United States Department of Commerce
Technology Administration
National Institute of Standards and Technology

NIST Technical Note 1500-4
Materials Reliability Series

Nondestructive Characterization of Reactor Pressure Vessel Steels: A Feasibility Study

Final Report
NRC Program RES-97-005

NIST Technical Note 1500-4
Materials Reliability Series

Nondestructive Characterization of Reactor Pressure Vessel Steels: A Feasibility Study

Submitted by
Harry I. McHenry, Program Manager
George A. Alers, Principal Investigator

Materials Reliability Division
Materials Science and Engineering Laboratory
National Institute of Standards and Technology
325 Broadway
Boulder, Colorado 80303-3328

Final Report, NRC Program RES-97-005
Control Number: B&R NO. 76015114010
Job Number: W 6738
Appropriation Symbol: 31x0200.760
BOC 253A

June 1998

U.S. DEPARTMENT OF COMMERCE, William M. Daley, Secretary
TECHNOLOGY ADMINISTRATION, Gary R. Bachula, Acting Under Secretary for Technology
NATIONAL INSTITUTE OF STANDARDS AND TECHNOLOGY, Raymond G. Kammer, Director

National Institute of Standards and Technology Technical Note
Natl. Inst. Stand. Technol., Tech. Note 1500-4, 104 pages (June 1998)
CODEN:NTNOEF

U.S. GOVERNMENT PRINTING OFFICE
WASHINGTON: 1998

For sale by the Superintendent of Documents, U.S. Government Printing Office, Washington, DC 20402-9325

CONTENTS

FOREWORD

The Materials Reliability Series of NIST Technical Notes are reports covering significant research accomplishments of the Materials Reliability Division. The Division develops measurement technologies that enable the producers and users of materials to improve the quality and reliability of their products. Measurement technologies are developed for process control to improve the quality and consistency of materials, for nondestructive evaluation to assure quality of finished materials and products, and for materials evaluation to assure reliable performance. Within these broad areas of measurement technology, the Division has focused its resources on three research themes:

- Intelligent Processing of Materials—To develop on-line sensors for measuring the materials' characteristics and/or processing conditions needed for real-time process control.

- Ultrasonic Characterization of Materials—To develop ultrasonic measurements for characterizing internal geometries of materials, such as defects, microstructures, and lattice distortions.

- Micrometer-Scale Measurements for Materials Evaluation—To develop measurement techniques for evaluating the mechanical, thermal, and magnetic behavior of thin films and coatings at the appropriate size scale.

This report is the fourth in the Materials Reliability Series. It covers research on nondestructive characterization of RPV steels, which is part of our research on ultrasonic characterization of materials. Previous reports in this series are:

Technical Note 1500-1	Tensile Testing of Thin Films: Techniques and Results, by D.T. Read, 1997
Technical Note 1500-2	Procedures for the Electron-Beam Moiré Technique, by E.R. Drexler, 1998
Technical Note 1500-3	High-Energy, Transmission X-ray Diffraction for Monitoring Turbine-Blade Solidification, by D.W. Fitting, W.P. Dubé, and T.A. Siewert, 1998

NONDESTRUCTIVE CHARACTERIZATION OF REACTOR PRESSURE VESSEL STEELS: A FEASIBILITY STUDY

Radiation damage to the walls of reactor pressure vessels (RPVs) causes the steel to become more brittle and less able to withstand the thermal stresses of start-up and shut-down procedures. Current methods of monitoring the degree of embrittlement are based on measurements of the ductile-to-brittle transition temperature (DBTT) of surveillance specimens subjected to severe radiation damage inside the reactor itself. In order to improve on this conservative approach and extend the useful life of vessels that have been in service for many years, NIST undertook a feasibility study to investigate nondestructive techniques for inferring the DBTT of the pressure vessel wall itself. The approach used was based on the hypothesis that the changes in microstructure that accompany embrittlement could be detected by accurate measurements of the physical properties of the steel in the pressure vessel wall. Nine magnetic and ultrasonic physical properties were measured on samples of RPV steel and on an A710 steel that could be heat treated to exhibit the same microstructural changes and embrittlement features as found in radiation damaged steel. The results showed that a nonlinear elastic coefficient, the magnetostriction constant and a dynamic magnetic permeability were strongly correlated with microscopic internal strains that appear to inhibit dislocation motion and cause embrittlement of the A710 steel. A study of techniques for making measurements of these three properties on a pressure vessel as well as for establishing their relationship to radiation embrittlement of A533B reactor steel is currently underway.

Key words: copper rich precipitates; elastic constants; internal friction; internal strain; magnetostriction; microstructure; nonlinear elasticity

1. INTRODUCTION

This program was undertaken in order to assess the feasibility of using physical property measurements to evaluate the embrittlement of reactor pressure vessel (RPV) steels. It is based on the premise that there are measurable physical properties that reflect the changes in microstructure that accompany radiation-induced embrittlement. If such properties can be found, then techniques and standards can be developed that will allow in-situ nondestructive testing of a pressure vessel to ensure its safe operation.

The approach proposed by NIST for the feasibility study was to accurately measure physical properties of unirradiated RPV steels as well as surrogate materials whose embrittlement mechanisms are similar to those thought to be responsibile for radiation induced embrittlement. The physical properties chosen were restricted to those that could be applied to the inner surface of a pressure vessel coated with a 7 mm thick stainless steel cladding. Thus, magnetic and ultrasonic methods that could penetrate the cladding were emphasized although x-ray diffraction studies were performed in order to establish the mechanisms behind the correlations observed between embrittlement parameters and physical-property measurements. Three sequential tasks were undertaken with the aim of producing recommendations for development of nondestructive testing procedures that could infer the ductile-to-brittle transition temperature of a pressure vessel embrittled by radiation damage. These tasks were as follows:

Task I. Procure samples of A533B RPV steels that have not been irradiated but which showed a spectrum of ductile-to-brittle transition temperatures (DBTTs) and perform a full set of ultrasonic and magnetic measurements on them as a function of temperature. The output of this task is intended to establish baseline values for the physical properties of RPV steels and to expose any relationships they might have with the DBTT.

Task II. Acurately measure ultrasonic and magnetic properties of a surrogate steel as it is embrittled by mechanisms similar to those expected to occur in irradiation embrittled pressure vessels. The output of this task is intended to establish those properties that are sensitive to embrittlement in radiation damaged RPV type steels and that can be measured nondestructively.

Task III. Investigate the possibilities for measuring the embrittlement related properties of the inner surface of a reactor pressure vessel that is clad with stainless steel.

Because this feasibility study demanded the performance of very accurate measurements by specialists in particular techniques, the body of the report has been organized by the physical property that was measured rather than by the tasks listed above. However, the Discussion Section presents the results as they apply to the tasks and the conclusions section presents the recommendations for the development of nondestructive testing methods and procedures. The table below lists the physical properties measured, the NIST staff member involved, and the rationalization for its relationship to mechanical strength parameters.

Table 1.1 Physical-mechanical properties measured in this study.

Property	Specialist	Information content
Elastic moduli	S. Kim	Direction dependence of the velocity of sound
Moduli and internal friction	H. Ledbetter	Dislocations and precipitation effects
X-ray diffraction	D. Balzar	Internal strain distributions on a submicron scale
Magnetic hysteresis	F. Fickett	Domain wall/imperfection interactions
Magnetostriction	B. Igarashi	Domain wall mobility and internal stresses
Incremental permeability	B. Igarashi	Dynamic magnetic response
Nonlinear ultrasonics	D. Hurley	Interatomic strain associated with precipitation
Stress induced damping	W. Johnson	Force required to move dislocations
Tensile properties	D. McColskey	Yield and ultimate strength. Elongation
Charpy energy	D. Vigliotti	DBTT and impact energy absorption
Hardness	P. Purtscher	Rockwell A hardness

2. MEASUREMENT RESULTS

2.1 MATERIALS — *P.T. Purtscher*

2.1.1 RPV Alloy A533B

Six samples of RPV steel were sent to NIST from ORNL. Four were cut from the SNUPPS vessel and two came from the Shoreham vessel. They were designated as shown in Table 2.1.1.

Figure 2.1.1 is a sketch that shows how the various test specimens were cut from the two largest segments of the SNUPPS material. Note that 20 Charpy specimens were cut from the weld and 20 more were cut from each of the four adjoining plates. These were designated W-1 (from the weld) and 1-1 from Segment 1, Plate 1; 1-2 from Segment 1, Plate 2: etc.

Half of the cladding from the 157 × 66 mm face of SNUPPS Seg. #4 was cut away from the base metal by EDM techniques to produce a 76 × 57 mm plate sample of the stainless steel approximately 3 mm thick so that its acoustic and electrical properties could be measured independently of the A533B substrate.

The two full thickness samples cut from the Shoreham RPV were delivered to NIST in order to provide examples of material coated with the stainless steel cladding and having the geometry that will be faced in the ultimate application of any nondestructive test. They each weigh approximately 1000 kg (2200 lb) and have been mounted on special heavy duty carts in order to facilitate their being moved to different laboratories within the NIST facilities.

Table 2.1.1 Designations assigned to the RPV materials provided to NIST by ORNL.

Designation	Dimensions (mm)	Description
SNUPPS Seg. #1	775 × 264 × 95	Girth weld and rolling dir. parrallel to 264 dim.
SNUPPS Seg. #2	914 × 240 × 50-90	Axial weld parrallel to 240, rolling dir. along 914 dim.
SNUPPS Seg. #3	226 × 157 × 66	Cladding over the 157 × 66 mm face
SNUPPS Seg. #4	226 × 175 × 66	Cladding over the 175 × 66 mm face
Shoreham I	953 × 914 × 159	6 mm thick cladding over 940 × 914 face
Shoreham II	921 × 890 × 159	6 mm thick cladding over 914 × 890 face

2.1.2 Dilute Copper in Iron Alloys

A recent review article [2.1.1] and several previous publications [2.1.2 – 2.1.4] ascribe the decrease in ductility and embrittlement of the pressure vessel to the formation of copper-rich precipitates (CRPs) which are known to increase the flow stress and hardness. The CRPs are typically 1 to 2 nm in diameter and are a precursor to the formation of the equilibrium ϵ phase shown in the iron-copper phase diagram. The Cu content of pressure vessel steels is normally never over 0.45 mass percent, but given the typical neutron fluence of 1 to 3 × 10^{19} cm^2 (for neutrons with energies over 1 MeV) and a typical Ni content of 1.4 mass percent, the shift in the DBTT compared to the pre-irradiated properties can be as large as 230 °C [2.1.5]. Due to the small size of the CRPs, the monitoring of their formation is difficult but is very important to the safety of the RPV.

2.1.3 Preparation of Materials and Test Specimens

In order to find those physical properties that can sense the formation of CRPs and hence be candidates for a nondestructive predictor of embrittlement, two steels containing 0.35 (SAE 1508) and 1.13 mass percent copper (ASTM A710) from earlier NIST programs were evaluated for their suitability as surrogate materials. The compositions are included in Table 2.1.2. The effects of direct quenching from hot rolling and subsequent tempering on these two steels was published by Manganello and Wilson [2.1.6]. Figure 2.1.2 shows the effect of tempering temperature on the yield strength (YS) for 19 mm thick plates from the two steels after direct quenching. Steel A (1508) demonstrated a definite peak in the YS after tempering at temperatures above 500 °C; steel C (A710) demonstrated a peak in the YS at 510 °C. The peak in YS is considered to be due to CRPs. The 19 mm thick plates that were available at NIST were in the peak-aged condition for each composition and hence include the CRPs in the microstructure.

Our initial experiments with the two potential surrogate steels were to determine whether the strengthening due to CRPs could be observed in heat treated conditions as well as in the direct quench and tempered condition. For this purpose, small samples (10 mm × 10 mm × 55 mm) were heat treated to various conditions. The standard solution treatment involved heating the samples to 900 °C and holding for 1 hour. This solution treatment will dissolve all of the Cu in austenite while retaining a 10 μm austenite grain size. After solution treatment, the samples were then cooled in vermiculite to room temperature and aged at temperatures between 450 and 700 °C for 1 hour. Hardness was used for the evaluation in this initial experiment. The hardness of steel A was R_A 50 and did not increase with subsequent aging treatments. For steel C, a definite peak in hardness was observed at about 525 °C and the minimum hardness was found at 700 °C. (See Fig. 2.1.3.) Thus, we concluded that steel C could be heat treated to produce precipitation strengthening from the CRPs, whereas steel A could not.

For the nondestructive characterization of microstructure, larger samples (19 × 25 × 300 mm long) were prepared so that multiple samples could be machined from each bar. The goal

Table 2.1.2 Nominal composition (in mass percent) of the steels investigated in this study.

Designation	Cu	Ni	C	Mn	Si	Cr	Mo	Nb	Al
A(1508)	-0.35	0.35	0.08	1.35	0.25	0.03	0.06	0.02	0.022
C(A710)	1.13	0.87	0.05	0.53	0.30	0.75	0.21	0.32	0.023
A533B	0.11	0.8	0.19	1.29	0.2	0.12	0.53		0.015

was to produce underaged, peak-aged, and overaged samples with respect to the precipitation strengthening due to CRPs for each steel. In steel A, precipitation strengthening could be achieved only with the as-received, directly quenched and tempered plates. Therefore, the as-received plate, designated A5, would be the peak aged condition and aging of the as-received plate at 675 °C would represent the overaged condition, designated A6. Underaged, directly quenched samples were not available so samples quenched in water, designated AA, and air cooled, designated AA-2, from the 900 °C solution heat treatment temperature were produced. Both AA samples were underaged with respect to CRP strengthening, but with different microstructures. For steel C, the large bars were air cooled to room temperature, designated CA (underaged), and then some bars were aged at 525 °C, designated C5 (peak aged), and others were aged at 700 °C, designated C7 (overaged). A summary of the microstructures evaluated by the nondestructive characterization methods is shown in Table 2.1.3.

Table 2.1.3 Microstructures observed in the copper alloys that were investigated following various heat treatments.

Desig-nation	Heat treatment	Matrix metallography	State of copper	Hardness Rockwell A
AA	As quenched	Acicular α + Bainite	Underaged	59.0
AA-2	Air cooled	Polygonal α + Bainite	Underaged	50.0 ± 0.5
A5	As received	Tempered α + 2nd phase	Peak aged	54.3 ± 0.5
A6	Rec'd + 675 °C*	Tempered α + 2nd phase	Overaged	53.1 ± 0.5
CA	Air cool	Polygonal α + 2nd phase	Underaged	55.6 ± 0.5
C5	Air Cool + 525 °C*	Polygonal α + 2nd phase	Peak aged	58.5 ± 0.5
C7	Air Cool + 700 °C*	Polygonal α + 2nd phase	Overaged	53.2 ± 0.5

*for 1 hour

For steel A (1508), the microstructures are represented by the following micrographs. Figure 2.1.4 shows the acicular α and bainitic microstructure of sample AA. The water quenching was not fast enough to produce a martensitic matrix. Figure 2.1.5 shows the polygonal α plus bainite structure found in the air cooled AA-2 sample. These two represent the conditions with the least precipitation strengthening (underaged with 0.35% Cu); AA has the highest hardness because water quenching did produce transformation strengthening. Figure 2.1.6 is representative of both A5 and A6, which had very similar microstructures when observed in the light microscope. This microstructure is mainly tempered α with some second phase scattered throughout, indicative of the low C content.

For steel C (A710), the microstructures observed in the light microscope for all three samples are very similar. Figure 2.1.7 shows the air-cooled CA sample, which was not aged (underaged with 1.13% Cu). The microstructure is mainly polygonal α but with a dispersed second phase that is probably a granular bainite, described in detail by Thompson and Krauss [2.1.3]. Figure 2.1.8 shows the microstructure found in C5 (peak aged), which is similar to that shown in Figure 2.1.7. The formation of CRPs is not visible at this magnification. The presence of CRPs is inferred from the hardness change that occurs during aging. The fact that the hardnesses of CA, C5, and C7 do not correspond exactly with those in Figure 2.2.2 reflects the influence of specimen size (cooling rate) on the matrix strength due to differences in transformation strengthening.

The microstructure of the A533B is quite different from that observed in both steels A and C. Figure 2.1.9 shows a low magnification view from a representative area in SNUPPS Seg. #1 (plate 1-1). There is some chemical segregation that produces light and dark etching contrast with a spacing of about 100 μm. At a higher magnification, the etching contrast is due to the amount of second phase, light contrast being less second phase, Fig. 2.1.10, and the dark contrast due to more second phase, Fig. 2.1.11. In either case, the microstructure of the A533B is finer than that of the surrogate samples and has a higher volume fraction of second phase due to the higher C content.

After heat treatment of large samples of steels A and C individual test specimens for each physical property were machined from the blocks. The specimen size for each test is summarized in Table 2.1.4.

2.1.4 References

2.1.1 Odette, G.R.; G.E. Lucas, An integrated appoach to evaluating the fracture of irradiated irradiated nuclear reactor pressure vessels. Nondestructive Eval., 15(3/4):137; 1996.

Table 2.1.4 Specimen dimensions used for the physical properties measured in this study.

Physical property	Shape	Specimen dimensions (in mm)
1. Magnetic - Hc and Ms	Cylinder	2 (dia) × 20 long & 3 (dia) x 30 long
2. Magnetostriction coef.	Block	9 × 20 × 125
3. Transverse incremental permeability	Block	9 × 20 × 125
4. C_{ij} and Q^{-1} and density	Block	10 × 11 × 12
5. Young's Modulus and Q	Sq. Bars	4 × 4 × 19, 25 and 50 long
6. Shear and longitudinal wave velocity	Block	25 × 50 × 19
7. Acoustic nonlinearity parameter, β	Block	25 × 50 × 19
8. Dislocation breakaway stress	Cylinder	20 (dia) × 160 long
9. Tensile strength	Cylinder	12 (dia) × 75 long

2.1.2 Lahiri, S.K.; Chandra, D.; Schwartz, L.H.; Fine, M.E., Modulus and Mossbauer Studies of Precipitation in Fe-1.67 At. pct. Cu, Trans. Metall Soc. AIME, 245:1865, Sept. 1969.

2.1.3 Thompson, S.W.; Krauss, G., Copper Precipitation During Continuous Cooling and Isothermal Aging of A710-Type Steels, Metall. Mater. Trans. A, 27A:1573, June 1996.

2.1.4 Aroztegui, J.J.; Urcola, J.J.; Fuentes, M.; The Influence of Copper Precipitation and Plastic Deformation Hardening on the Impact Transition Temperature of Rolled Structural Steels, Metall. Trans. A, 20A:1657, Sept. 1989.

2.1.5 United States Nuclear Regulatory Commission, Regulatory Guide 1.99: Radiation Embrittlement of Reactor Vessel Materials, U.S. Government Printing Office, Washington, D.C. 1988.

2.1.6 Manganello, S.J.; Wilson, A.D., Direct Quenching and Its Effects on High-Strength Armor Plate, in Low-Carbon Steels for the 90's, R. Asfahani and G. Tither, eds. TMS, Warrendale, PA, p. 235, (1993).

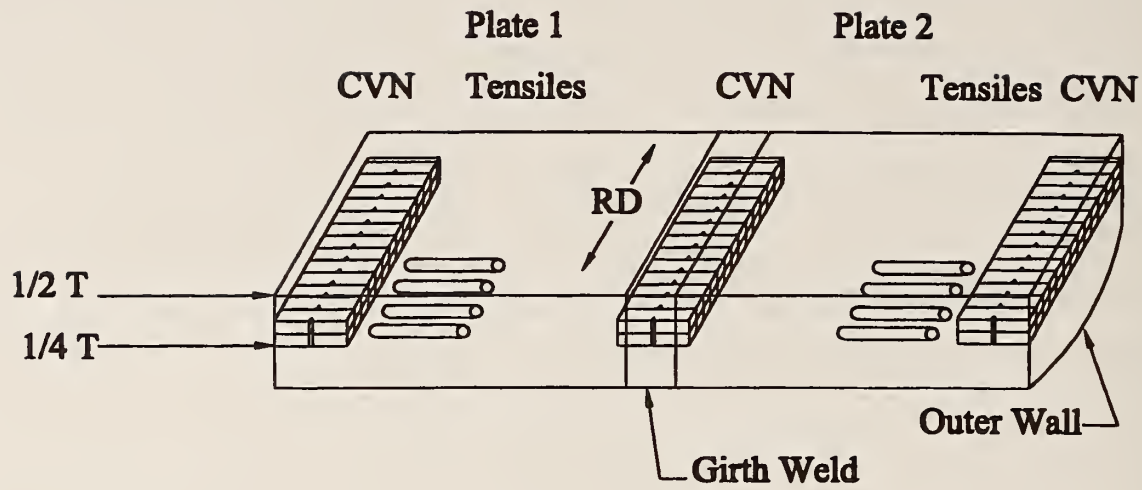

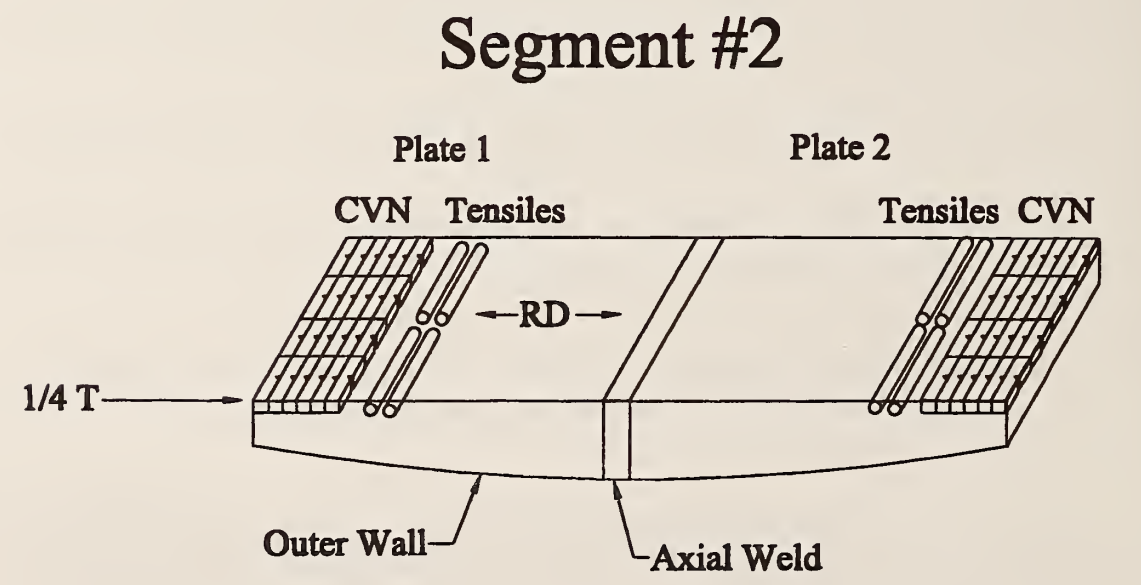

Fig. 2.1.1 Sketch of the SNUPPS Segments #1 and #2 showing the location of pieces used for various measurement specimens. T = thickness, CVN = Charpy V Notch.

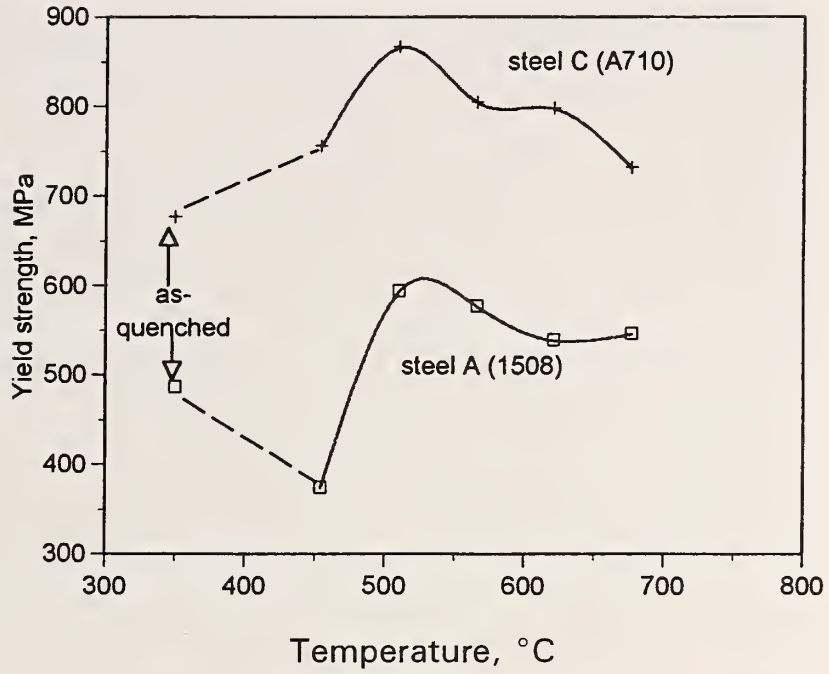

Fig. 2.1.2 Yield strength versus tempering temperature for 19-mm-thick plates of Cu-containing steels produced by the direct-quench process [2.1.6].

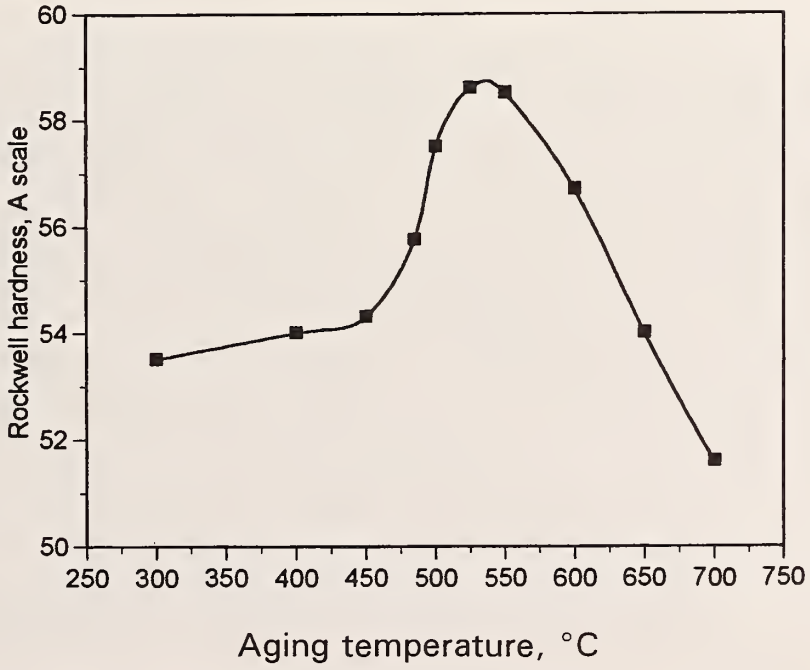

Fig. 2.1.3 Hardness versus aging temperature for steel C (A710) after solution heat treatment at 900 °C for 1 h and cooling in vermiculite.

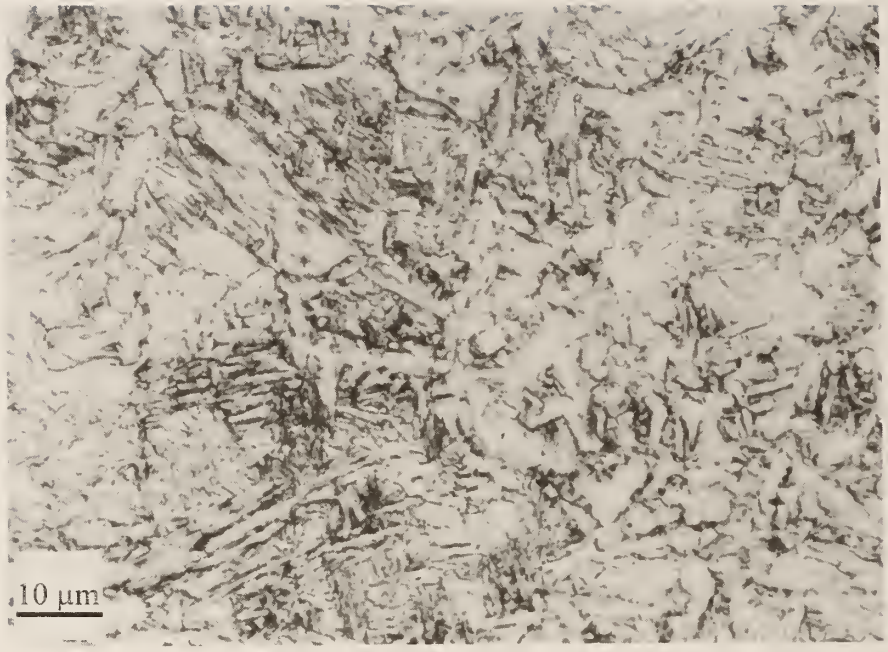

Fig. 2.1.4 Light micrograph of the water-quenched steel A sample AA. Bar = 10 μm.

Fig. 2.1.5 Light micrograph of the air-cooled steel A sample AA. Bar = 20 μm.

Fig. 2.1.6 Light micrograph of the direct-quenched and tempered steel A sample A5. This microstructure is also representative of sample A6. Bar = 20 μm.

(a)

(b)

Fig. 2.1.7 Light micrographs of the air-cooled steel C sample CA. Bar = 20 μm in (a) and 7 μm in (b).

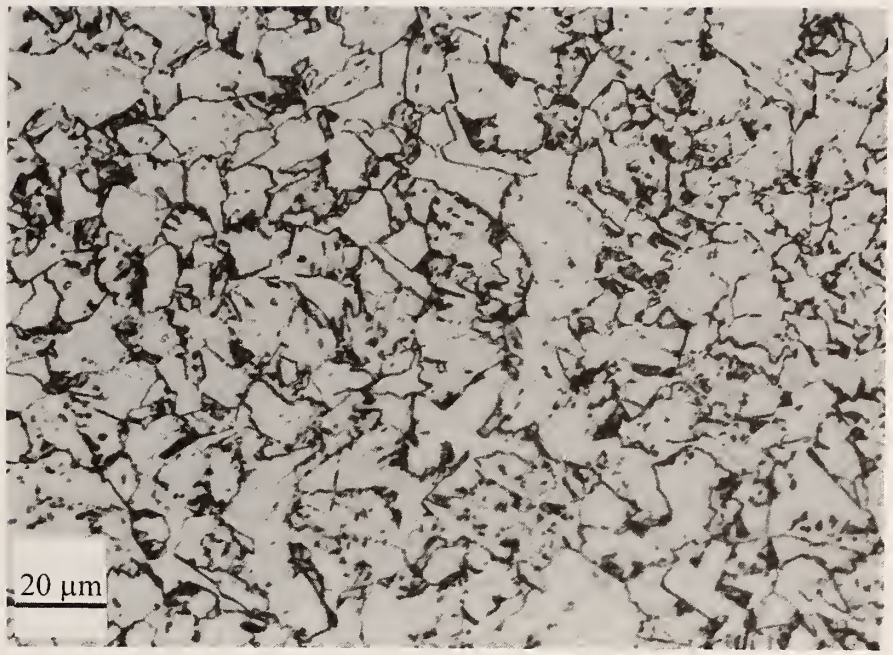

(a)

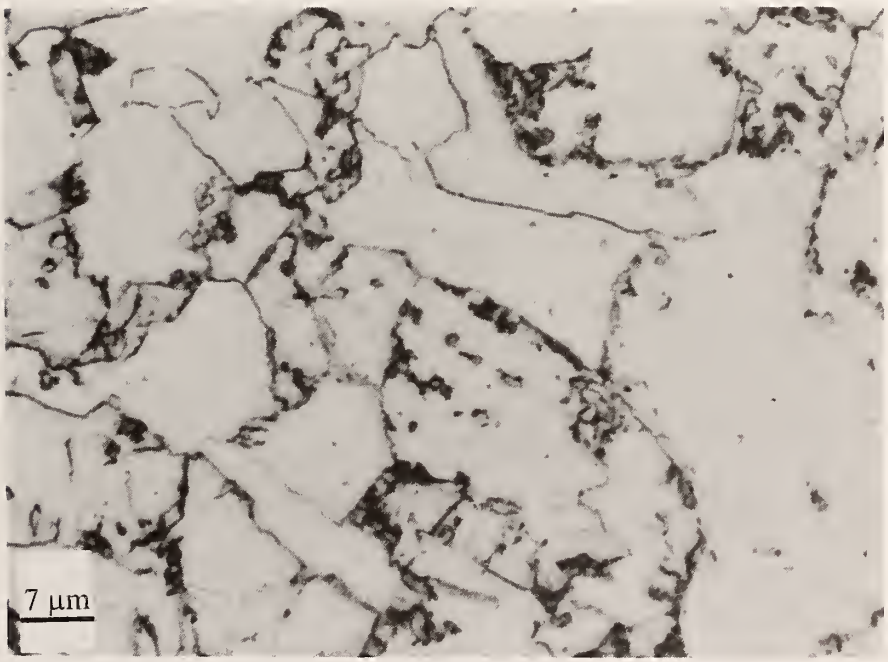

(b)

Fig. 2.1.8 Light micrographs of the air-cooled and aged steel C sample C5. This microstructure is also representative of sample C7. Bar = 20 µm in (a) and 7 µm in (b).

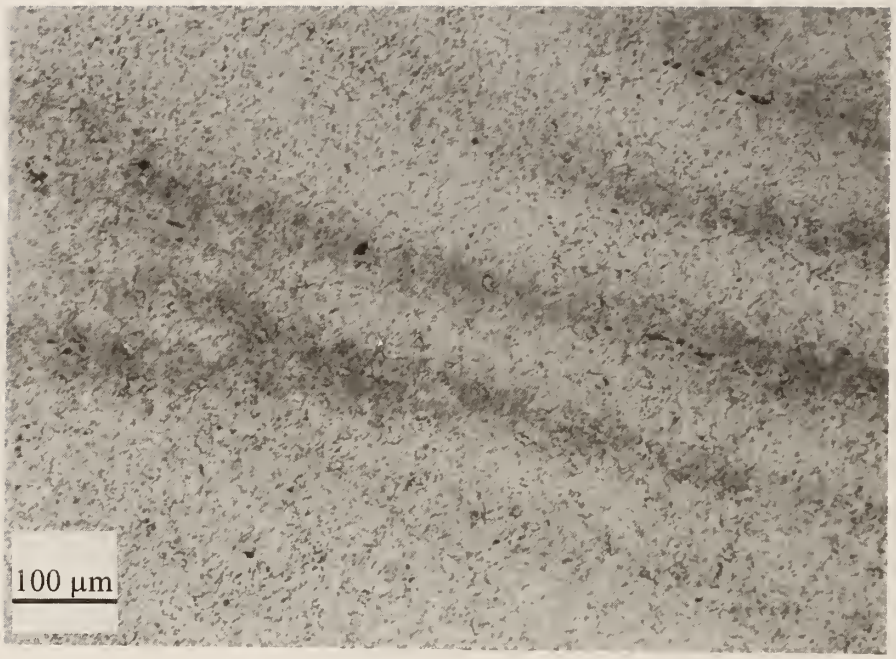

Fig. 2.1.9 Light micrograph at low magnification of the quenched and tempered A533B base metal sample 1-1. Bar = 100 μm.

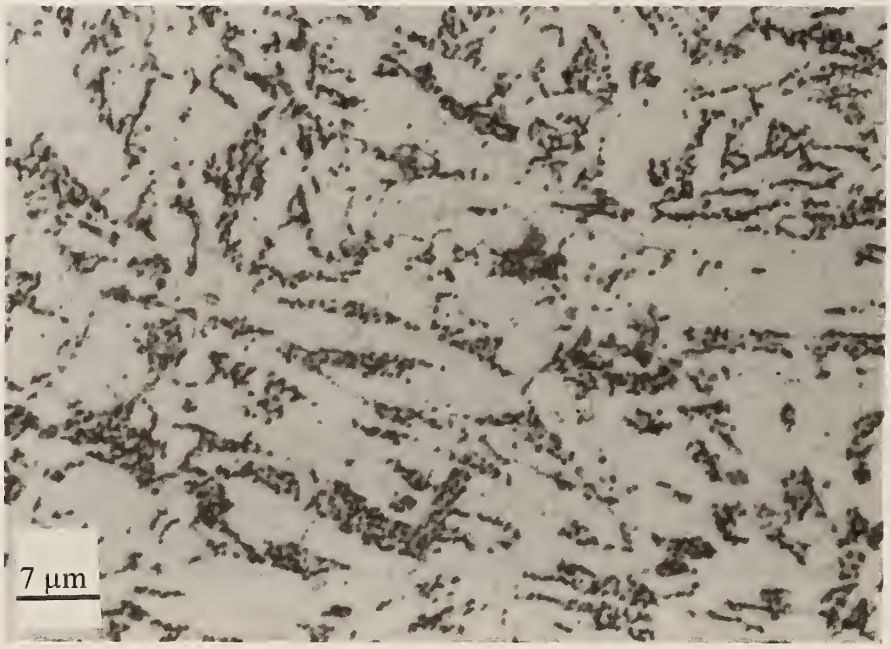

Fig. 2.1.10 Light micrograph at high magnification of the quenched and tempered A533B base metal sample 1-1, lighter etching area. Bar = 7 μm.

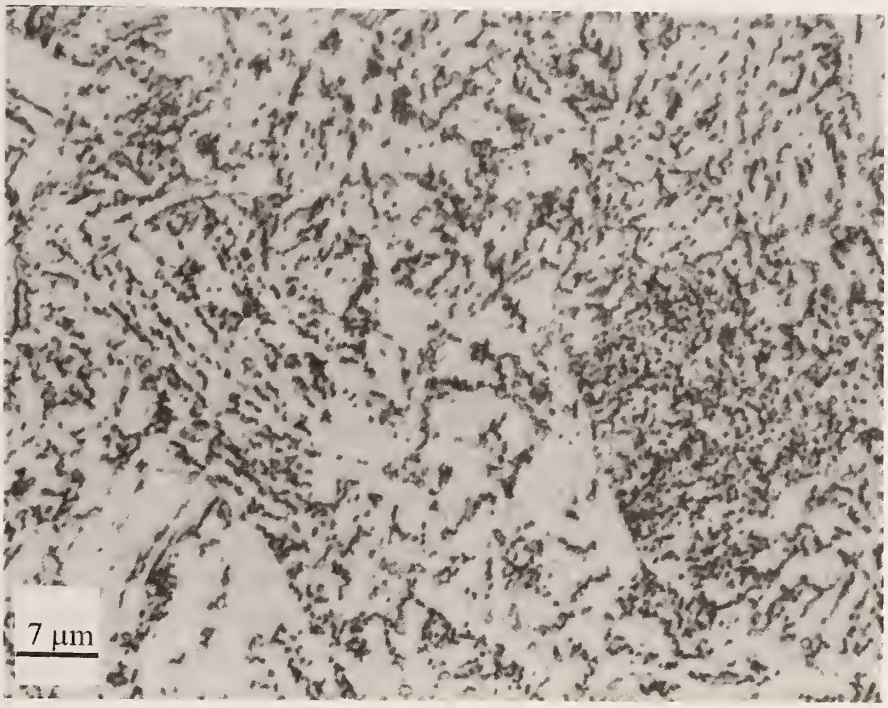

Fig. 2.1.11 Light micrograph at high magnification of the quenched and tempered A533B base metal sample 1-1, darker etching area. Bar = 7 μm.

2.2 MECHANICAL PROPERTIES — *D. McColskey and D. Vigliotti*

Standard tensile test specimens were machined and tested according to ASTM recommended procedure E-8. The A-533B tensile specimens were machined with a test section diameter of 12.7 mm (0.5 in) and, because of material thickness limitations, the CA, C5, C7, AA, A5 and A7 materials were machined with a 6.37 mm (0.25 in) test section diameter. The weld section of the A533B material was also tested in the smaller diameter because of limited material availability. In all cases, the test section gage length was four times the specimen diameter.

Tensile tests were conducted in a screw-driven tensile testing machine at an initial strain rate, in the elastic region of the test, of 0.02 per minute. An extensometer monitored the specimen test section elongation during the test. The strain sensitivity during the yielding process allowed the detection of a 0.01% deviation from linearity to be detected. Thus, the proportional limit could be measured even in cases where a discontinuous yield drop was observed. Table 2.2.1 lists the tensile properties deduced from load-elongation curves for all the materials studied in this program. Many of the materials showed discontinuous yielding behavior so the upper yield and the 0.2% offset yield strengths are listed in the table. Yield strength was determined using the 0.2% offset method. Yield point, for materials that exhibited discontinuous yielding, was determined using the autographic diagram method. Those materials that showed no load drop but continuously work hardened at stresses above the proportional limit have been listed in the table as having no upper yield point.

Also included in Table 2.2.1 are values for the Rockwell A hardness and the 41 J (30 ft · lbf) ductile-to-brittle transition temperature (DBTT). The latter was deduced from measurements on 15 standard notched Charpy bars (from each material) machined and tested according to ASTM recommended procedure E-23. Test temperatures for the Charpy specimens were selected to establish a full transition temperature curve and ranged between +100 and −100 °C.

The A series alloys did not show significant changes in hardness in response to the heat treatments intended to form CRPs so a complete set of physical property and mechanical strength values was not developed for the A alloy series. However, the C alloy series showed clear evidence for the strengthening effect of the CRPs. Therefore, a very complete set of data that included the DBTT was generated for this alloy and they are presented in Table 2.2.1. Figure 2.2.1 shows the low strain portions of the stress-strain curves obtained on the C series alloy (A710 steel) in the solution treated, peak aged, and overaged conditions. These curves show the large increase in flow stress as the solution treated or as-cooled alloy was tempered to the peak-aged or peak hardness condition produced by the formation of the CRPs. Upon overaging, copper precipitates form and a discontinuous yielding response develops at a stress level higher than the proportional limit of the peak aged condition. Since the hardness is often used as a measure of strength and is correlated with various nondestructively measured physical properties, it is instructive to plot hardness against the other mechanical properties that can be deduced from a tensile test. Figure 2.2.2 shows such a graph relating the proportional limit, the 0.2% offset yield strength and the ultimate tensile strength to the hardness. It is clear that there is a good,

Table 2.2.1 Tensile properties of the materials used in this study as deduced from constant strain rate tensile tests on cylindrical samples

Material	Prop. limit MPa	Upper yield point MPa	0.2% offset yield strength MPa	Ultimate tensile str. MPa	Elongation %	Hardness Rockwell A	41 J DBTT °C
CA	173	—	415	650	27.8	55.6	-33
C5	391	—	551	718	25.1	58.5	-10
C7	446	471	471	558	29.2	53.2	-60
AA	287	—	575	821	6.6	59	—
A5	576	576	560	610	24.8	54	—
A6	524	524	514	594	25.3	53	—
A533 1-1	479	491	465	610	38	55.3	-20
A533 1-2	461	468	452	574	43	53.3	-60
A533 2-1	476	482	475	600	40	55.1	-25
A533 2-2	513	525	507	640	35	56.0	-20
A533 W-1	568	589	578	672	24	57.0	-30

linear correlation between the hardness and the ultimate tensile strength but no linear correlation between hardness and the proportional limit (when irreversible plastic flow is initiated) or the 0.2% offset yield strength.

An even more striking display of the effect of heat treatment and the formation of CRPs in the A 710 steel alloy is shown in Fig. 2.2.3 where the absorbed energy from the Charpy impact test is plotted against temperature for the three heat treatment conditions. This graph shows that both the transition temperature and the upper shelf energy are changed by the aging process and that overaging makes the transition from ductile to brittle very sharp. For comparison purposes, the results of Charpy impact tests on the unirradiated A533B material are also plotted in Fig. 2.2.3. For the RPV material, the transition is gradual, at a higher temperature and exhibits a low upper shelf energy compared to that of the 1.13% Cu alloy. With increasing radiation damage, A533B shows an even lower upper shelf energy and a less pronounced transition between ductile and brittle behavior.

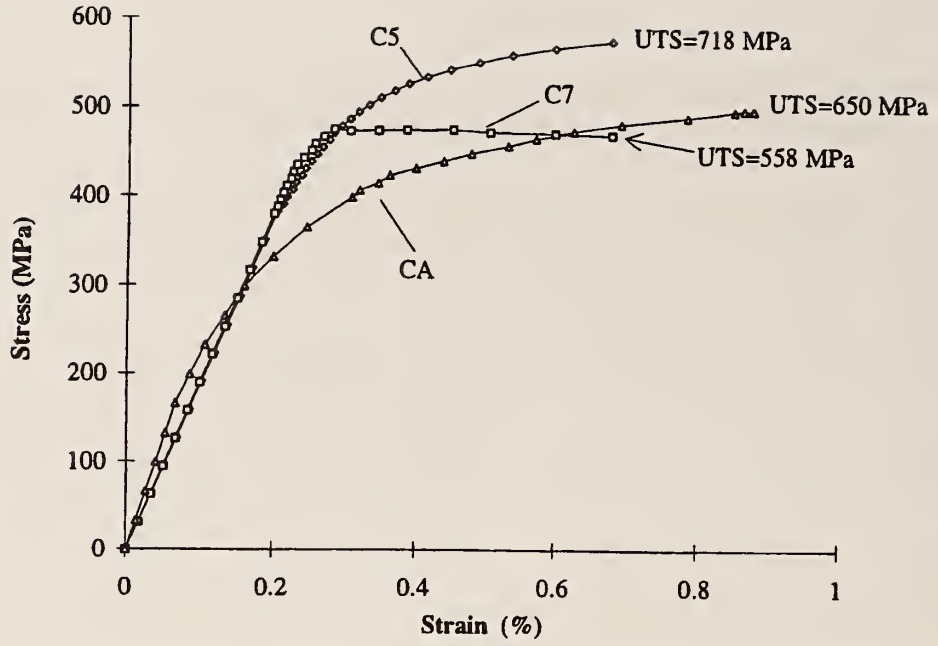

Fig. 2.2.1 Low strain portion of the stress strain curves for the Fe-1.13% Cu alloy in the three heat treatment conditions.

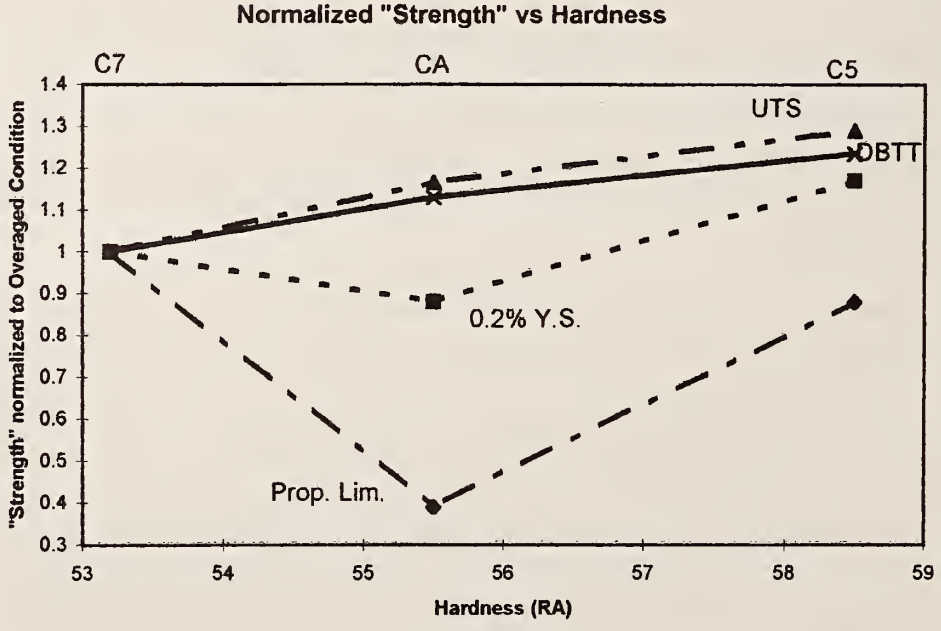

Fig. 2.2.2 Graphical representation of Table 2.2.1 showing the relationship between the hardness and four strength measures: the proportional limit, the 0.2% yield strength, the ductile-to-brittle transition temperature and the ultimate tensile strength for the Fe-1.13% Cu in the overaged condition (C7), the solution treated condition (CA) and the peak-aged condition (C5).

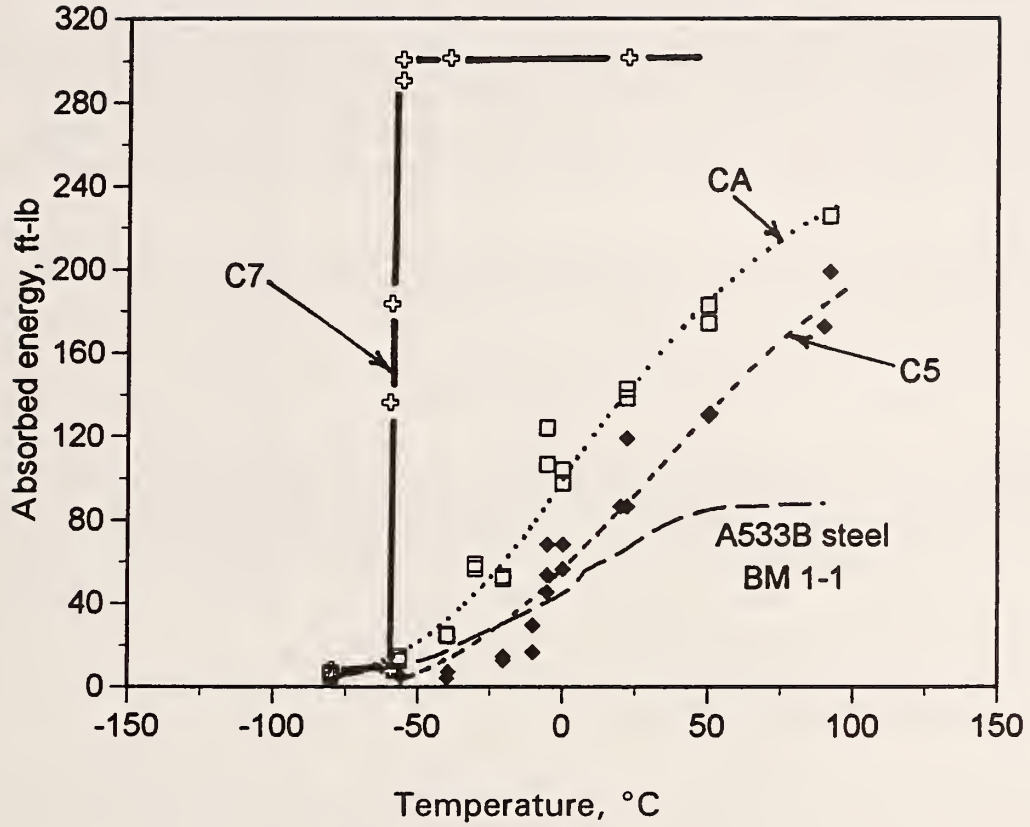

Fig. 2.2.3 Charpy energy versus temperature for the Fe-1.13% Cu alloy in the three heat treatment conditions: CA - solution treated, C5 - peak aged, C7 - overaged. Also shown for reference are measurements on A533B steel.

2.3 ELASTIC PROPERTIES — *Sudook Kim*

2.3.1 Introduction

We report measurements of elastic-stiffness coefficients and their associated imaginary parts, the internal frictions, for three body centered cubic (b.c.c.) steels, one in three heat treatment conditions. We used four dynamic measurement methods and varied the strain magnitude, the frequency, and the temperature. Our measurements also produced values for the mass density.

The elastic-stiffness coefficient, a fourth-order tensor $\tilde{C}_{ijkl}$, contains two parts, real and imaginary:

$$\tilde{C}_{ijkl} = \tilde{C}_{ij} = C_{ij} (1 + i\, Q_{ij}^{-1}) . \qquad (1)$$

The four-index to two-index transformation represents the usual Voigt contraction method. The internal-friction term Q_{ij}^{-1} is small: less than 10^{-2} and sometimes much smaller, say 10^{-5}. Both properties, C_{ij} and Q_{ij}^{-1}, correlate strongly with other physical-mechanical properties. C_{ij} relates strongly to lattice-vibrational properties such as specific heat; thus it is relatively structure insensitive. However, Q_{ij}^{-1} is strongly structure sensitive and is used widely to study material defects such as dislocations, grain boundaries, vacancies, and so on.

2.3.2 Details of Measurement Methods

The five cases we considered (CA, C5, C7, 1-2, W1) are described elsewhere in this report in terms of chemical composition, heat treatment, hardness, plastic-deformation behavior, and so on.

There are numerous methods for measuring the C_{ij}. The most common—slope of quasistatic stress-strain curve—is also the least accurate, and yields little reliable Q_{ij}^{-1} information. Therefore, we used four dynamic methods:

TP, forced-vibration torsional pendulum (near 1 Hz);
MOR, Marx-oscillator resonance (50 to200 kHz);
ARS, acoustic-resonance spectroscopy (50 kHz to 5 MHz);
PES, pulse-echo superposition (5 to 10 MHz).

We made most measurements by the third method. For these materials, the ARS method gives 0.05% uncertainty in C_{ij} and 10% uncertainty in Q_{ij}^{-1}.

2.3.3 Results and Discussion

We made all measurements at ambient temperatures, except for E versus T and Q^{-1} versus T for the CA steel measured between 295 and 200 K. For each of the five steels, we constructed tables of 48 measured physical-property values, thus 240 values altogether. For all cases, we obtained by analysis some additional physical-property values: the monocrystal elastic-stiffness coefficients C^{o}_{ij}. Tables 2.3.1 through 2.3.3 and Figures 2.3.1 through 14 show most of our main results.

Compared with typical commercial b.c.c. steels, the elastic-shear stiffnesses show low to moderate anisotropy with values ranging from 1.000 (isotropic) to 1.085, about 6% of the maximum-possible anisotropy. (See Table 2.3.3.) With aging, the anisotropy decreased slightly in the C series steels. Both W1 and 1-2 steels show nearly isotropic elastic stiffnesses. Presumably, most of the anisotropy arises from texture (nonrandom crystallite orientations).

Anisotropy of the shear-mode internal friction Q^{-1}_{G} varied from 1.14 to 2.74, a surprisingly narrow range given the possibilities arising from changes in microstructure. During thermal treatment, the C series steels showed decreasing Q^{-1} anisotropy, probably reflecting dislocation rearrangement.

For all five steels, all the usual quasiisotropic elastic stiffnesses B, E, G, C_L, lie within a band 2% below the values of pure Fe. Thus, to use these stiffnesses as a quality parameter requires a measurement sensitivity of better than 0.1%, which we have in both the ARS and MOR measurement methods.

As a function of aging treatment, the C series steels show a tight monotonic increase in the C_{ij}, increasing about 1% from the underaged to overaged conditions. (See Figs. 2.3.1 and 2.) The internal friction provides even larger promise for hardness correlations. For the C series steels, where hardness increases about 3 digits on the Rockwell-A scale upon going from underaged to peak aged, Q^{-1}_{G} decreases from about 13 to 8 and Q^{-1}_{B} from 21 to 4. Presumably, the decrease results from precipitation of small coherent Cu-rich particles, which pin dislocations, which we assume make the largest contribution to Q^{-1}. (See Figs. 2.3.3 through 2.3.5.) We measured both the strain and frequency dependences of Q^{-1}, both useful probes of the lattice defects. Both results present surprises. (See Figs. 2.3.6 through 2.3.9.) The Q^{-1} strain-dependence curve rises rapidly and reaches a saturation value. Figure 2.3.7 gives a possible explanation. The Q^{-1} frequency dependence shows a negative slope (Fig. 2.3.8). At frequencies below ω_o, the Koehler-Granato-Lücke [2.3.1] model predicts a positive slope. This opens the possibility of magnetic contributions to Q^{-1}. However, magnetomechanical hysteresis shows no frequency dependence. Microeddy currents show Q^{-1} proportional to frequency f. Macroeddy currents show the same proportionality at low f and a $f^{-1/2}$ dependence at high f. Thus, we fail to understand the negative slope dQ^{-1}/df.

Using MOR equipment at 150 kHz, we measured the Young modulus E and the associated internal friction Q^{-1} between 295 and 200 K, for the CA steel. (See Fig. 2.3.10.) During cooling, the Young modulus showed a smooth monotonic increase with a slope higher than for pure iron. We expect this from alloying effects and the fact that the Fe-Cu steel has lower elastic stiffness than iron. The E-T curve showed no detectable irregularities upon cooling through the ductile-brittle transition. The Q^{-1} versus T curve showed a surprising result: a relatively sharp peak near 265 K, significantly below the ductile-brittle onset. (See Fig. 2.3.11.) If further measurements on other steels confirm this peak, then we speculate that it arises from dislocations. One proposed explanation of the ductile-brittle transition is that the a/2<111> screw dislocations become immobilized by defects such as interstitials, substitutionals, precipitates.

By collaborating with a non-NIST research group [2.3.2], we used a forced-vibration torsional pendulum to measure Q^{-1} at frequencies from 0.001 to 10 Hz (4 decades) for CA, C5, C7 steels. (See Fig. 2.3.12.) Absolute Q^{-1} values agreed well with ours measured at kHz to MHz frequencies, and the results show the above-described V-shape behavior: CA>C7>C5. However, the spectrum failed to show an expected peak near 0.1 Hz. After annealing the C5 specimen at 525 °C for 5 minutes, we found a strong internal-friction peak near 0.1 Hz. Thus, if, after thermal treatment, these alloys sit at ambient temperature for a long time, then microstructural changes eliminate the near −0.1 Hz peak in the mechanical-spectroscopy spectrum. This peak arises from carbon-lattice interactions. But it could prove useful in studying copper-atom distribution because the Cu-C interaction must differ from the Fe-C interaction.

We considered correlations with mechanical hardness. The C series steels stiffen elastically with increasing hardness, but soften beyond the optimum-aging treatment. In the C-steel case, in going from hardness 56 to hardness 58, the shear modulus increases about 0.4%, almost 10 times our measurement uncertainty of 0.05%. Thus, we can correlate elastic stiffness and hardness, which relates in turn to yield strength, and to the ductile-brittle-transition temperature. See Figs. 2.3.13 and 14.

Finally, we considered texture, which can alter drastically the elastic-coefficient values. We assumed orthotropic macroscopic symmetry: x^1 = rolling direction, x^2 = transverse direction, x^3 = plate-normal direction. From the measured C_{ij}, we calculated the orientation-distribution coefficients W_{ijk}. We used these to prepare (110), (111), (200) pole figures for the CA, C5, C7 steels. (See Fig. 2.3.1.5.) As expected, the CA and C5 pole figures showed identical pole distributions. The C7 pole figure differed slightly, suggesting the beginning of recrystallization, which would alter both the macroscopic elastic stiffnesses C_{ij} and their associated internal frictions Q_{ij}^{-1}. All the pole figures show a hint of the usual b.c.c. rolling texture: (100) planes perpendicular to x^3.

2.3.4 Conclusions

From these measurements on elastic stiffnesses C_{ij} and internal frictions Q_{ij}^{-1}, we draw the following conclusions:

1. With thermal-treatment-induced microstructural changes, the C_{ij} change is small, (about one-half percent) but large compared to our measurement uncertainties.

2. Q_{ij}^{-1} shows a much larger change. For example, some of the Q_{ij}^{-1} are about 40% lower for the C5 steel than the CA steel.

3. Although the relationship is not monotonic, both C_{ij} and Q_{ij}^{-1} change with hardness, as expected from the presumed microstructural changes.

2.3.5 Recommendations

Based on the present results, we advocate the following further studies:

1. Assuming that Cu atom distribution affects ductile-to-brittle behavior, study a series of Fe-Cu binary alloys free from complications of other alloying elements.

2. Further studies on internal friction, including especially the effects of temperature, strain, and frequency.

3. Consider magnetic-field effects on reducing total internal friction.

4. Perform additional low-frequency torsional-pendulum measurements because this method appears to provide the most-accurate internal-friction values.

5. Explore the possibility of getting useful information from the Snoek peak. Carbon atoms provide a potent anisotropic strain field, which should change when other impurity atoms such as copper occupy the lattice.

6. Conduct basic studies on the substitutional-interstitial internal-friction problem (mainly Snoek peak). This would require a series of Fe-Cu-C alloys.

2.3.6 References

2.3.1 Lucke, K.; Granato, A.; Application of Dislocation Theory to Internal Friction Phenomena at High Frequencies, J. Appl. Phys. 27:789; 1956.

2.3.2 Commercial instrument made available by Professor Wuttig of The University of Maryland.

Table 2.3.1 Elastic coefficients and internal frictions of C steels.

		CA (underaged)	C5 (optimum-aged)	C7 (overaged)	Iron
ρ (g/cm^3)	=	7.8414	7.8558	7.8534	7.872
C_{11} (GPa)	=	272.96±0.46	273.44±0.57	275.38±0.72	276.85
C_{22} (GPa)	=	275.37±0.30	275.75±0.39	276.16±0.44	
C_{33} (GPa)	=	272.13±0.73	273.48±0.90	273.26±0.98	
C_{12} (GPa)	=	105.77±0.36	105.44±0.44	106.52±0.81	111.97
C_{13} (GPa)	=	111.47±0.64	111.90±0.78	112.06±0.82	
C_{23} (GPa)	=	107.93±0.60	108.03±0.75	108.89±0.51	
C_{44} (GPa)	=	78.725±0.000	78.944±0.000	79.804 ±0.008	82.44
C_{55} (GPa)	=	82.371±0.008	82.684±0.008	82.975 ±0.008	
C_{66} (GPa)	=	77.571±0.023	77.955±0.023	78.414 ±0.024	
S_{11} (TPa^{-1})	=	4.739	4.727	4.695	4.709
S_{22} (TPa^{-1})	=	4.632	4.617	4.628	
S_{33} (TPa^{-1})	=	4.791	4.767	4.776	
S_{12} (TPa^{-1})	=	−1.255	−1.242	−1.248	−1.356
S_{13} (TPa^{-1})	=	−1.444	−1.444	−1.428	
S_{23} (TPa^{-1})	=	−1.323	−1.316	−1.332	
S_{44} (TPa^{-1})	=	12.70	12.67	12.53	12.13
S_{55} (TPa^{-1})	=	12.14	12.09	12.05	
S_{66} (TPa^{-1})	=	12.89	12.83	12.75	
B (GPa)	=	163.42	163.71	164.41	166.93
E_1 (GPa)	=	211.00	211.56	212.99	212.36
E_2 (GPa)	=	215.89	216.60	216.09	
E_3 (GPa)	=	208.73	209.77	209.38	
$Q^{-1}{}_2(10^{-5})$*	=	9.94	6.40	7.26	
ν_{12}	=	0.2647	0.2627	0.2658	0.2880
ν_{13}	=	0.3047	0.3054	0.3042	
ν_{23}	=	0.2857	0.2850	0.2879	
ν_{21}	=	0.2708	0.2690	0.2696	
ν_{31}	=	0.3014	0.3028	0.2990	
ν_{32}	=	0.2762	0.2760	0.2790	

x_1 = rolling direction; x_2 = transverse direction; x_3 = plate normal
*Measured Young-modulus-mode internal friction in direction 2.

Table 2.3.1 (continued)

		CA (underaged)	C5 (optimum-aged)	C7 (overaged)
Q^{-1}_1 (10^{-5})*	=	8.47	9.53	7.99
Q^{-1}_2 (10^{-5})*	=	5.12	3.38	3.75
Q^{-1}_3 (10^{-5})*	=	15.4	4.41	3.64
Q^{-1}_{11} (10^{-5})	=	8.64	9.68	10.8
Q^{-1}_{22} (10^{-5})	=	15.4	2.70	5.58
Q^{-1}_{33} (10^{-5})	=	19.8	2.57	4.95
Q^{-1}_{44} (10^{-5})	=	19.5	7.06	11.9
Q^{-1}_{55} (10^{-5})	=	10.3	10.9	11.0
Q^{-1}_{66} (10^{-5})	=	9.58	10.0	10.4
Q^{-1}_B (10^{-5})	=	20.88	4.32	8.88
Q^{-1}_G (10^{-5})	=	13.30	7.99	8.45
Q^{-1}_E (10^{-5})	=	14.37	7.47	8.51
$Q^{-1}_{E_2}$*(10^{-5})	=	9.94	6.40	7.26

x_1 = rolling direction; x_2 = transverse direction; x_3 = plate normal
*Averaged Young-modulus-mode internal friction.

Table 2.3.2 Elastic coefficients and internal frictions of 1-2 and W1 steels.

		1-2	w1	Iron
ρ (g/cm^3)	=	7.8532	7.8339	7.872
C_{11} (GPa)	=	274.42	273.54	276.85
C_{22} (GPa)	=	274.44	274.50	
C_{33} (GPa)	=	274.49	273.40	
C_{12} (GPa)	=	110.34	110.19	111.97
C_{13} (GPa)	=	110.54	109.30	
C_{23} (GPa)	=	110.54	109.56	
C_{44} (GPa)	=	81.987	82.007	82.44
C_{55} (GPa)	=	82.011	82.234	
C_{66} (GPa)	=	82.001	82.202	
S_{11} (TPa^{-1})	=	4.738	4.745	4.709
S_{22} (TPa^{-1})	=	4.738	4.730	
S_{33} (TPa^{-1})	=	4.740	4.738	
S_{12} (TPa^{-1})	=	−1.356	−1.366	−1.356
S_{13} (TPa^{-1})	=	−1.362	−1.350	
S_{23} (TPa^{-1})	=	−1.362	−1.349	
S_{44} (TPa^{-1})	=	12.20	12.19	12.13
S_{55} (TPa^{-1})	=	12.19	12.16	
S_{66} (TPa^{-1})	=	12.20	12.17	
B (GPa)	=	165.13	164.39	166.93
E_1 (GPa)	=	211.07	210.74	212.36
E_2 (GPa)	=	211.08	211.42	
E_3 (GPa)	=	210.97	211.07	
ν_{12}	=	0.2863	0.2879	0.2880
ν_{13}	=	0.2874	0.2844	
ν_{23}	=	0.2874	0.2853	
ν_{21}	=	0.2863	0.2889	
ν_{31}	=	0.2873	0.2848	
ν_{32}	=	0.2873	0.2848	

x_1 = rolling direction; x_2 = transverse direction; x_3 = plate normal

Table 2.3.2 (continued)

		1-2	W1
Q^{-1}_{11} (10^{-5})	=	6.564	5.568
Q^{-1}_{22} (10^{-5})	=	5.599	6.356
Q^{-1}_{33} (10^{-5})	=	11.46	0.499
Q^{-1}_{44} (10^{-5})	=	10.23	13.28
Q^{-1}_{55} (10^{-5})	=	6.813	6.363
Q^{-1}_{66} (10^{-5})	=	5.396	12.70
Q^{-1}_{B} (10^{-5})	=	9.369	3.409
Q^{-1}_{G} (10^{-5})	=	6.735	8.557
Q^{-1}_{E} (10^{-5})	=	7.109	7.824

x_1 = rolling direction; x_2 = transverse direction; x_3 = plate normal

Table 2.3.3 Elastic-stiffness anisotropy defined as ratio of maximum to minimum shear-mode elastic-stiffness coefficients (C_{44}, C_{55}, C_{66}). Also, we show a similarly defined anisotropy for the internal friction Q^{-1}_{ij}.

Steel	C_{ij} anisotropy*	Q^{-1}_{ij} anisotropy
CA	1.062	2.04
C5	1.061	1.54
C7	1.058	1.14
1-2	1.000	1.89
W1	1.003	2.09

*For an isotropic material, this value equals 1.000. For polycrystal iron, the maximum-possible C_{ij} anisotropy equals $2C_{44}/(C_{11}-C_{12}) = 2.407$.

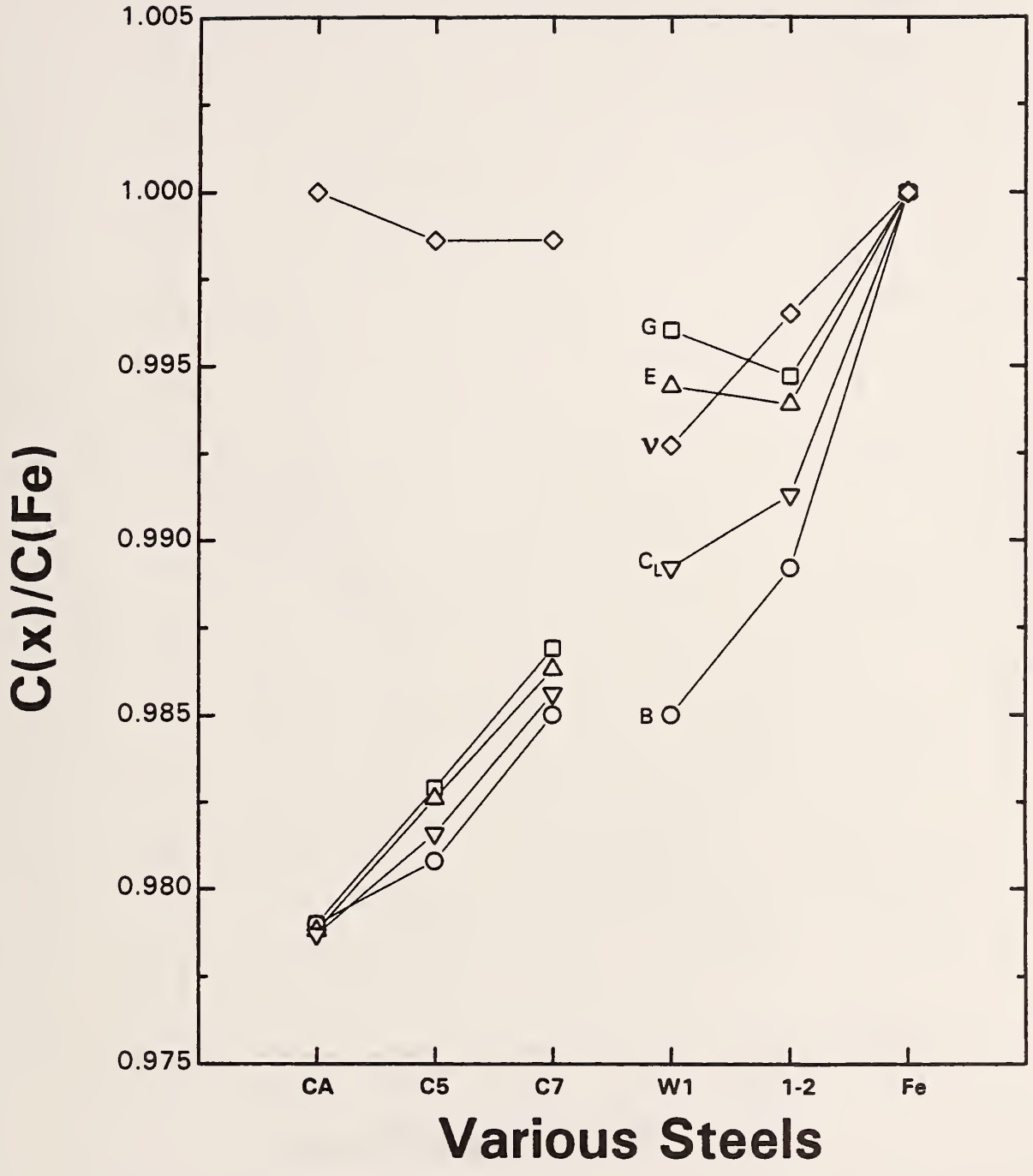

Fig. 2.3.1 Polycrystal (quasiisotropic) elastic stiffnesses for the five steels compared with iron. B = bulk modulus, C_L = longitudinal modulus, E = Young modulus, G = shear modulus, ν = Poisson ratio. Precipitation of atoms from solid solution increases stiffness.

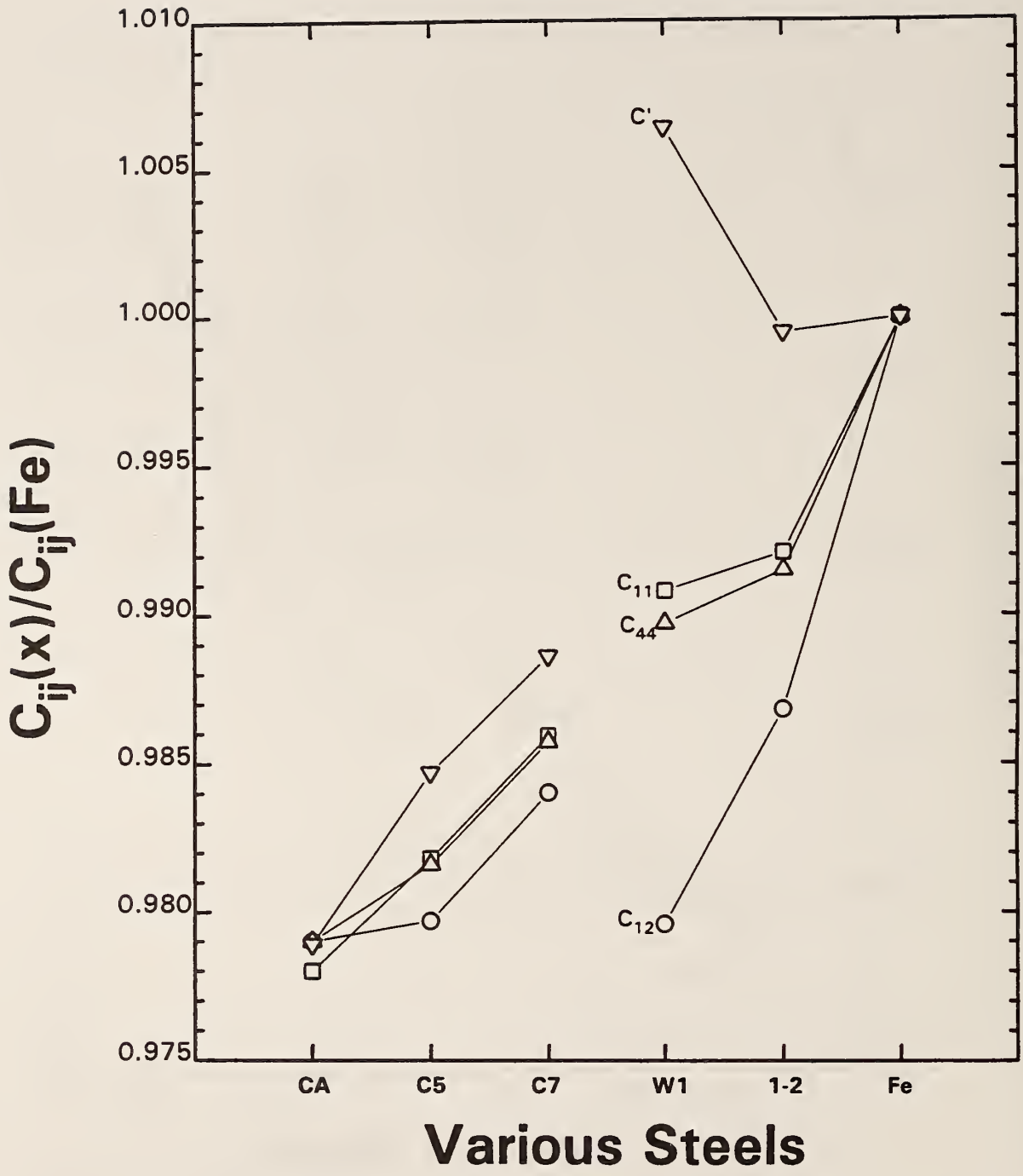

Fig. 2.3.2 Companion to Fig. 2.3.1. Derived monocrystal elastic stiffnesses. C_{11}, C_{12}, C_{44} = usual Voigt elastic coefficients, and $C' = \frac{1}{2}(C_{11} - C_{12})$. Anisotropic stiffness behaves similar to quasiisotropic case.

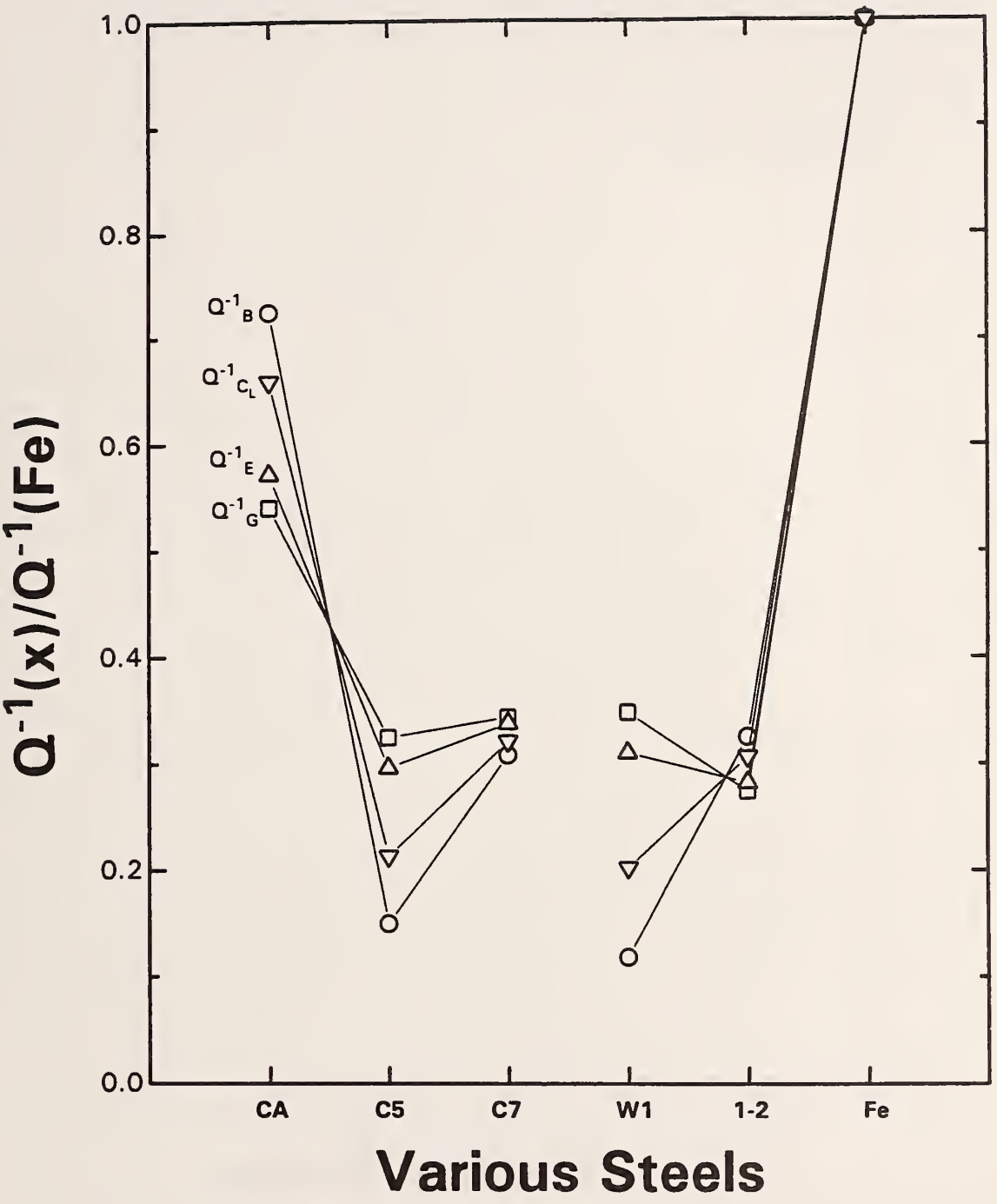

Fig. 2.3.3 Companion to Fig. 2.3.1. Shows internal friction Q^{-1} for various quasiisotropic modes. In the C steels, probably loss of precipitate coherency causes V-shape.

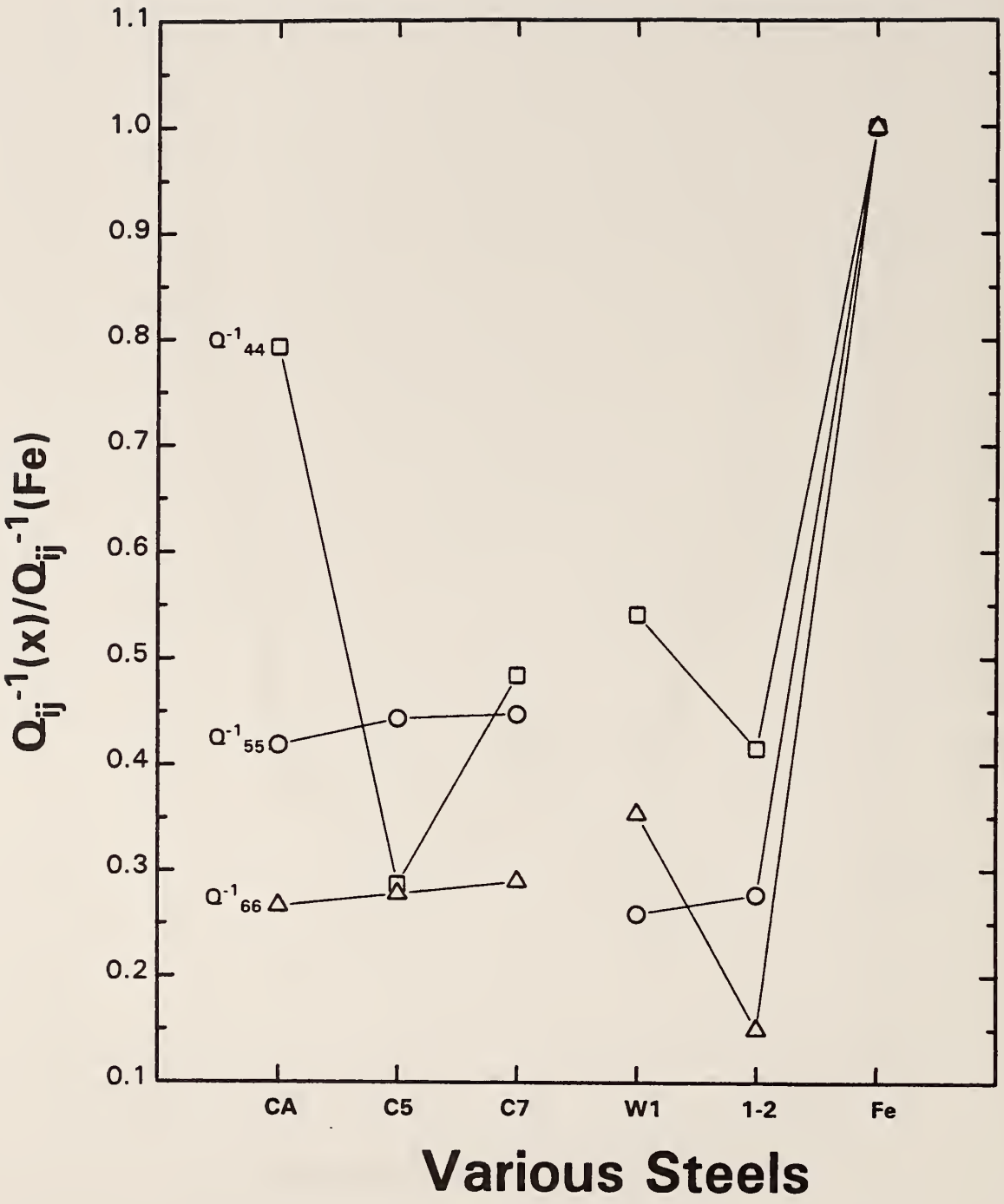

Fig. 2.3.4 Companion to Fig. 2.3.1 and 2.3.3. Shows Q^{-1} associated with the three anisotropic shear moduli. Different behavior for the 44, 55, 66 cases suggests anisotropic dislocation geometry.

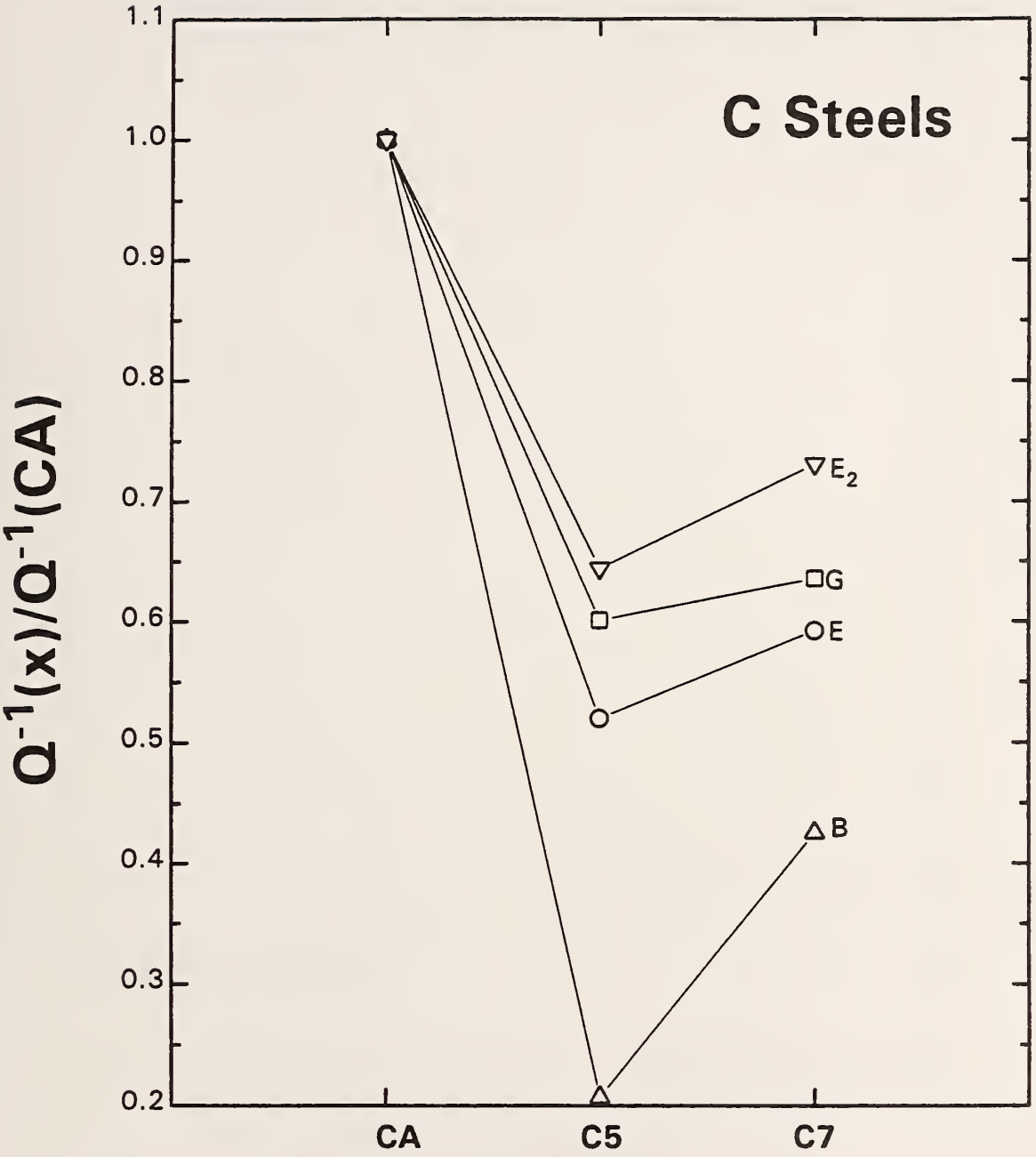

Fig. 2.3.5 Relative Q^{-1} values for C steels. E_2 refers to MOR measurements, E to ARS measurement. Two independent measurements confirm V-shape behavior.

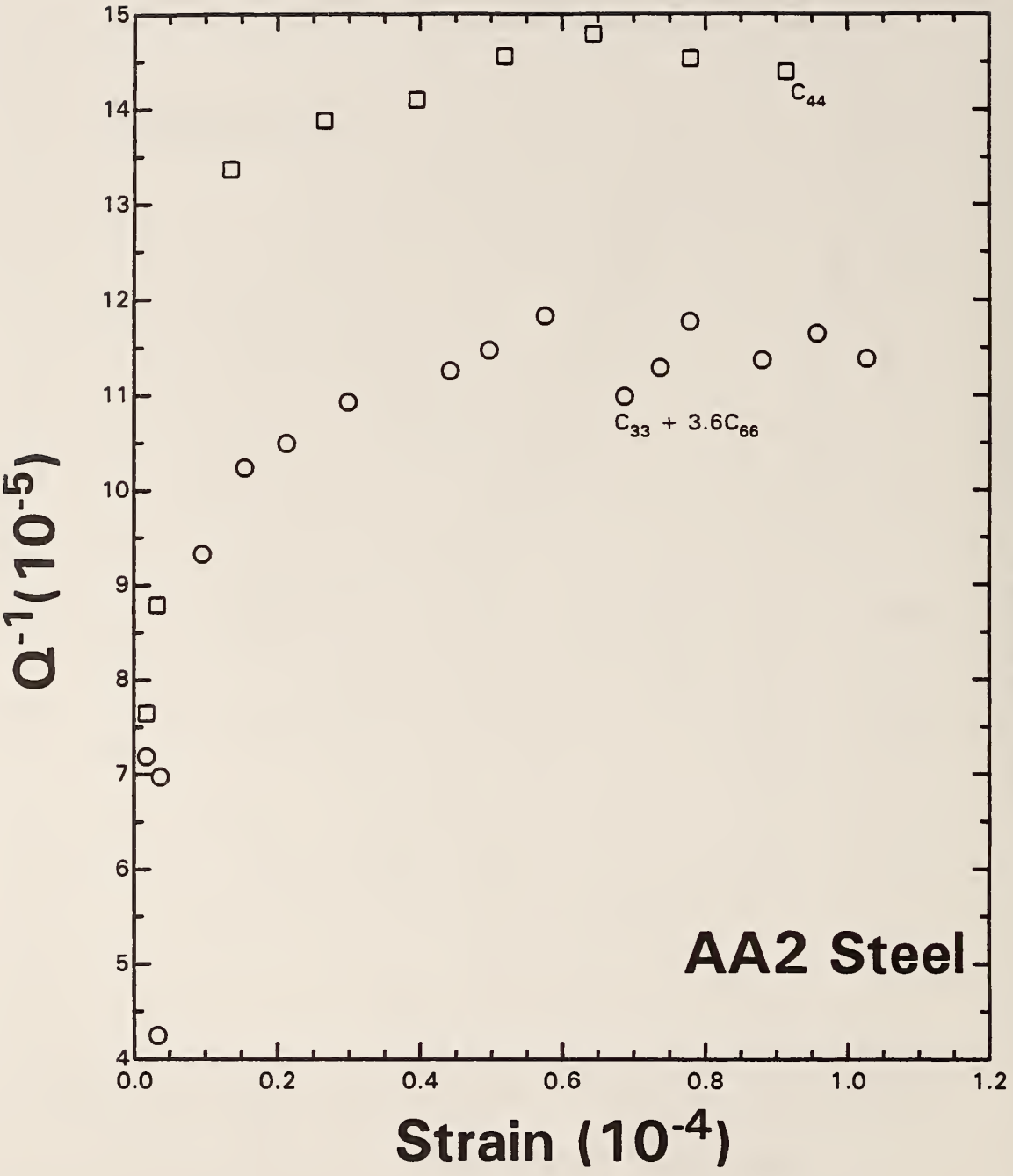

Fig. 2.3.6 Q^{-1} strain dependence. Both C_{44} and C_{66} represent shear modes. The AA2 steel is a lower-copper-content companion to the CA steel. Saturation above about 0.3×10^{-4} departs from usual Koehler-Granato-Lücke model.

Hypotheses to explain previous figure.

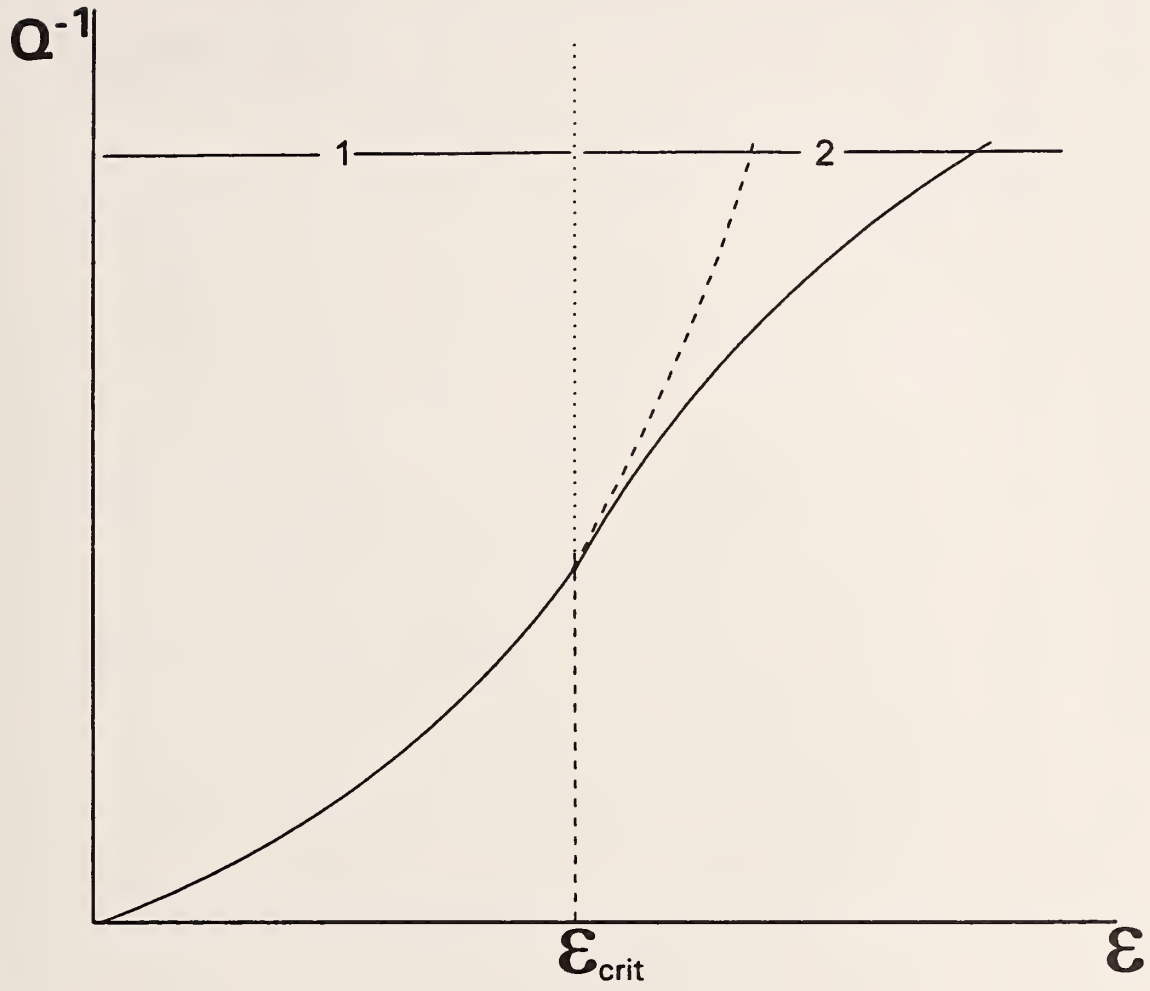

Region 1	Region 2
vibrating dislocation	moving dislocation
viscoelastic	microplastic
reversible	irreversible

Fig. 2.3.7 Companion to fig. 2.3.6. Possible interpretation of the Q^{-1} strain relationship. Low ε_{crit} means high ductility.

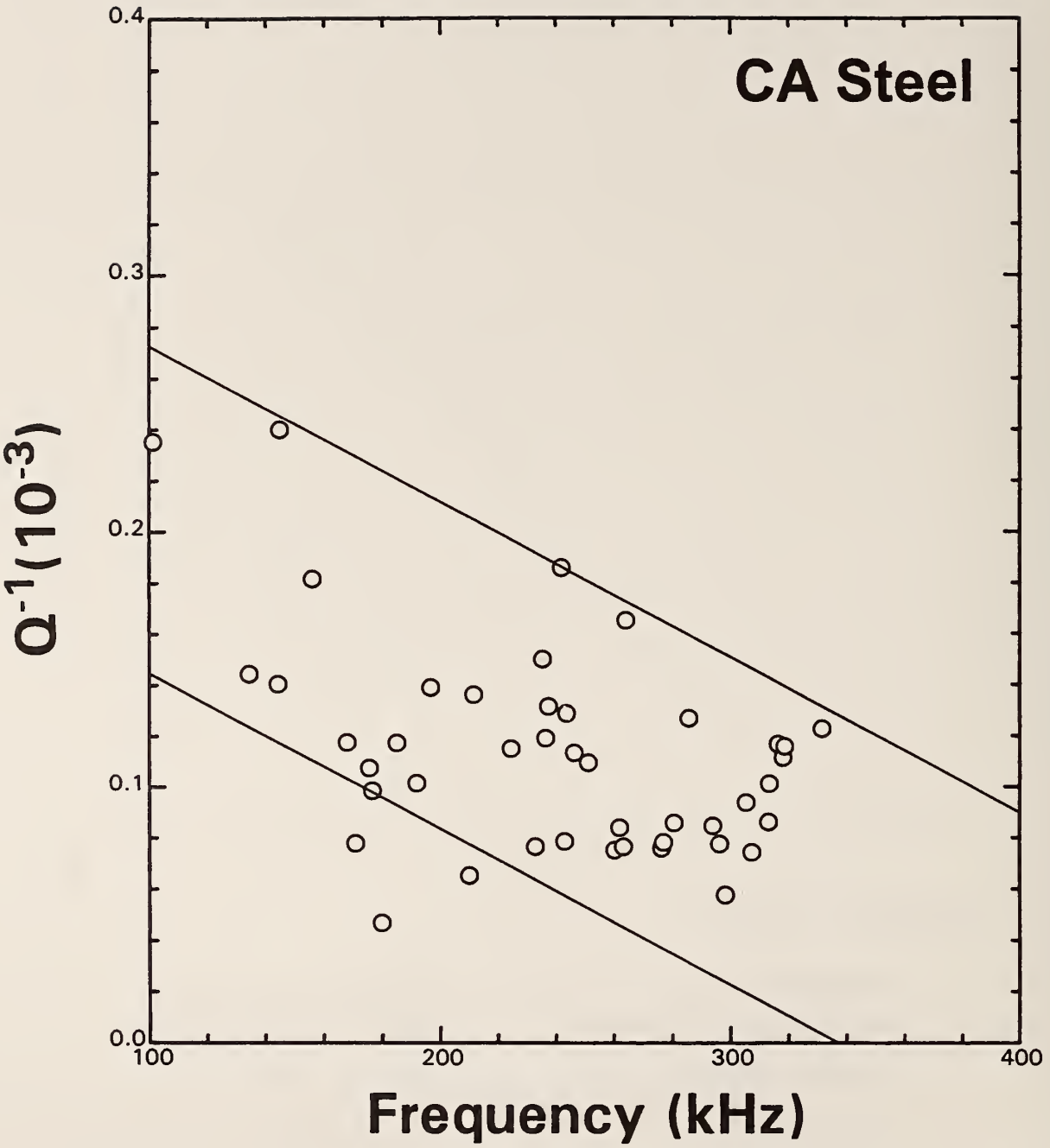

Fig. 2.3.8 Q^{-1} - frequency dependence. Surprising negative slope disagrees with usual dislocation and magnetic mechanisms. Scatter arises from various deformation modes.

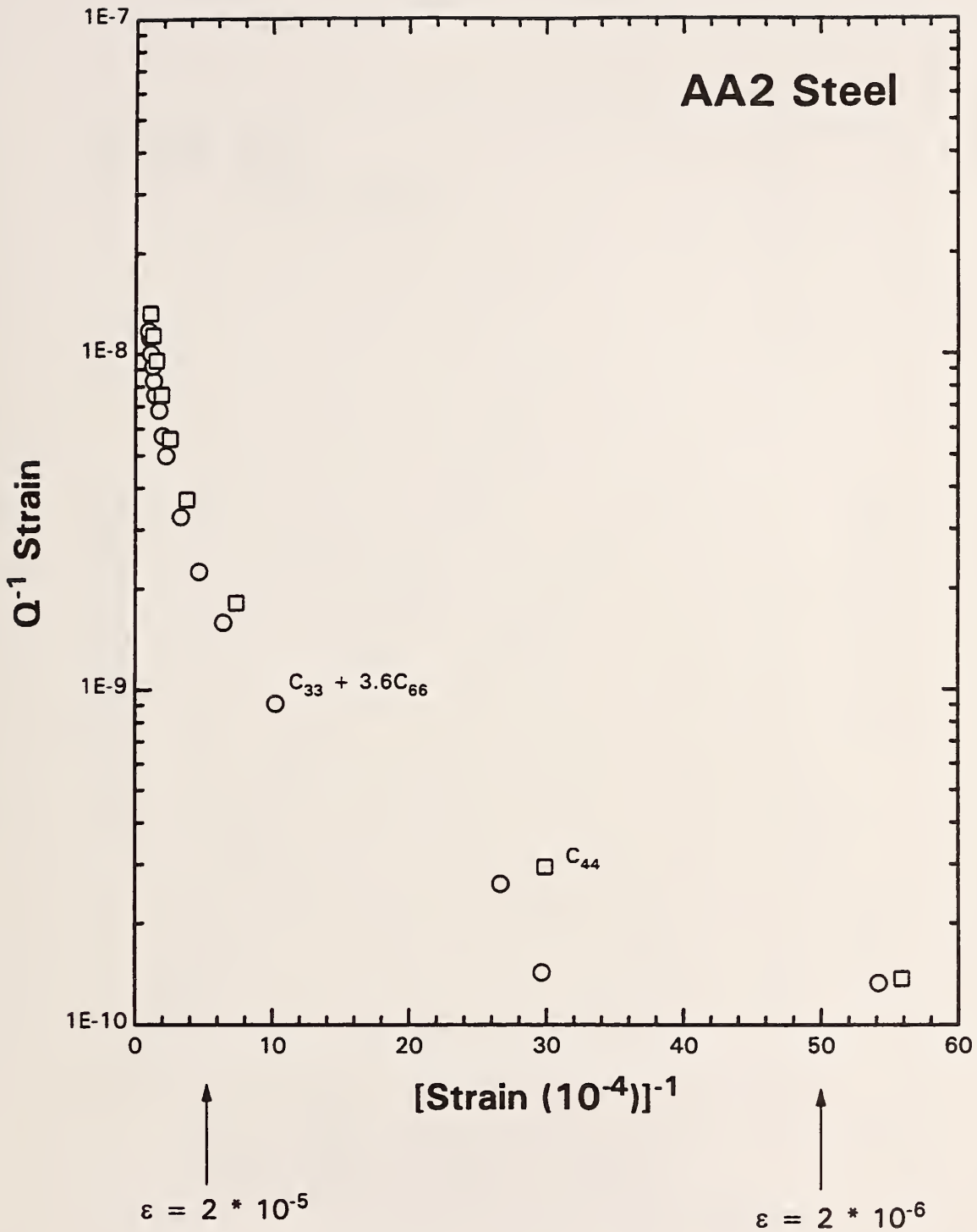

Fig. 2.3.9 Granato-Lücke diagram. The Koehler-Granato-Lücke model predicts linear behavior. Departure from linearity at low strains remains to be explained; it occurs in many materials. The AA2 steel is a lower-copper-content companion to the CA steel.

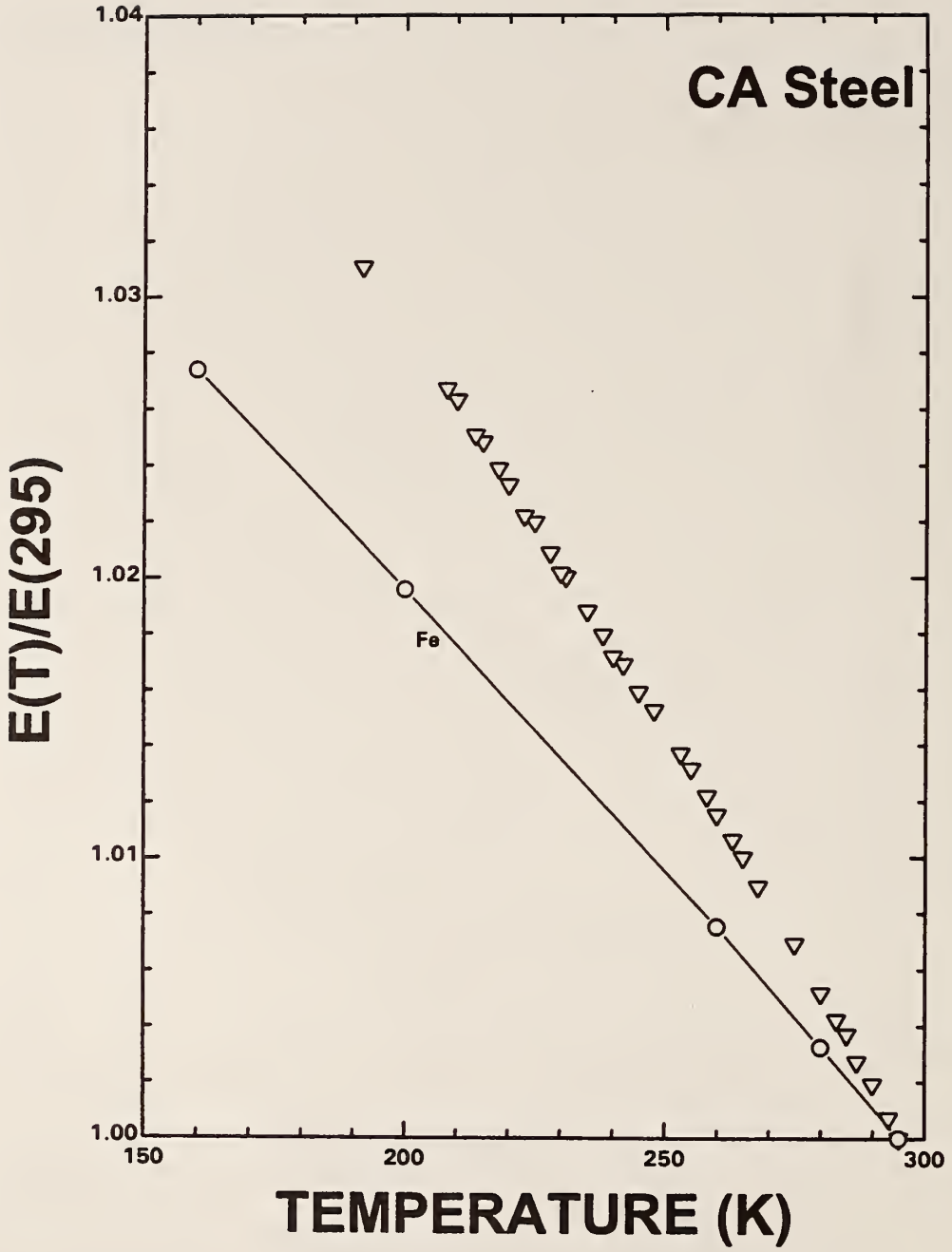

Fig. 2.3.10 Temperature variation of CA-steel Young modulus compared with iron. Measured using MOR method. Upon cooling through the ductile-brittle transition, no significant irregularity appears. (Data for iron, see Ref. [2.3.3].)

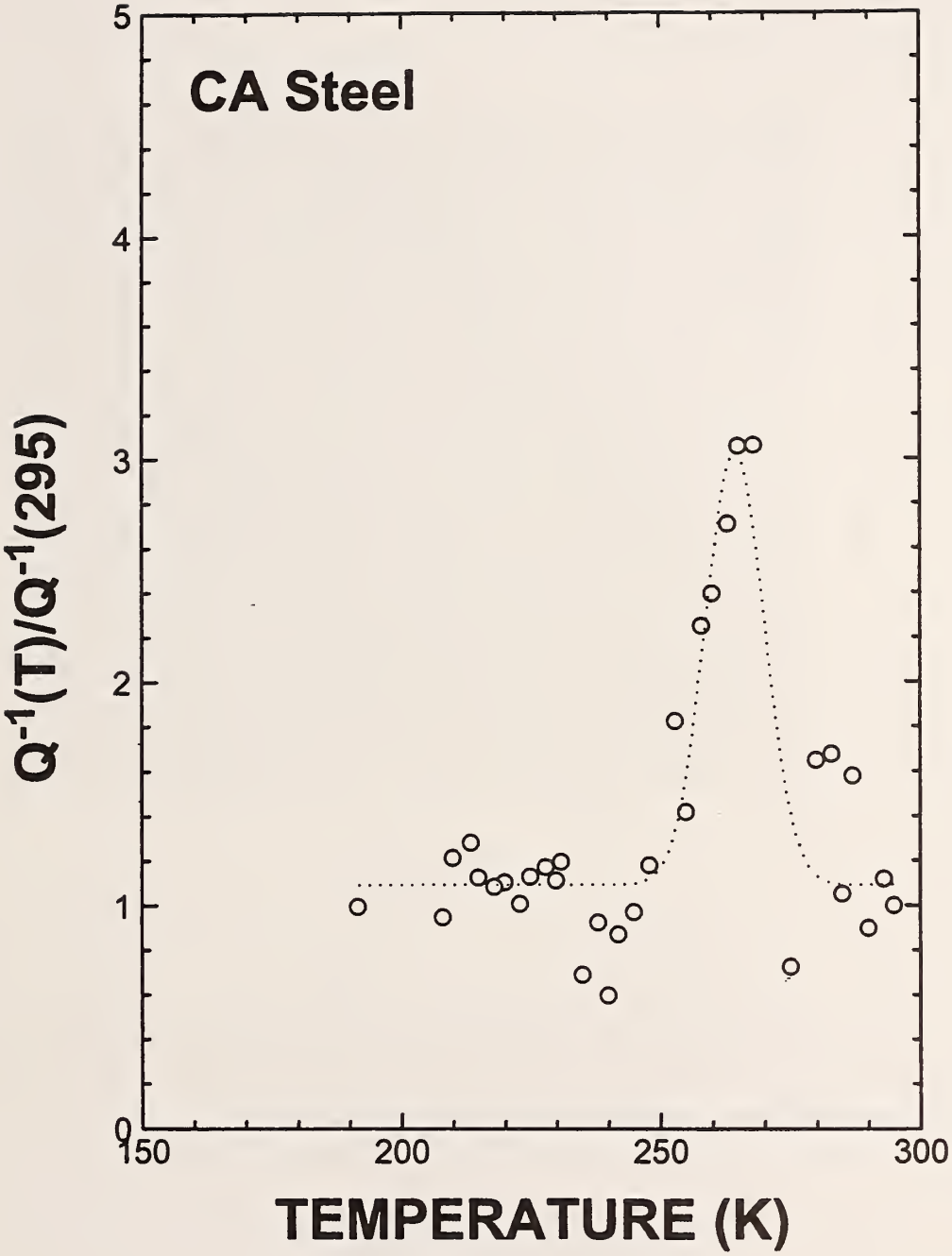

Fig. 2.3.11 Companion to Fig. 2.3.10. Peak in internal friction implies a relaxation process near 270 K, close to the ductile-brittle transition temperature.

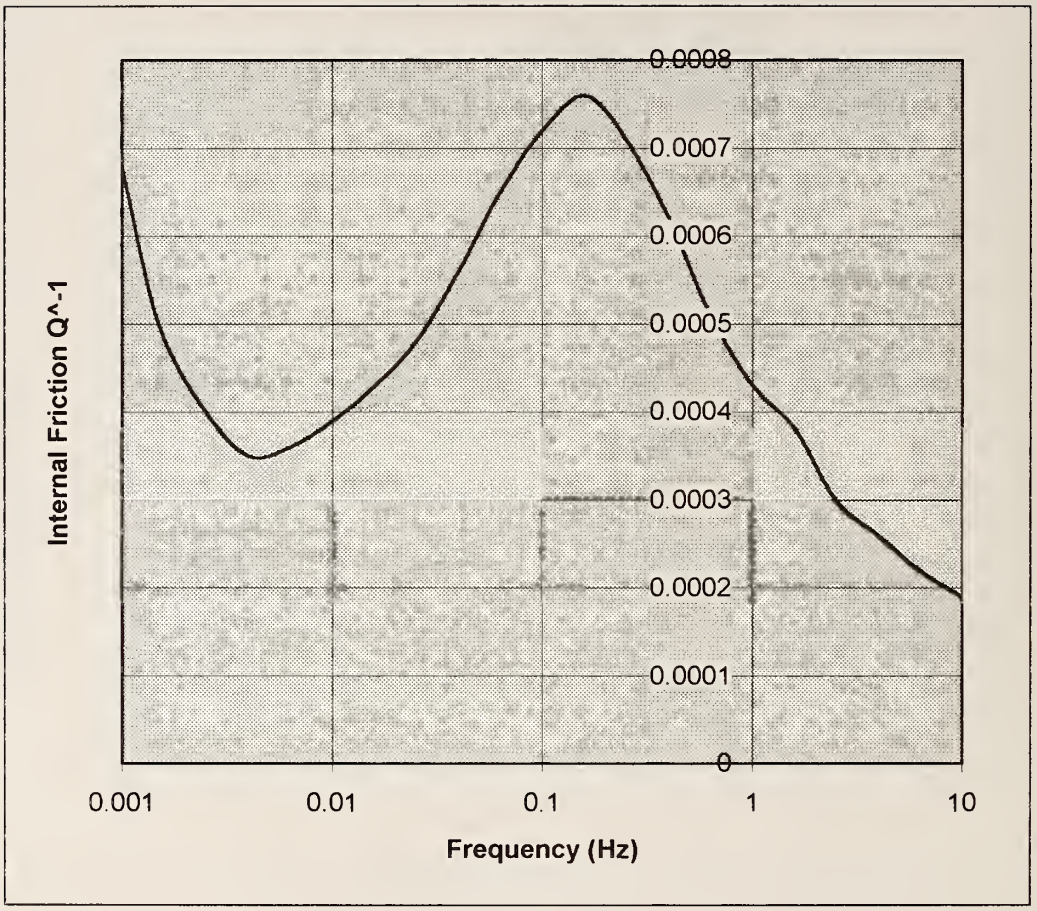

Fig. 2.3.12 Snoek peak of C5 steel. Measured at a non-NIST laboratory using a forced-vibration torsion pendulum. The Snoek peak arises from carbon-atom reorientation under stress. Replacing Fe-lattice atoms with other atoms (a ternary solute addition such as Cu) should change this peak: broadening, frequency shift, peak height, subpeaks.

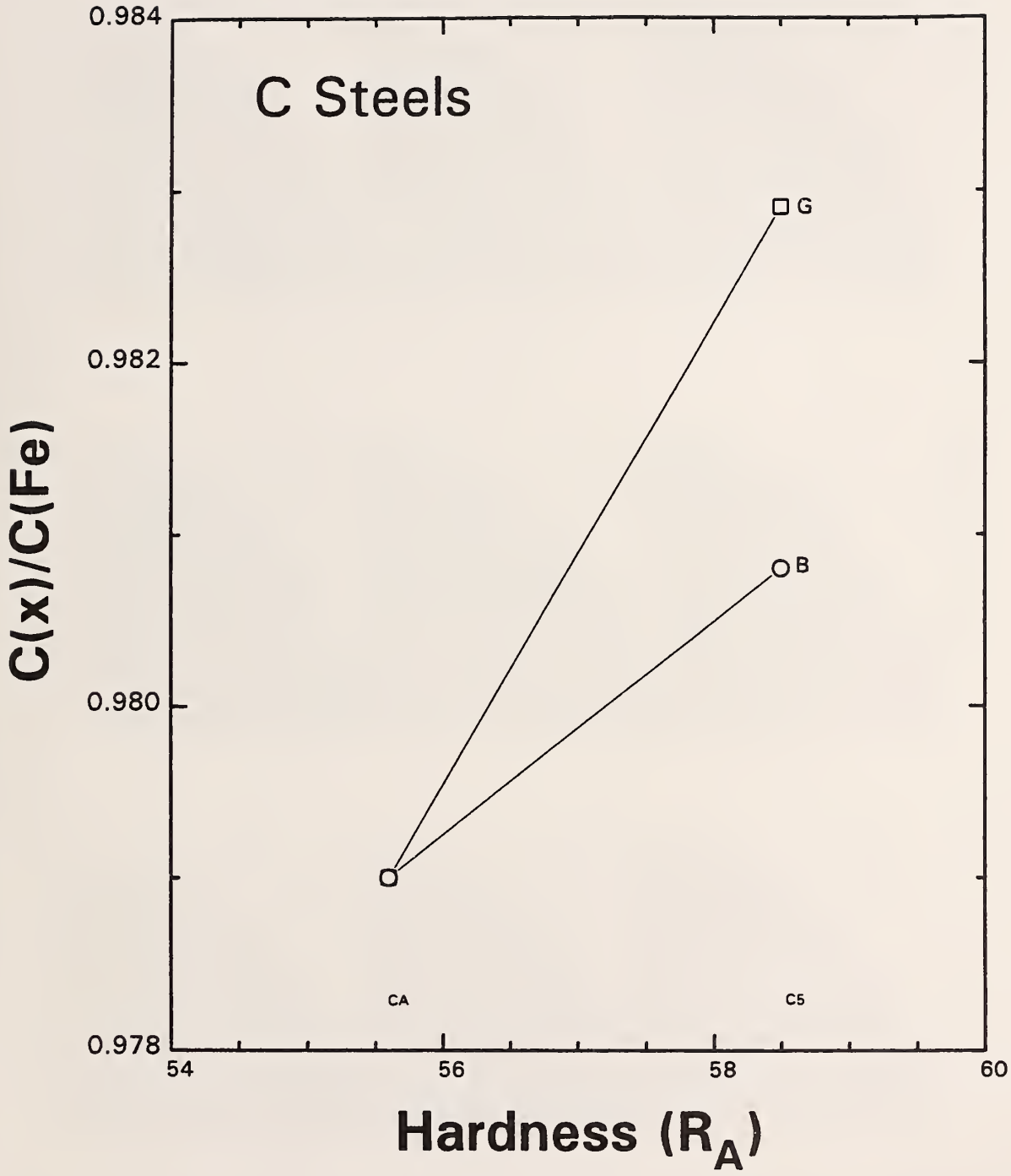

Fig. 2.3.13 Elastic-stiffness change with hardness.

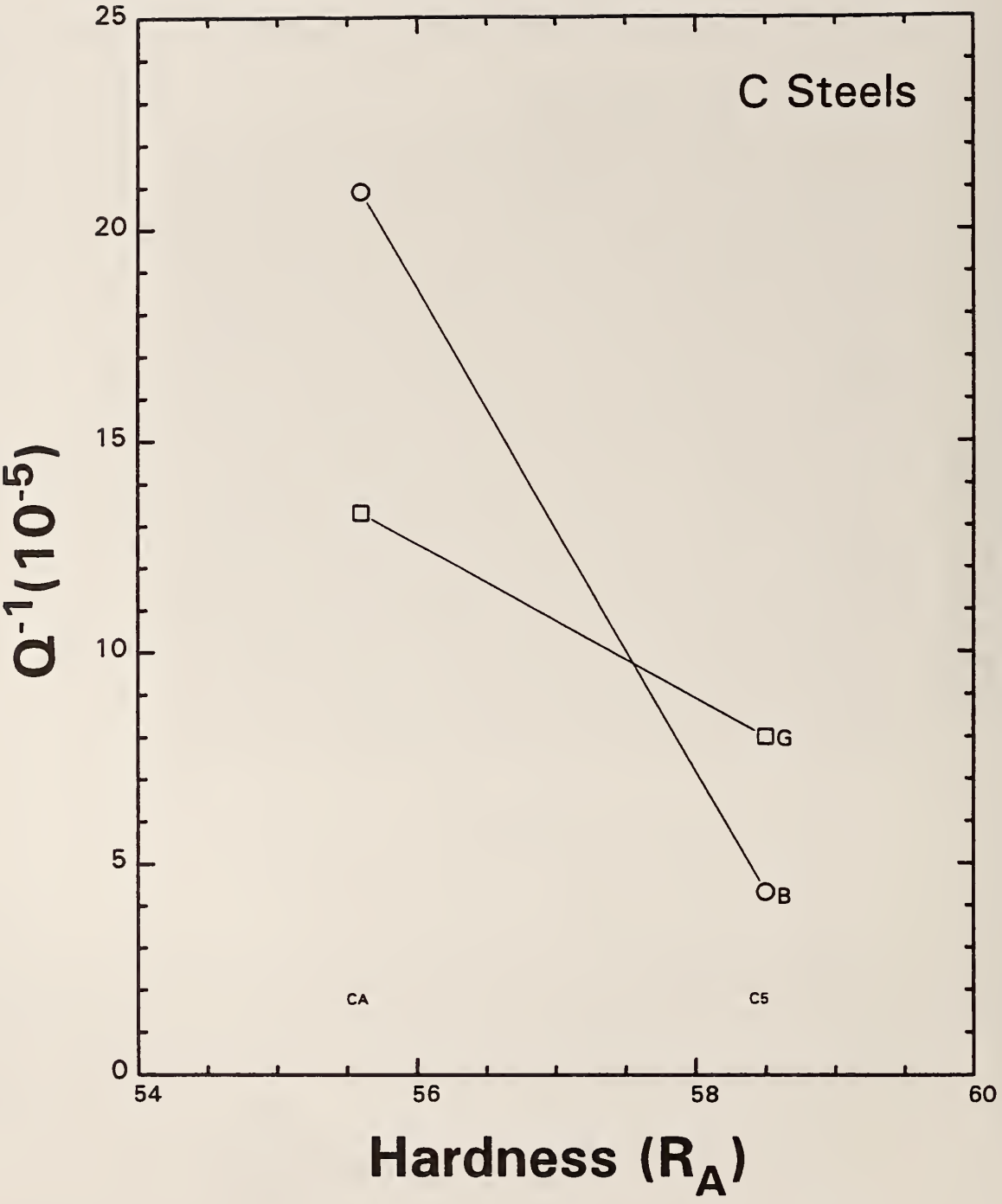

Fig. 2.3.14 Companion to Fig. 2.3.13. Q^{-1} change with hardness.

CA specimen

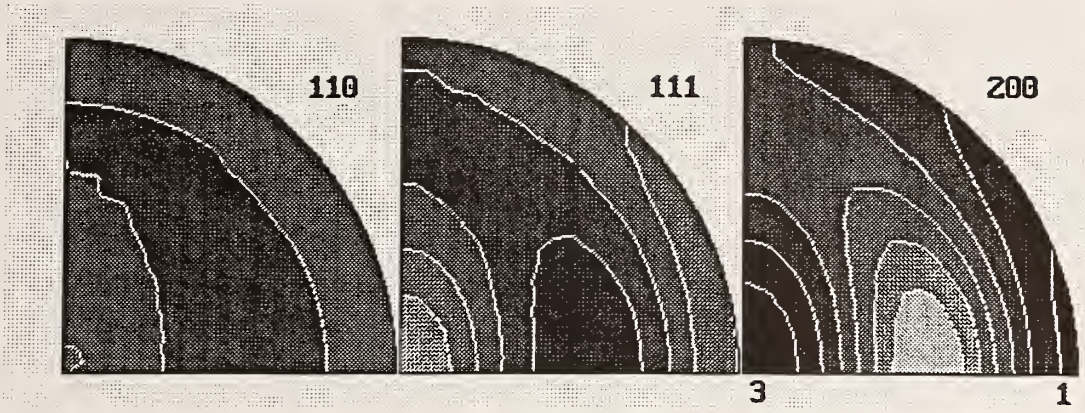

C5 specimen

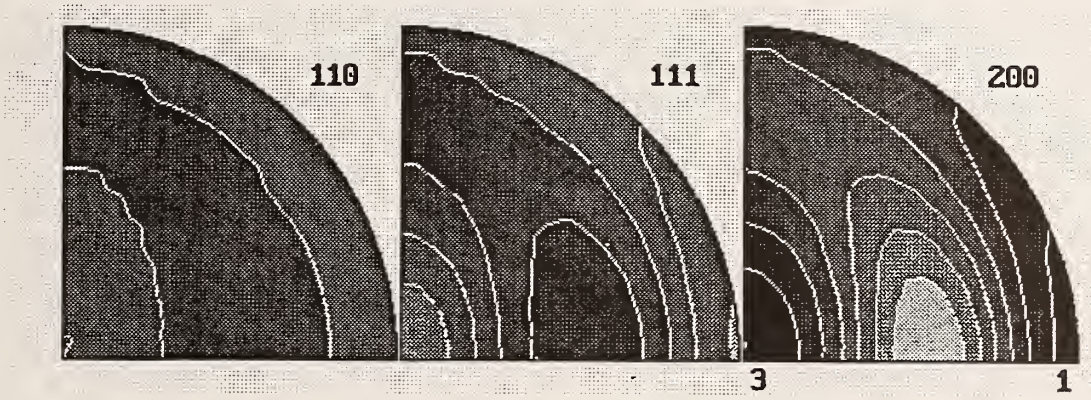

C7 specimen

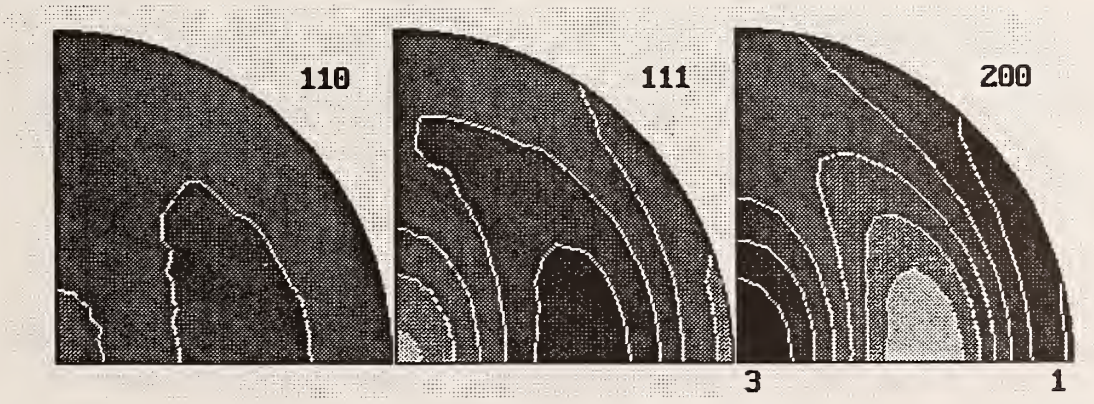

Fig. 2.3.15 Principal pole figures (100, 110, 111) derived from acoustic measurements, which yield the orientation-distribution coefficients W_{ijk}. These reveal texture (nonrandom-crystallite-orientation distribution).

2.4 X-RAY DIFFRACTION — *Davor Balzar*

2.4.1 Methodology

Because the X-ray strain gauge is so small, the diffraction method is sensitive to both macrostress (generally caused by any applied or residual macroscopic elastic and plastic deformation of material) and microstress (for instance, caused by elastic incompatibility of different grains in a single-phase material, different plastic deformation or thermal expansion coefficients of phases in multi-phase materials). Terminology used in the literature divides residual stresses into three kinds: Kind I – acting over macroscopic regions; Kind II – acting over sub-millimeter dimensions (such as grains); and Kind III – acting over sub-grain dimensions at the crystalline lattice level. The first two categories shift diffraction lines because the deformation is homogeneous throughout the sampling volume. Residual stresses of Kind III are visible mostly in line broadening, caused by localized inhomogeneous deformation associated with structural defects. Analysis of diffraction line-broadening can quantify both size-related defects (such as stacking and twin faults, low-angle and high-angle boundaries) and strain-related defects (namely dislocations, point defects, and distortions of the host lattice in the vicinity of coherent precipitates). Diffraction methods measure directly *strain* and not *stress*. Conversion between the two is provided by the way of macroscopic elastic constants. However, because the Kind III stress is localized on so small a scale (in the 1 to 100 nm range), the simple linear elastic-continuum approximation may not be valid. Therefore, we have chosen here to report only on the measured quantity: the strain.

2.4.2 Experimental Technique

Specimens CA, C5, and C7 were prepared by polishing and etching one surface. The average x-ray sampling volume was about 15 mm × 3 mm × 5 μm. Measurements were made on a horizontal goniometer with $CuK\alpha_{1,2}$ radiation in a high-resolution setup. The complete diffraction patterns were collected (six Bragg reflections for the ferrite structure) and showed peaks from only the α-Fe phase plus a few very weak peaks of unknown origin. It is not possible to distinguish between the peaks from the main ferrite phase present and bainite, but because no carbide peaks were observed, the contribution of bainite should be minimal. The diffraction patterns exhibited relatively strong texture, but this varied greatly among the specimens and may depend on how the specimens were cut. (See Fig. 2.3.15 for pole figure information.)

2.4.3 Results

The diffraction patterns were modeled with a Rietveld-refinement program. The refined lattice parameters did not differ significantly, which indicates no change of hydrostatic strain or chemical composition between the specimens. Line broadening was moderate in all three specimens, but it did differ significantly, especially between C5 and C7 specimens. Preliminary diffraction-line broadening analysis indicated an insignificant effect of anisotropy and only the isotropic line-broadening parameters were refined by the Rietveld program. Coherent-domain size

and strain were estimated from refined diffraction-line full-widths-at-half maximum, which were corrected for instrumental line broadening. The refined domain sizes were larger than about 300 nm (which indicates a very small contribution to line broadening), and increased monotonically but not significantly from CA to C5 to C7. Strain-induced broadening was dominant, although the magnitude was not large (less than 0.1%). Strain values are presented in Table 2.4.1 for the C-series, 1-2, and W1 specimens, and are plotted as a function of hardness in Fig. 2.4.1. A good linear correlation is evident. Different offsets for the A-series and C-series of specimens may indicate somewhat different physical mechanisms of broadening in the two alloy types. Fig. 2.4.2 shows a good correlation between strain and ultimate tensile strength, as well.

2.4.4 Physical Model

Because it is difficult to prevent the formation of copper-rich precipitates, the CA specimen probably contains a relatively large number density of such precipitates. However, they are probably significantly smaller than those in the C5 specimen. This is confirmed by relatively higher strain and hardness of the CA compared to the C7 specimen. There is a sharp drop in strain between the C5 and C7 specimens. A possible explanation for this is that the coherent copper-rich precipitates, which are of optimum size in the C5 specimen, coarsen due to higher and prolonged annealing temperature (overaging), thus becoming incoherent with the matrix, which in turn relieves the matrix strain. Moreover, the effect may be accompanied by a simultaneous decrease in dislocation density because coarser precipitates do not pin dislocations so efficiently and the material has been subjected to an annealed higher temperature. The reason that a drop in hardness and ultimate tensile strength is not accompanied by a decrease in the proportional limit (see Fig. 2.2.2) may simply be because there is an overall lower dislocation density in the C7 material compared to the C5 specimen.

Table 2.4.1 Strain deduced from diffraction line-broadening analysis.

Specimen	Strain (10^{-4})
CA	6.9(5)
C5	7.4(1)
C7	5.3(5)
1-2	7.3(1)
W1	7.7(1)

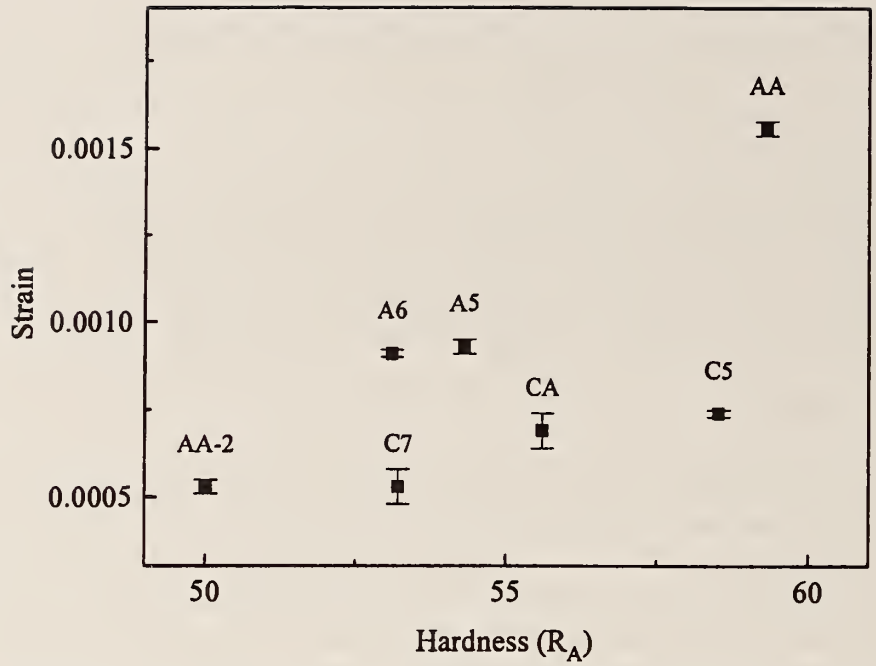

Fig. 2.4.1 Relationship between internal lattice strain and hardness for the A710 steel (CA, C5, and C7) and the 1508 steel (AA, AA-2, A5 and A6).

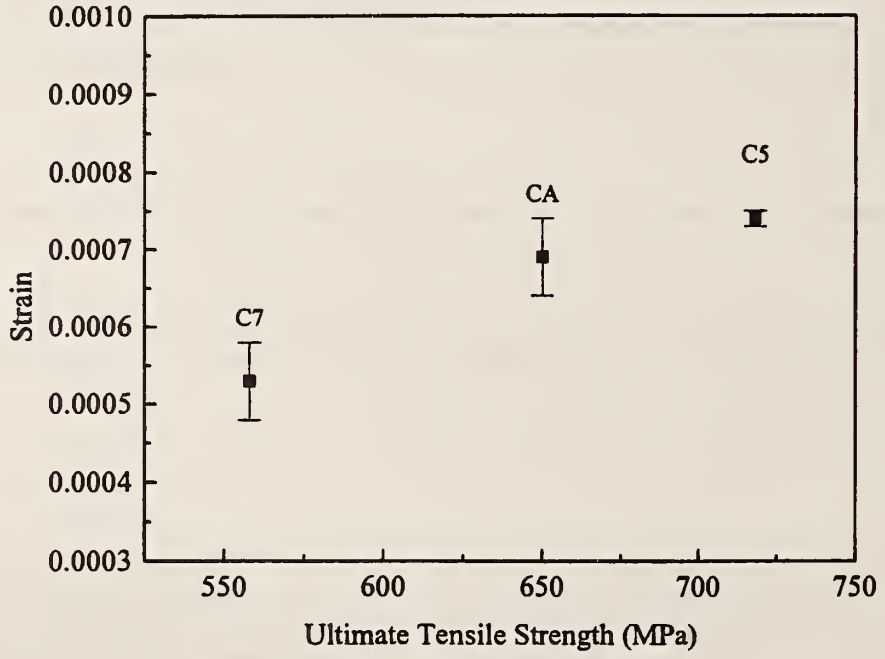

Fig. 2.4.2 Relationship between internal lattice strain and the ultimate tensile strength for the A 710 alloy in the overaged (C7), the solution treated (CA), and the peak-aged (C5) condition.

2.5 NONLINEAR ULTRASONIC PROPERTIES—Donna Hurley

2.5.1 Background

When an ultrasonic wave at a frequency ω and amplitude A_1 propagates through a solid, nonlinear terms in the force-distance relationship that describes the interatomic forces cause the generation of a wave at frequency of 2ω (a second harmonic). The amplitude of this second harmonic wave A_2 increases with distance and with the square of the amplitude A_1. By measuring A_2 relative to A_1, it is possible to deduce the value of a parameter β that is related to the nonlinear terms in the interatomic force relationship and is, therefore, a physical property of the solid. Harmonic generation experiments were performed on eight steel samples in order to determine their nonlinear ultrasonic parameters and to establish their relationship to the microstructures. Three of the samples contained 1.13% copper (the "C" series) and three contained 0.35 mass percent copper (the "A" series). The remaining two samples were extracted from the SNUPPS reactor vessel and consisted of A533B steel from the region adjacent to a weld (sample 1-2) and from the weld itself (sample W1). The "C" and "A" samples had received different heat treatments in order to vary their mechanical hardness, as described in Section 2.1 of this report.

2.5.2 Experiments

In the experiments, a tone burst of finite amplitude and at a frequency of 9.8 MHz was launched with a piezoelectric transducer bonded to one side of the specimen. The absolute displacement amplitudes of the wave components at ω (fundamental) and 2ω (second harmonic) were measured on the other side of the specimen using an infrared, path-stabilized Michelson interferometer. Experimental techniques for determining β in this way have been described in detail elsewhere [2.5.1]. Values for β were calculated from the ratio of the fundamental and second-harmonic wave amplitudes together with values for ω, the longitudinal velocity v_L and the sample thickness. (The velocities were measured by K.W. Hollman using a high-precision pulse-echo superposition technique [2.5.2].) Physically, β is defined in terms of the second and third-order elastic stiffness moduli. For the experiments performed here, $\beta = -(3 + C_{111}/C_{11})$.

2.5.3 Results

The experimental results are summarized in Table 2.5.1. It lists both the absolute value of β and its value β' relative to that for the C7 specimen. By using relative values, it is possible to eliminate common sources of measurement uncertainty and thus reduce the relative uncertainty to $\pm$ 2%. Also given are values for the residual strain as determined by x-ray diffraction line-broadening experiments (discussed in Section 2.4 of this report).

Table 2.5.1 Compilation of measurements associated with nonlinear elasticity.

Sample	Hardness (HRA)	β	β' (relative)	v_L(m/s)	ε(10^{-4})
C7	53.2±0.5	4.81±0.29	1	5906±10	5.3±0.5
CA	55.6±0.5	5.16±0.31	1.07±0.02	5885±10	6.9±0.5
C5	58.5±0.5	5.36±0.32	1.11±0.02	5898±10	7.4±0.1
AA2	50.0±0.5	5.64±0.34	1.17±0.02	5903±10	N/A
A6	53.1±0.5	5.42±0.33	1.13±0.02	5906±10	9.1±0.1
A5	54.3±0.8	5.66±0.34	1.18±0.02	5906±10	9.3±0.2
1-2	53.3±0.8	5.30±0.32	1.10±0.02	5912±30	7.3±0.1
W1	57.0±0.5	6.56±0.39	1.37±0.02	5917±30	7.7±0.1

2.5.4 Discussion

The results for the three C series specimens are plotted in Fig. 2.5.1 as a function of hardness. This figure reveals that β changed markedly with sample hardness and increased by 11% over a hardness change of about 10%. We think that this behavior is due to changes in the copper precipitate strain configuration with tempering—precipitate formation and growth of coherency strain, then gradual loss of coherency through coarsening. At peak hardness (C5 sample), the precipitate is fully coherent and the surrounding region contains a great deal of strain. In overaged material (C7 sample), the precipitate becomes incoherent, relieving the strain. The nonlinear ultrasonic experiments measure an average strain in the bulk of the sample and, therefore, they should be sensitive to the relative state of precipitate coherency [2.5.3]. A comparison of the nonlinearity parameter β with the x-ray strains, given in Figure 2.5.2, shows an excellent correlation. Since nonlinear ultrasonic experiments probe bulk, and not just near-surface, properties (as in the case of the x-ray experiments), these results offer promise for nondestructive characterization of precipitate strain. Further experiments are being planned to obtain a more systematic understanding of this behavior.

The correlation between strain and the nonlinear parameter β for the C series leads us to ask whether the remaining data exhibit similar trends. Accordingly, all of the experimental results for β as a function of strain are plotted in Fig. 2.5.3. This figure reveals that β increases approximately linearly with strain for all of the samples measured, including the A533B reactor steel, *except* for the weld specimen (W1). In the weld specimen, precipitate strain is probably not the only microstructural feature that contributes to harmonic generation. Therefore, the weld

specimen results serve as a reminder that the absolute value of β cannot be interpreted as a direct reading of the microstrain, although the relative values may be useful to assess the relative state of strain.

2.5.5 References

2.5.1 Hurley, D.C.; Fortunko, C.M.; Determination of the nonlinear ultrasonic parameter β using a Michelson interferometer, Meas. Sci. Tech. 8: 634; 1997.

2.5.2 Renken, M.R.; Kim, S.; Hollman, K.W.; Fortunko, C.M.; Accuracy of Resonant Ultrasound Spectroscopy: an Experimental Study, Proc. 1997 IEEE Ultrason. Symp., Vol. 1, 97CH36118, ISSN 1051-0117, p. 483.

2.5.3 Cantrell, J.H.;Yost, W.T.; Effect of precipitate coherency strains on acoustic harmonic generation, J. Appl. Phys. 81:2957; 1997.

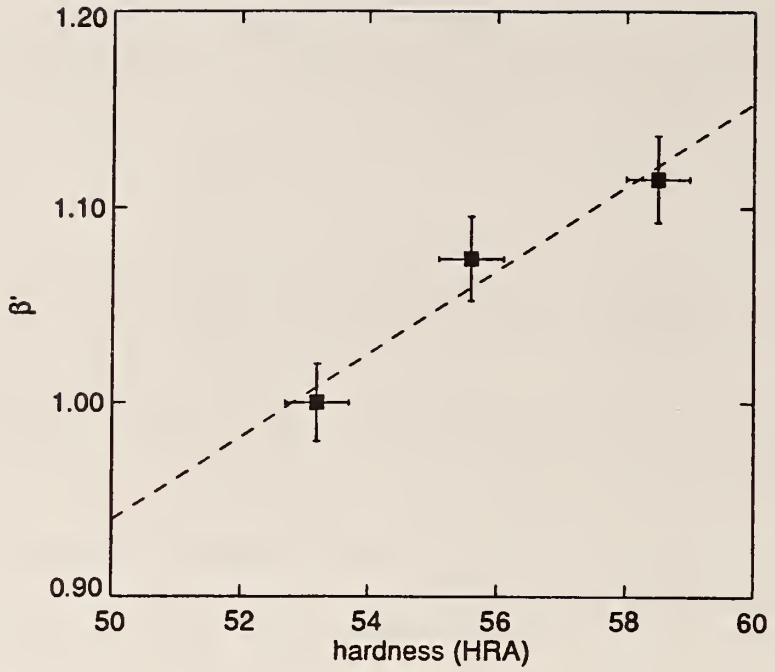

Fig. 2.5.1 Relationship between the nonlinearity parameter β and the Rockwell A Hardness of the A710 alloy after heat treatment to different hardness levels.

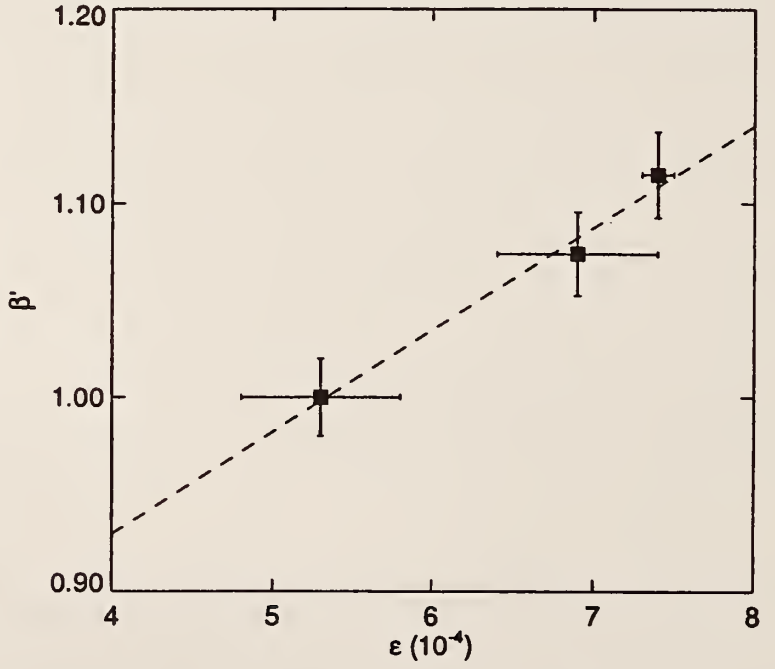

Fig. 2.5.2 Relationship between the nonlinearity parameter β and the internal lattice strain deduced from X-ray diffraction line broadening.

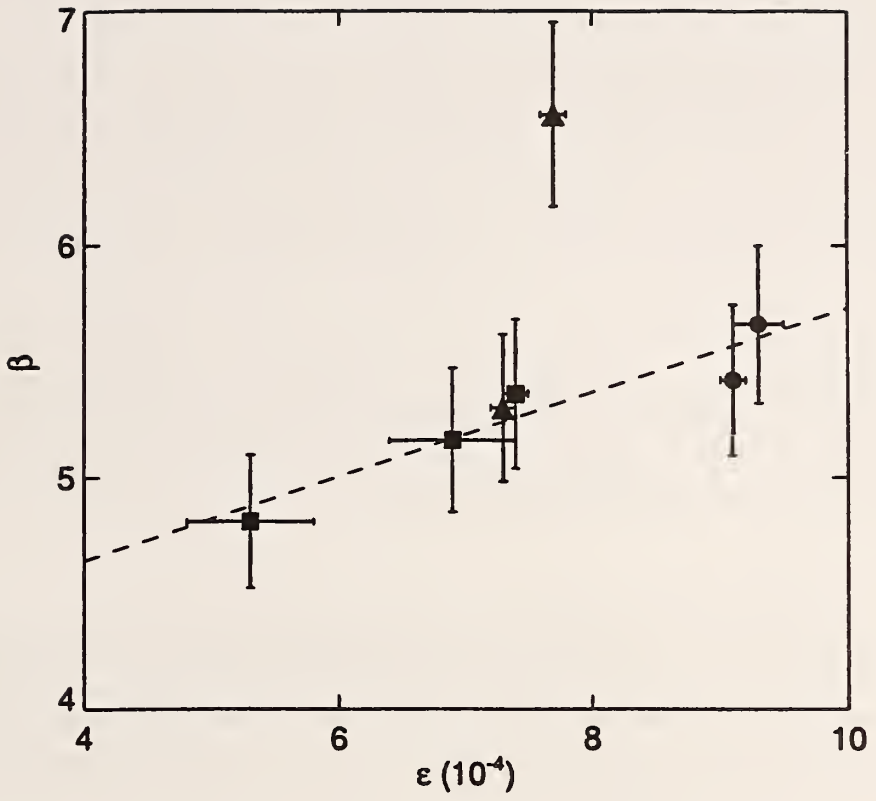

Fig. 2.5.3 Relationship between the nonlinearity parameter and the internal lattice strain for the A710 alloy (squares), the 1508 alloy (circles) and the A533B alloys (triangles).

2.6 MAGNETIC PROPERTIES — *Fred Fickett*

2.6.1 Introduction

Magnetic measurements for detecting embrittlement of the reactor steels are not new. The interaction of moving domain walls with lattice defects of various sorts is well known as a pinning mechanism that shows up as dramatic changes in the magnetic coercivity with relatively small changes in defect type or concentration. Other magnetic parameters, such as permeability, remanence, and saturation magnetization, also offer the potential for providing information on specific defect or compositional effects, although in all cases the interactions are very complex. Magnetic measurements offer one of the best chances for a detection system that can be used in the actual pressure vessel environment where the detection must be done through a relatively large thickness of stainless steel cladding, which normally is a nonmagnetic material. In this part of the project, we are looking at steels of various compositions with conventional magnetic measurement systems. These data will form the basis for interpretation of the necessarily less sophisticated measurements to be made in the field.

2.6.2 Literature Review

The existing literature on magnetic properties of reactor steels was reviewed. Much of the literature is embodied in a series of progress reports to the NRC over a large number of years as well as conference papers based on those reports: a lot of paper and not many data. The final report was published just last year and is available only on microfiche. Measurement techniques used were mostly of the large-sample B-H looper type. At best, existing data on the effect of the precipitates on magnetic properties are inconclusive. Interestingly, it seems that no precise magnetic measurements, such as can be made with the vibrating-sample magnetometer, have yet been done.

2.6.3 Vibrating Sample Magnetometer (VSM) Measurements

The VSM is a laboratory instrument that will almost certainly not be adaptable to field use. However, it gives the best direct data on the magnetic properties of the bulk steel. Specifically, it is capable of measuring the entire hysteresis loop of the sample, from which all of the static magnetic parameters can be obtained. These data will be needed as baseline or input to actual field measurements as well as for the detailed understanding of the magnetic behavior of the steels. At this stage of the investigation, the instrument allows us to answer many questions quickly and easily.

2.6.4 Apparatus

The VSM concept is shown in the Fig. 2.6.1. The steel sample is vibrated in an applied (variable) magnetic field and the moment induced by the field is detected by a set of pickup coils next to the sample. Clever design of the pickup coil and sophisticated modern electronics allow

various sources of error to be corrected out so that the final readout is a voltage proportional to the magnetic moment of the sample. The VSM borrowed for the tests reported here had been optimized for very low level magnetic measurements and our samples are at quite the other end of the scale. Test runs on nickel and steel samples indicated that the apparatus and the associated data acquisition programs needed modification to accurately measure materials of high magnetic moment. The VSM coil set and the location of the applied field magnetic Hall probe pickup were modified to avoid interactions between the sample and the probe. A VSM always has to be calibrated with a sample of known moment, preferably of the same size and shape as the samples to be measured. In our experiments, this was done with a pure nickel sample.

2.6.5 Samples and Sample Preparation

In all cases, the steel samples measured were in the form of rods 2 mm in diameter by 20 mm in length cut by electric-discharge machining (EDM) from the bulk material with their length in the plane of the sheet, essentially at the center of the thickness. Specimens were prepared from three steels, the A710 steels (CA, C5, C7), the 1508 steels (AA, A5, A6), and A533B (1-2) and a welded A533B (W1).

The calibration sample was cut from a 2 mm rod of pure nickel (99.9945% Ni). Because of the purity, the saturation moment was easily calculated and it is that number that calibrates the VSM at the beginning of each set of measurements.

2.6.6 Data and Calibration Runs

As mentioned above, the calibration run with the nickel sample was made frequently, necessitated in large part because the instrument was used by a number of people in the course of a week and the calibration quickly degrades if major changes have been made to the apparatus. Although, the calibration data consist of only the saturation magnetization of the sample, complete hysteresis loops, as described below, were always run.

For each of the steel samples, two types of measurements were made: The first was a hysteresis loop extending to 240 kA/m (3000 Oe) applied field and starting with magnetization to −240 KA/m (−3000 Oe). Each of the 200 points on these loops is a dc measurement, i.e. the applied field was stationary during the actual moment measurement. This curve was used to determine the coercivity. The second curve was started at zero field with a demagnetized sample and taken to 368 kA/m (4600 Oe) on a coarser grid of 75 points. This curve was used to determine the saturation magnetization. The measurements described above were completed on one sample of each of the steels for a total of 16 data runs.

2.6.7 Data Analysis

To date, analysis of the data to determine the saturation magnetization and the coercivity of the steel samples has been completed. In essence this involves plotting the portion of the loop

Table 2.6.1 Values for the magnetic parameters measured with the VSM.

Sampe	Condition	H_3(Oe)	H_c(A/m)	$\mu_0 M_S$
CA	Solution treated	8.39	668	2.03
C5	Peak aged	8.07	642	2.07
C7	Overaged	6.10	485	2.06
W-1	Welded A533B	8.95	712	2.05
1-2	Bulk A533B	6.84	544	2.06

in the appropriate region and doing a linear fit to the data. Figure 2.6.2 shows this process for determining the coercivity of the C5 steel. The magnetizaton at saturation is easily extracted from the virgin field curve, although the value at 368 kA/m (4600 Oe) is little changed from that seen here at 240 kA/m (3000 Oe). A summary of the data is given in Table 2.6.1. Note that the A steels are not included; further assessment of their appropriateness for this project led us to drop them from the sample set. Remanence data were also analyzed, but for these steels they add nothing that is not already seen in the coercivity. The curves were not analyzed for permeability values at this time. That analysis requires a fairly lengthy process of correcting the curves for the demagnetizing field of the sample. If later investigation indicates that it might be a valuable parameter, it will be extracted then.

2.6.8 Low Temperature VSM Experiments

The coercivity Hc and the saturation magnetization, $\mu_0 M_S$, were measured at room temperature and on cooling to liquid nitrogen temperature (76 K) on new samples of A533B taken from the base metal (sample 1-2) and from the weld (sample W1). The results are shown in Table 2.6.2. In all cases, the effect is essentially reversible. Based on these limited data, we concluded that we are not seeing a transition of any sort, but that the observed increase is an effect of reduced thermal energy which, at the higher temperature, hinders the alignment of moments, lowering M_s, and helps the motion of domain walls, lowering H_c. Complete proof would require an experiment using a larger number of temperature points. H_c data on longer samples from earlier measurements which were cut from different regions and prepared slightly differently from the above gave values of H_c = 6.84 (1-2) and H_c = 8.95 (W1).

Table 2.6.2. Values of the coercivity H_c and saturation magnetization M_s for the A533B steels and the nickel standard at room temperature (two readings) and at the temperature of liquid nitrogen. (The samples used were 2 mm dia. × 10 mm long.)

Parameter	T	1-2	W1	Ni std
H_c in A/m (Oe) (2-point method)	Room temp.	571 (7.18)	759 (9.54)	1990 (25.0)
	Liquid N_2	602 (7.56)	844 (10.60)	2316 (29.1)
	Room temp.	571 (7.18)	761 (9.56)	1997 (25.1)
M_s (mV) (not calibrated)	Room temp.	59.2	59.2	18.5
	Liquid N_2	61.5	61.7	19.5
	Room temp.	59.2	57.9	18.4

2.6.9 Results and Conclusions

Preliminary analysis of the data for the C- series steel indicates a dependence of coercivity on sample treatment, but no dependence of the saturation magnetization. This latter observation is to be expected given that the composition of the steel is not changed dramatically by the heat treatments. The coercivity variation does not track with the hardness, which is taken as the measure of embrittlement for these experiments. Again, this is not surprising given that a number of changes in the microstructure, defect content, and arrangement are occuring in this material. There is still reason to believe that, when applied to the actual problem where the confounding variables are minimized, the magnetic measurements may well provide excellent diagnostics.

There are several clear directions for the future of these measurements: First, we need to evaluate a number of samples from a given lot of steel with more tight control on their preparation, especially the EDM operation and subsequent cleanup. Second, we need to investigate the possibility of measuring a sample of the irradiated steel in our laboratory. The samples are sufficiently small that this may be possible. If even smaller samples were necessary, our SQUID magnetometer systems could measure milligram quantities, albeit with a bit more difficulty than that encountered with the larger samples in the VSM. The major problem will be in getting the appropriate samples prepared—almost certainly a hot-cell EDM system would be needed.

2.6.10 Other Methods

B-H Looper. A number of techniques that we think may be used on samples of the actual steel (unirradiated, but with cladding in place) make use of a large transformer core device that could be called a B-H looper. We have built a first prototype of the device and made preliminary dc tests (ac and dc are possible) with multiple field detector locations and have demonstrated its ability to see a signal from the steel through the cladding. This is a long way from a usable instrument, but we are encouraged by the results to date.

Bitter Techniques. Early in the project, we attempted some very preliminary measurements on two early A710 samples (not the C samples) using the Bitter technique to look for domain structure. We had no luck bringing the domains out either with a very fine oxide powder or with a more conventional iron powder suspension. We probably need a smoother surface prepared by electropolishing or chemical polishing and measured relatively soon after preparation to avoid surface oxidation. This was only a secondary experiment and, thus, has not been pursued further.

AFM/MFM Studies. Early in our thinking about the problem, we considered how to use the atomic force microscopy (AFM), and maybe magnetic force microscopy (MFM), capability of our scanning probe microscope to image precipitates with sizes in the 10 nm range. There is reason to believe that it can be done *if we can find the things* and if the sample surface can be prepared such that they remain there and don't get ripped out or flattened by the surface preparation. No experiments were tried, but it remains a possible technique to be evaluated in more detail.

Ion Implantation Studies. We have been involved in recent years in a project studying nitrogen-ion-implanted stainless steel surfaces implanted with N ions. We can also implant Cu into steel, and it occurred to us that this might make a reasonable model material for the irradiated steel. Initially, two samples of Fe were implanted with Cu ions. These were very heavily implanted (40% Cu), but in a very thin layer (~20 nm). It is possible that this may be a way to make a (very small) sample with the right amount of copper. Certainly one can heat these samples to encourage copper migration from the surface layer. New samples with better surface preparation and 1 to 10% implanted copper have been prepared and preliminary magnetic force microscope and atomic force microscope images have been made. As usual, the data are confusing, but sufficiently interesting to consider further study under NIST funding.

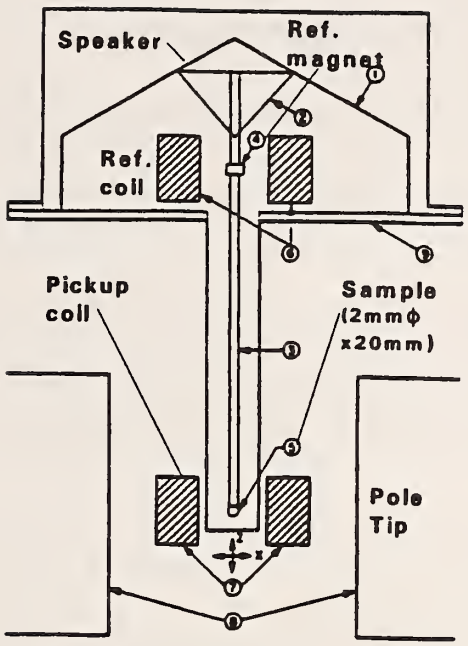

Fig. 2.6.1 Schematic diagram of a vibrating sample magnetometer (VSM).

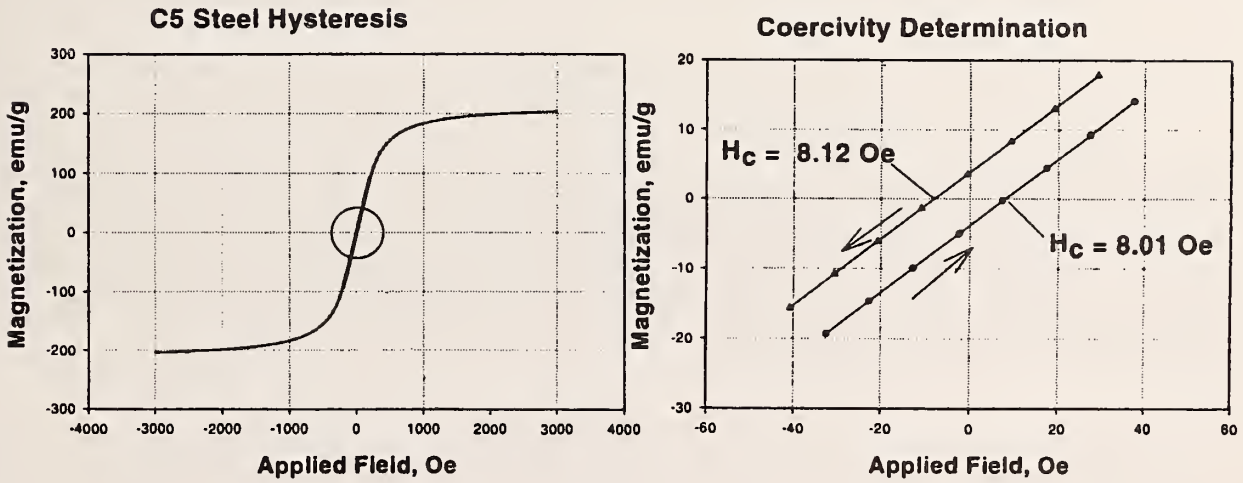

Fig. 2.6.2 (Left) Example of the hysteresis curve observed with the VSM for alloy A710 in the peak-aged condition. (Right) Magnified hysteresis curve near H = B = 0 for determination of Hc.

2.7 MICROMAGNETIC TECHNIQUES — *Brian Igarashi*

2.7.1. Development of a Noncontacting Measurement of Magnetostriction

The objectives of the micromagnetics experiments are twofold: (1) demonstrating that magnetostriction (the change of length of a ferromagnetic material that accompanies magnetization) and the transverse incremental permeability are sensitive to the formation of Cu-rich precipitates (CRPs) in carbon steel and (2) devising a noncontacting technique for measuring magnetostriction. Such a noncontacting technique would be needed in the field, since the portion of RPV carbon steel that is the target of inspection lies underneath stainless steel cladding. Results of investigations into the first objective are discussed in individual sections below, but the way by which the second objective is fulfilled may be described briefly as follows.

Magnetostriction of a steel sample is ascertained by measuring the amplitude of ultrasonic waves generated by magnetostriction. The noncontacting aspect of the measurement is afforded by use of electromagnetic acoustic transducers (EMATs) to generate and detect ultrasound. Thompson [2.7.1–2.7.3] has shown that shear horizontal (SH) plate waves can be generated magnetostrictively with the arrangement shown in Figure 2.7.1. A static magnetic field H_0 establishes an axis of tension due to magnetostriction. (Compression is regarded here as a negative tension.) The ac current in the meander coil creates an oscillating field H_ω that adds perpendicularly to the static field and, in effect, rotates the axis of tension in the surface plane, thus, creating a shear strain.

According to Thompson, the amplitude of the SH wave obeys the relationship,

$$\Psi \propto \delta h \left| \frac{\partial \epsilon_{xy}}{\partial H_\omega} \right|, \tag{1}$$

where ϵ_{xy} is the magnetostrictive shear strain induced by H_0 and H_ω (the derivative is referred to as magnetostrictive strain coefficient), h is the magnitude of H_ω at the sample surface, δ is the skin depth , μ_t is the transverse incremental permeability, σ is the conductivity, and ω is the angular frequency. In near-saturation static fields, where the axis of magnetostrictive tension rotates nearly parallel with the net magnetic field,

$$\frac{\partial \epsilon_{xy}}{\partial H_\omega} = \frac{3}{2} \frac{\lambda}{H_0}, \tag{2}$$

where λ is the magnetostriction coefficient (the longitudinal strain due to H_0). At low H_0, this expression gives an overestimate of the derivative, but we [2.7.4] recently have shown that modelling of the wave amplitude is improved somewhat by using

$$\frac{\partial \varepsilon_{xy}}{\partial H_\omega} = \frac{3}{2}\frac{\lambda}{H_\omega}\frac{\left(\frac{B_0}{\mu_t H_\omega} - \frac{\mu_t H_\omega}{B_0}\right)}{\left(\frac{B_0}{\mu_t H_\omega} + \frac{\mu_t H_\omega}{B_0}\right)^2}. \qquad (3)$$

The range of validity of this expression extends to lower H_0 than eq (2), because the axis of magnetostrictive tension does not rotate parallel with the net magnetic field at low H_0. Substitution of eq (3) into eq (1) yields better predictions of variations of wave amplitude at low H_0, although relative values of the wave amplitude at low H_0 are overestimated.

Estimates of $|\lambda|$ are obtained by substituting measured wave amplitudes into the following expression derived from eqs (1) and (3):

$$|\lambda| \propto \Psi \sqrt{\mu_t}\,\frac{\left(\frac{B_0}{\mu_t H_\omega} + \frac{\mu_t H_\omega}{B_0}\right)^2}{\left|\frac{B_0}{\mu_t H_\omega} - \frac{\mu_t H_\omega}{B_0}\right|}. \qquad (4)$$

This expression is valid primarily at high H_0, and that relative values of the estimated $|\lambda|$ tend to be underestimated at low H_0.

We experimented with a variety of methods for measuring the amplitude of SH waves generated by EMATs (specifically, the fundamental SH_0 mode). In initial experiments, we attempted to infer the wave amplitude from the amplitude of standing waves set up between parallel sides of a sample. However, it was discovered that the EMAT excited unwanted standing waves that interfered with the one being monitored. Although this problem could be ameliorated by sticking clay to the sides of the sample to dampen out unwanted standing waves, measurements were judged to still contain an uncertain error. For this reason, this approach was abandoned in favor of a pulse-echo technique that directly measures the amplitude of the traveling wave generated by the EMAT.

One configuration of the pulse-echo measurement is depicted in Fig. 2.7.1 (Setup 1). A meander-coil EMAT is used to generate SH_0 waves of 4 mm wavelength. A gated amplifier issues pulses consisting of three cycles of sinusoids at 791 kHz, and the amplifier output is adjusted continuously to maintain a constant EMAT peak current of 5 A. The amplitude of a chosen echo is measured with a shear piezoelectric transducer that is pressed flush against one edge of the sample with its axis of displacement aligned parallel to the length of the sample.

Care was taken to avoid destructive interference between echoes, which would result in underestimating the amplitude of an isolated echo. This is a potential problem with the most closely spaced echoes, which originate from the two pulses simultaneously emitted in opposite directions by the meander coil. The problem is avoided by positioning the meander coil a quarter wavelength away from a sample edge; then the two pulses essentially combine to form a single pulse of approximately twice the duration of the input pulse to the meander coil, and no destructive interference occurs.

During all types of measurements, the samples were mounted between C-shaped pole pieces of an electromagnet (see Fig. 2.7.2). Samples were positioned carefully in the electromagnet in such a way as to minimize pulling on the ends of the sample due to magnetic attraction between the sample and the pole pieces. The amplitude of the SH_0 wave was monitored as the magnetic field is decreased from high levels.

In Setup 2 shown in Fig. 2.7.2, the piezoelectric transducer was replaced by a second EMAT. This setup was more suitable for measuring the wave amplitude at variable temperatures, since the repeatibility of measurements with a piezoelectric transducer suffers from temperature-induced shifts in the bond. The disadvantage of this setup is that it is more difficult to extract the magnetostriction from measurements of the wave amplitude, since the wave amplitude is a function of both the generation and reception efficiencies of the EMATs, which depend upon magnetostriction in different ways.

Measurements of the ultrasonic wave amplitude ψ were performed on 122 × 21 × 9 mm bars of A710 steel (samples CA, C5, and C7) and A533B (samples 1-2 and W-1). For each sample, all measurements were performed on a single surface that was wet-ground using a sequence of sandpapers ranging in roughness from between 60 and 800 grit. Subsequently, at least 30 to 40 μm of material was removed by chemically polishing the surface with an aqueous solution of oxalic acid and hydrogen peroxide. Between measurements, samples were stored under a roughing pump vacuum, and, after the samples were exposed to air for a few hours during the measurements, the chemical polishing of samples was repeated.

The magnetization, magnetostriction, and transverse incremental permeability were measured separately. The B-H curve of a sample was obtained by measuring the voltage induced across a solenoid wound around a sample. The transverse incremental permeability was measured through an eddy current technique suggested by Rose et al. [2.7.5]. These authors have shown that the transverse incremental permeability μ_t is proportional to the unique frequency f_0 that leaves the real inductance of a coil unaffected when the coil is brought close to a ferromagnetic material. In the present work, a flat, spiral, oval shaped coil was used, and f_0 was measured as a magnetic field was applied. (The frequency f_0 varied between ~10 kHz near saturation to ~250 kHz at low fields.) The coil was oriented in such a way as to measure the incremental permeability mostly along a direction perpendicular to the applied static field (that is, parallel to H_ω in Fig. 2.7.1). With this configuration, μ_t is expected to be B/H near saturation, and μ_t is

derived as a function of the applied field by scaling f_0 so that μ_t equals B/H at high fields (with values of B taken from the B-H curve and H expressed in units of A/m).

2.7.2 Measurement of A710 Steel

The purpose of tests on this material was to demonstrate that micromagnetic measurements are sensitive to the formation of fine CRPs that strengthen the steel. Results are summarized in Fig. 2.7.3. The transverse incremental permeability (Fig. 2.7.3(a)) and the SH_0 wave amplitudes (Fig. 2.7.3(b) and 2.7.3(c)) are different for the three samples. Differences among the transverse incremental permeabilities occur primarily at low H_0, while differences among the wave amplitudes extend to high fields. Figure 2.7.3(d) shows estimates of $|\lambda|$ obtained by substituting data from Figs 2.7.3(a) and 2.7.3(b) into eq (4), and, again, it is seen that the curves are different for all three samples. The differences shown in Fig. 2.7.3(d) agree qualitatively with results reported by other investigators [2.7.6]; for example, they observed that the maximum static magnetostriction of copper-alloyed (1 mass percent) ferritic steel (WB 36) reaches a peak value when fine CRPs form (similar to the case of sample C5).

Several aspects of these curves may be correlated with other measurements of the samples. For example, Fig. 2.7.4 shows that the maximum transverse incremental permeability correlates with the lattice strain determined from x-ray diffraction. Average values of the most valid estimates of $|\lambda|$ in Fig. 2.7.3(d) (those in the near-saturation regime, which lies above 25 kA/m in this case) also correlate with lattice strain. The same two quantities also correlate with hardness (see Fig. 2.7.5). Figure 2.7.6 shows that the H_0-values of the maxima in Fig. 2.7.3(d) correlate with the proportional limits of the samples.

The way that certain features of the magnetostriction and transverse incremental permeability change monotonically with lattice strain and hardness suggests that the changes are linked to the population of strengthening CRPs. These micromagnetic measurements are therefore sensitive to the formation of these precipitates, which points to the possibility of using either technique as an NDE tool for monitoring the evolution of CRP's in this particular steel.

2.7.3 Measurements on A533B Steel.

Micromagnetic measurements are performed on two specimens of this steel, one cut from the base metal (1-2) and the other from a weld region (W1). Results of room temperature measurements are shown in Figs. 2.7.7 and 2.7.8. The transverse incremental permeability curves of the two samples practically overlap (the uncertainty of data points is ±5%), and the SH_0 wave amplitudes largely agree with each other within estimated uncertainties. [It should be noted that, even though the receiver gain is increased for these measurements, much smaller wave amplitudes are recorded in these samples than in the A710 samples (see Fig. 2.7.3(b)).] This close agreement of measurements in the two samples is consistent with the small difference of lattice strains of these samples (ϵ(1-2) = 0.00073 ± 0.00001, ϵ(W1) = 0.00077 ± 0.00001, and $\Delta\epsilon/\epsilon$ = 5 ± 2%),

which reinforces the notion of micromagnetic quantities correlating with lattice strain, as suggested by measurements of the A710 samples.

These samples were also measured below room temperature in order to determine the temperature dependences of the micromagnetic quantities and to ascertain whether they may be used to predict the ductile-to-brittle transition temperature (DBTT) of this steel. The samples were cooled by placing them in spring-loaded contact with brass blocks carrying liquid nitrogen, and nitrogen gas was sprayed on the samples to help suppress build-up of frost.

While the B-H curves of both samples do not change significantly between −120 °C and room temperature, both the transverse incremental permeabilities (Figs. 2.7.9 and 10) and the SH_0 wave amplitudes (Fig. 2.7.11) of the samples do depend on temperature. The transverse incremental permeabilities change with temperature primarily at low H_0 (similar to effects of Cu precipitation discussed previously). The temperature dependences of the maximum values of the transverse incremental permeabilities are plotted in Fig. 2.7.12(b). The wave amplitude seems to be more sensitive to temperature; it displays a temperature dependence over a larger range of fields H_0. Features of the most reliable data, portions of the curves lying in the near-saturation regime (above ~25 kA/m), depend linearly upon temperature; for example, Fig. 2.7.12(c) shows that the wave amplitudes at 80 kA/m decrease linearly with increasing temperature.

The temperature dependences of the two samples are different. Hence, even though at room temperature the samples share similar transverse incremental permeabilities and wave amplitudes, one may measure these quantities at low temperatures to distinguish the samples. For example, Fig. 2.7.8 shows that the wave amplitudes at −128 °C are distinct. The temperature dependences of the impact toughness of the two samples also are different, and the toughness changes with temperature the most in sample 1-2, similar to the transverse incremental permeability and wave amplitude (see Figs. 2.7.12(a) through (c)). The possibility arises, then, that the temperature dependences of all three quantities are affected by common physical properties. However, the fact that the micromagnetic curves do not reproduce the sigmoidal shape of the impact toughness curve (that is, do not show evidence of a transition at the DBTT) suggests that the relationship between the micromagnetic quantities and impact toughness is tenuous. Micromagnetic measurements cannot be used to determine directly the DBTT.

2.7.4 Conclusions

Micromagnetic measurements may be used to monitor the evolution of CRPs in A710 steel. Certain features of the magnetostriction and transverse incremental permeability are shown to correlate linearly with the lattice strain, hardness, and proportional limit. The magnetostriction is measured through use of EMAT-generated waves, a noncontacting technique which would be necessary for determining zones of embrittlement in pressure vessels. Investigations in A533B steel reveal that, although it is possible that the temperature dependences of micromagnetic quantities and impact toughness depend upon common physical properties, micromagnetic techniques cannot be used to determine directly the DBT temperature.

2.7.5 References

2.7.1 Thompson, R.B., New configurations for the electromagnetic generation of SH waves in ferromagnetic materials, in: 1978 Ultrasonics Symposium Proceedings, Cat. No. 78CH1344-1SU, J. deKlerk and B.R. McAvoy, eds., IEEE Press, New York (1978).

2.7.2 Thompson, R.B., Generation of horizontally polarized shear waves in ferromagnetic materials using magnetostrictively coupled meander-coil electromagnetic transducers, Appl. Phys. Lett. vol. 34, pp. 175-177, Jan. 1979.

2.7.3 Thompson, R.B., Physical principles of measurements with EMAT transducers, in: Ultrasonic Measurement Methods, Vol. 19 of Physical Acoustics, R.N. Thurston and A.D. Pierce, eds., Academic Press, Boston (1990), ch. 4, pp. 157-200.

2.7.4 Igarashi, B., Alers, G.A., Purtscher, P.T., An ultrasonic measurement of magnetostriction, in: 1997 Ultrasonics Symposium Proceedings, IEEE Press, New York (in press).

2.7.5 Rose, J.H., Tai, C.-C., Moulder, J.C., Scaling relation for the inductance of a coil on a ferromagnetic half-space, J. Appl. Phys., in press.

2.7.6 Altpeter, I., Becking, R., Jaschan, A., Kern, R., Lang, M., Rösner, H., Proof of Cu Precipitates by Means of Micromagnetic Test Procedures, IZFP (Frauhofer-Institut für zerstörungsfreie Prüfverfahren) Report No. 970137-TW, 1997 (unpublished).

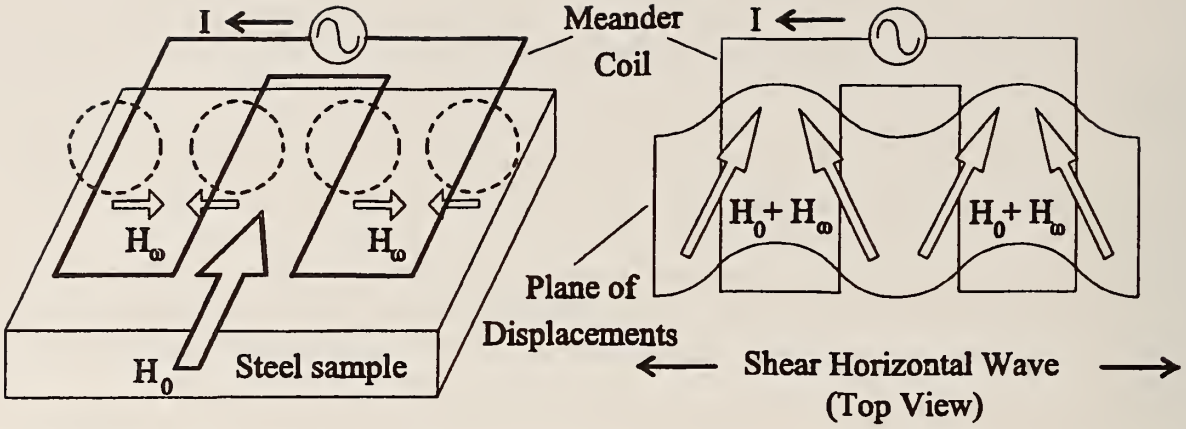

Fig. 2.7.1 Setup for magnetostrictively generating SH ultrasonic waves with an EMAT. The meander coil carries ac current I, and H_0 is applied by an external magnet. The resultant elastic displacements are parallel to the sample surface.

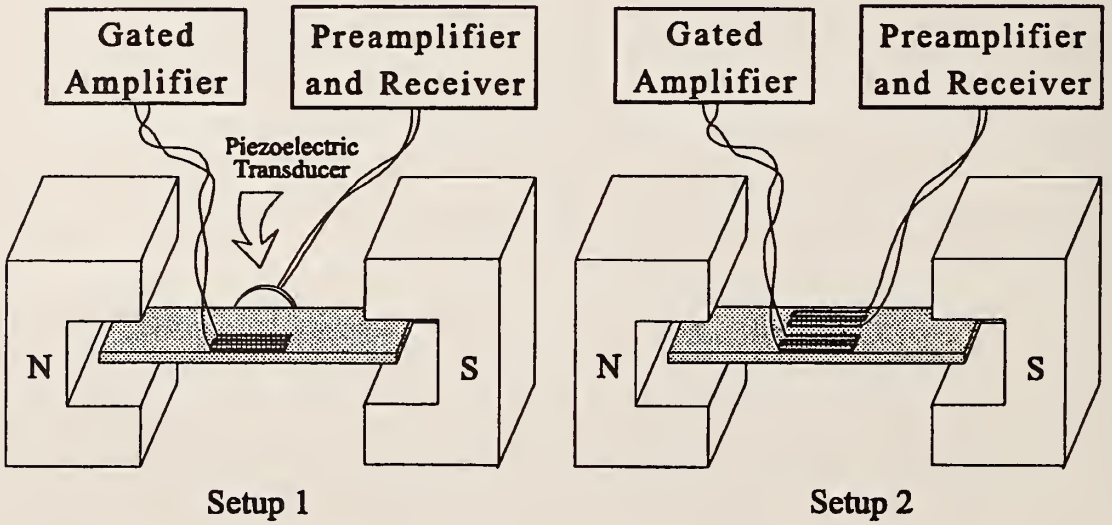

Fig. 2.7.2 Experimental setups for measuring the amplitude of SH_0 ultrasonic waves.

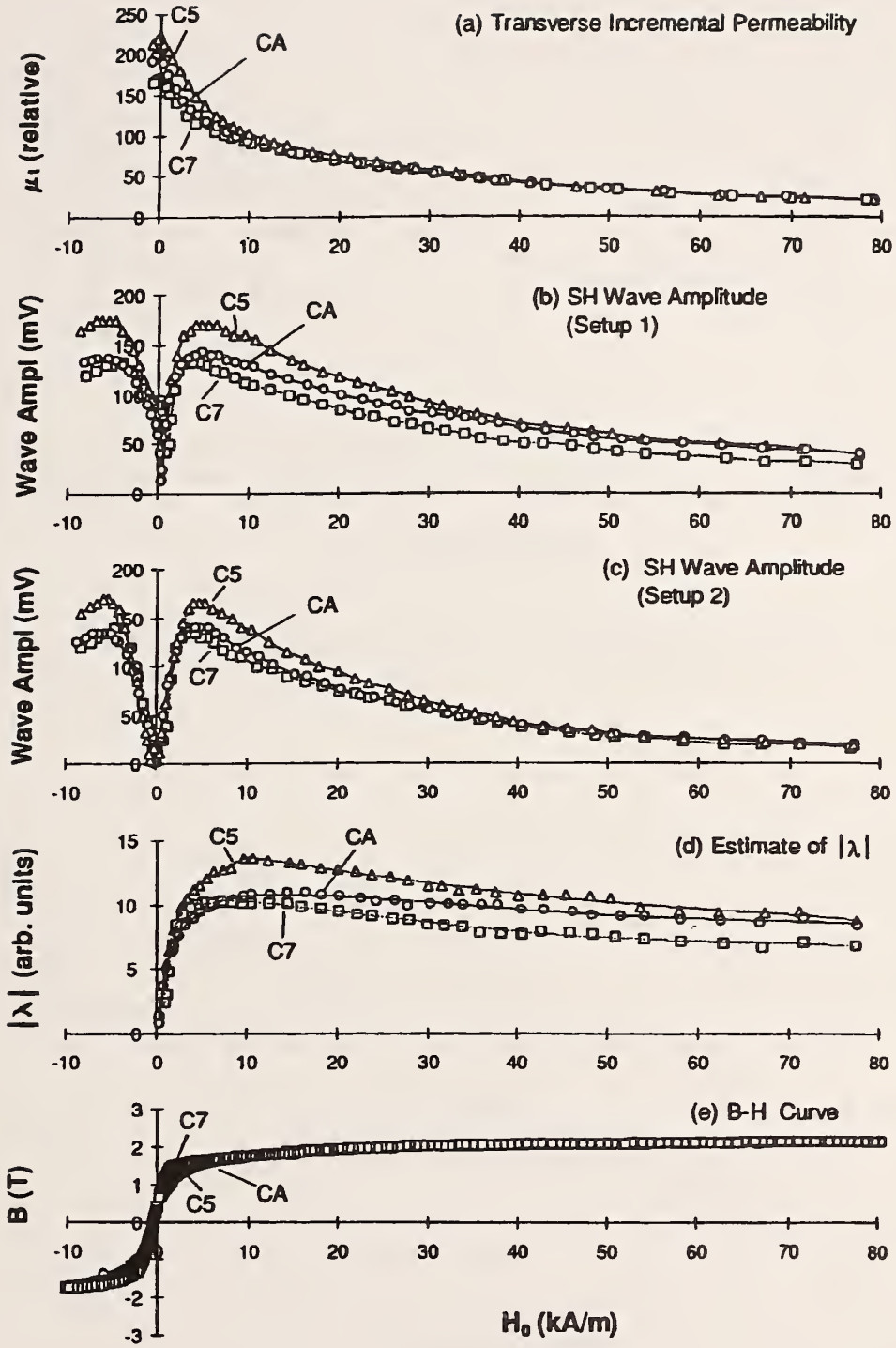

Fig. 2.7.3 (a) Transverse incremental permeabilities, (b) SH_0 wave amplitudes measured in Setup 1 of Fig. 2.7.2, (c) SH_0 wave amplitudes measured in Setup 2 of Fig. 2.7.2, (d) estimates of $|\lambda|$ from eq (4) and (e) B-H curves obtained in the CA(0), C5(△), and C7(□) A710 samples.

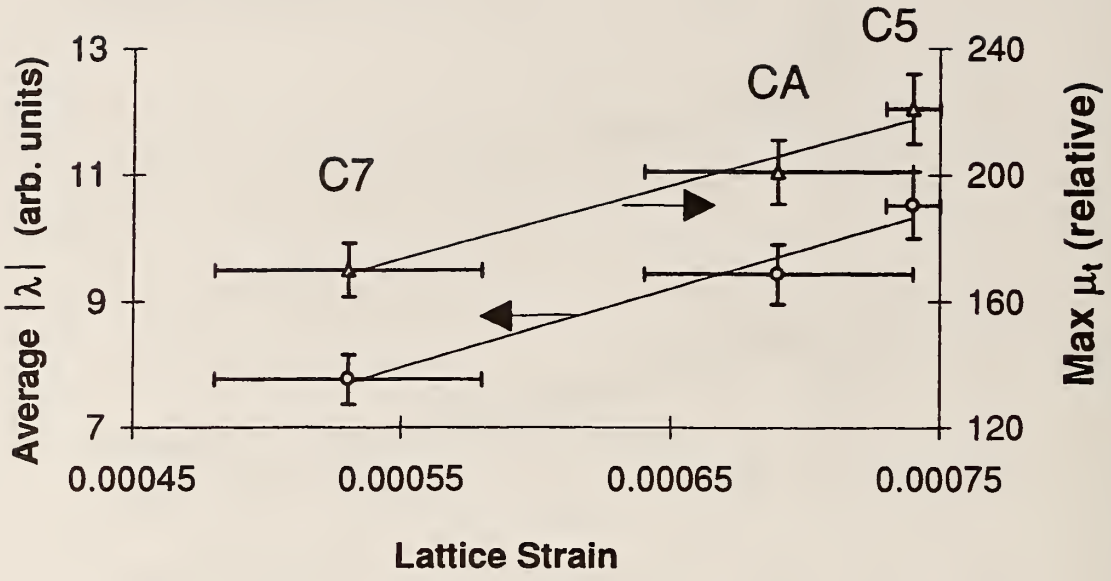

Fig. 2.7.4 Estimated $|\lambda|$ averaged over high $H_0(0)$ and maximum transverse incremental permeability (Δ) versus lattice strain.

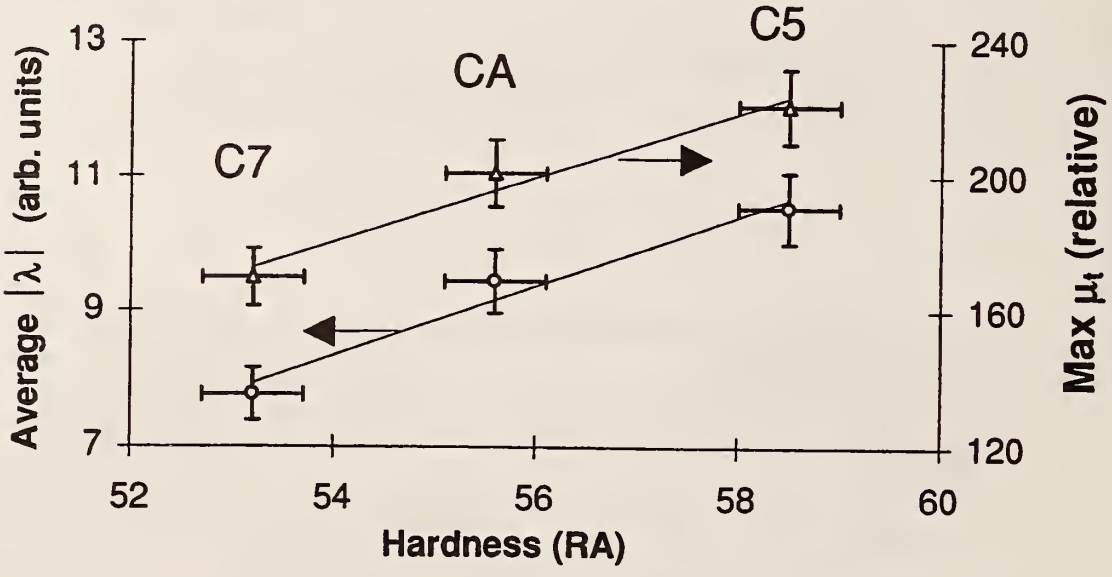

Fig. 2.7.5 Estimated $|\lambda|$ averaged over high $H_0(0)$ and maximum transverse incremental permeability (Δ) versus hardness.

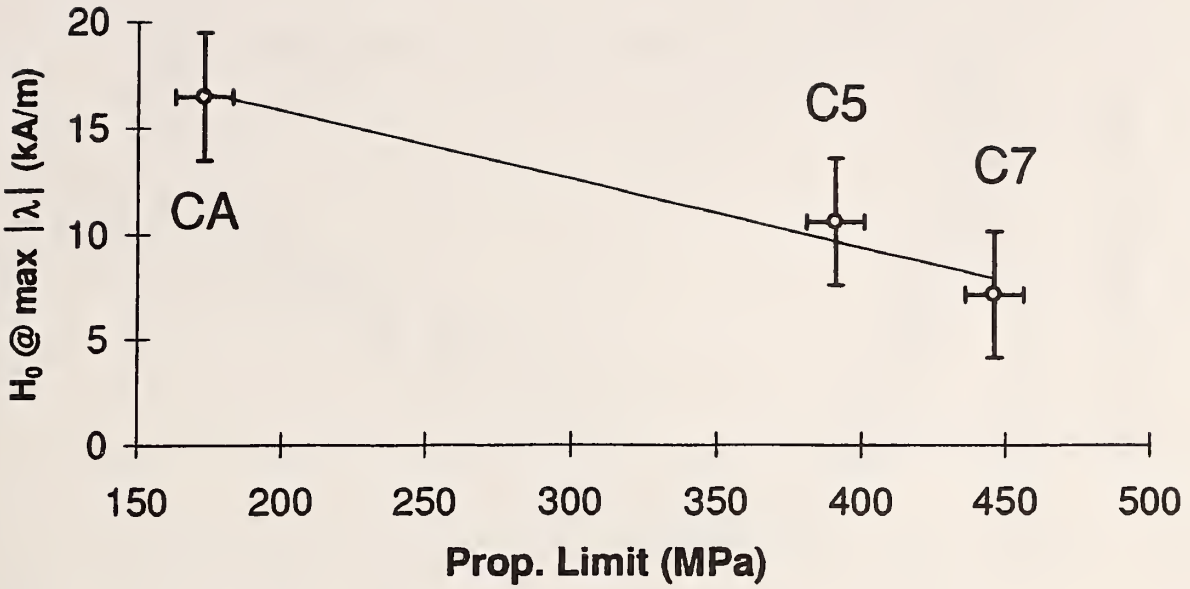

Fig. 2.7.6 H_0 at maximum $|\lambda|$ in Fig. 2.7.3(d) - (0) versus proportional limit.

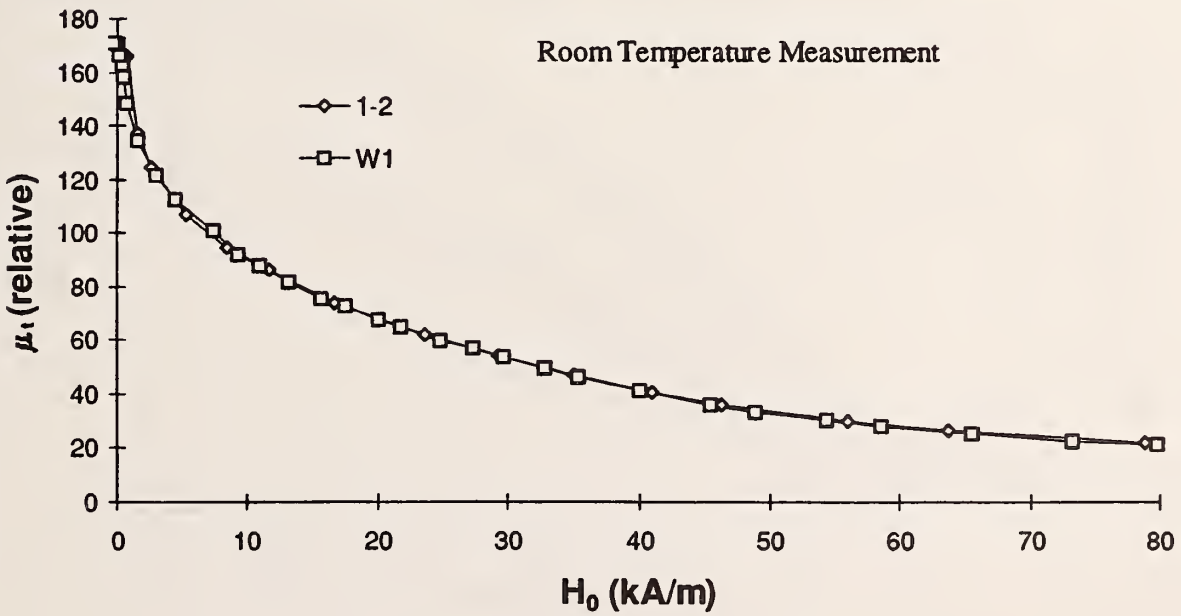

Fig. 2.7.7 Comparison of tranverse incremental permeabilities of A533B samples 1-2 (◇) and W1(□) at room temperature.

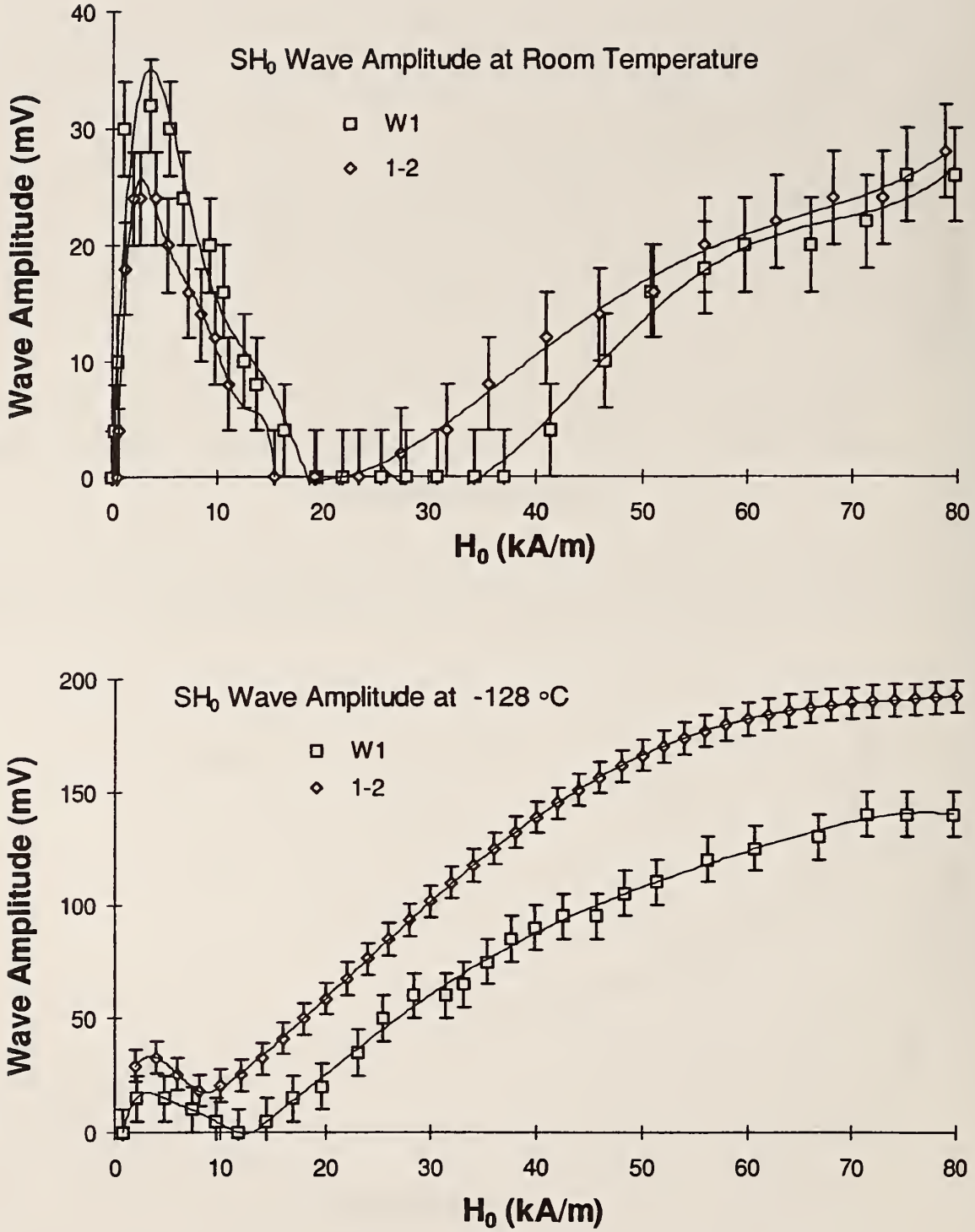

Fig. 2.7.8 Comparisons of SH_0 wave amplitudes measured in A533B samples 1-2 (◇) and W1 (□) at room temperature (top) and at −128 °C (bottom).

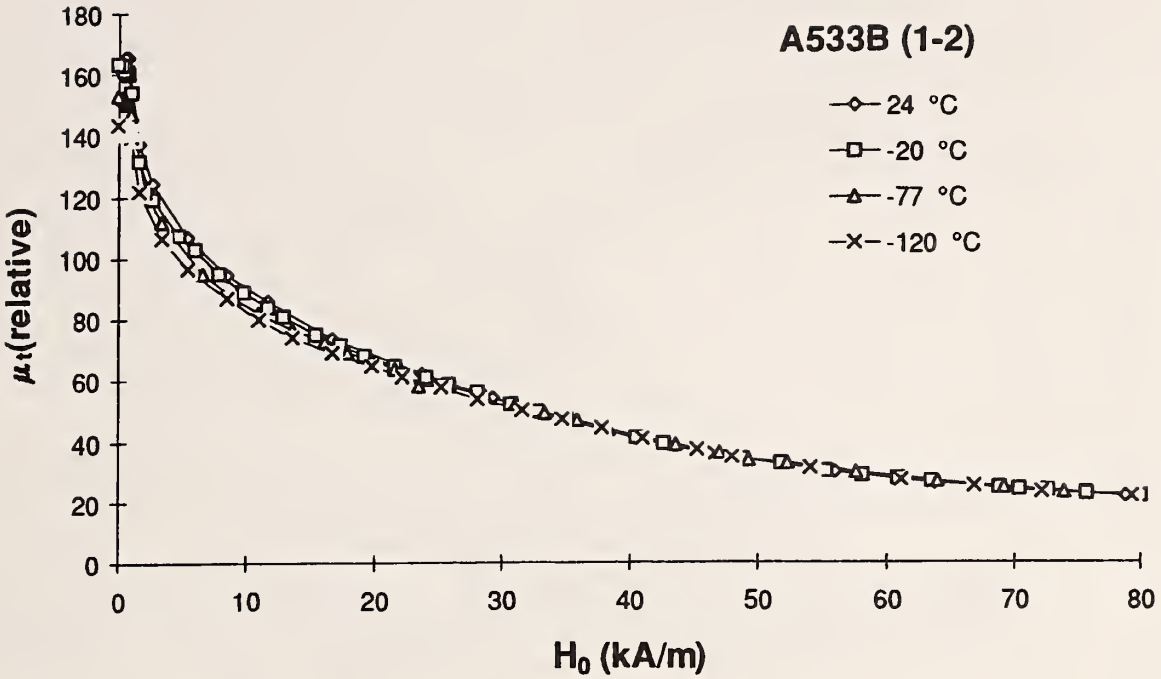

Fig. 2.7.9 Transverse incremental permeability of sample 1-2 versus H_0 at 120 °C (x), −77 °C (△), −20 °C (□), and 24 °C (◇).

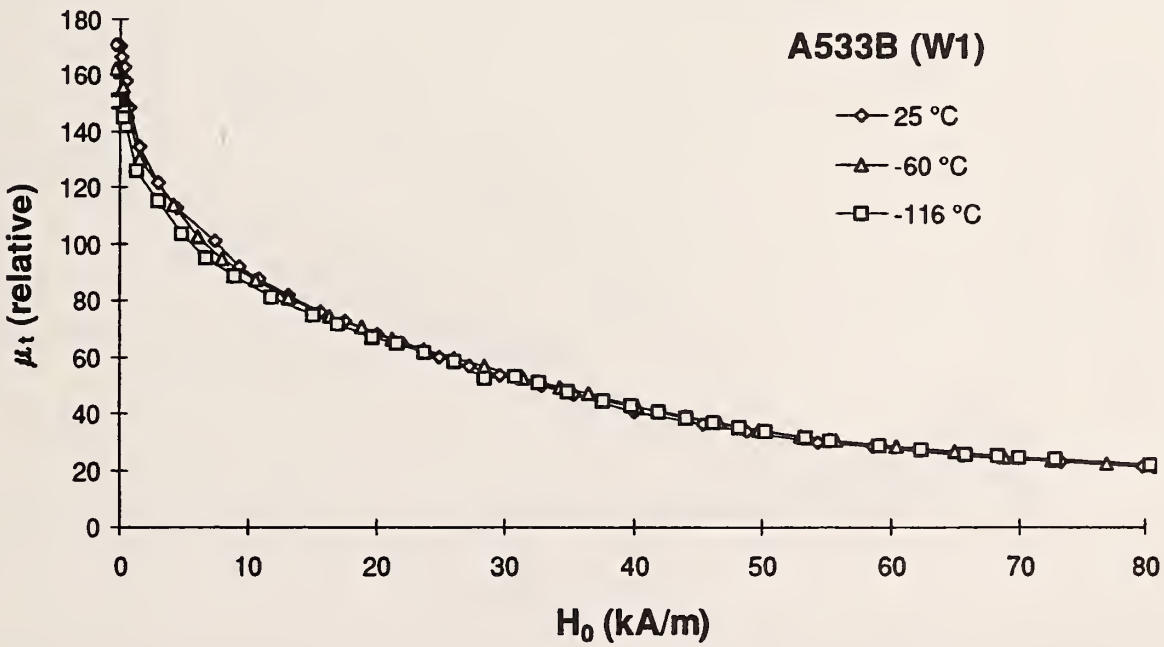

Fig. 2.7.10 Transverse incremental permeability of sample W1 versus H_0 at −116 °C (□), −60 °C (△), and 25 °C (◇).

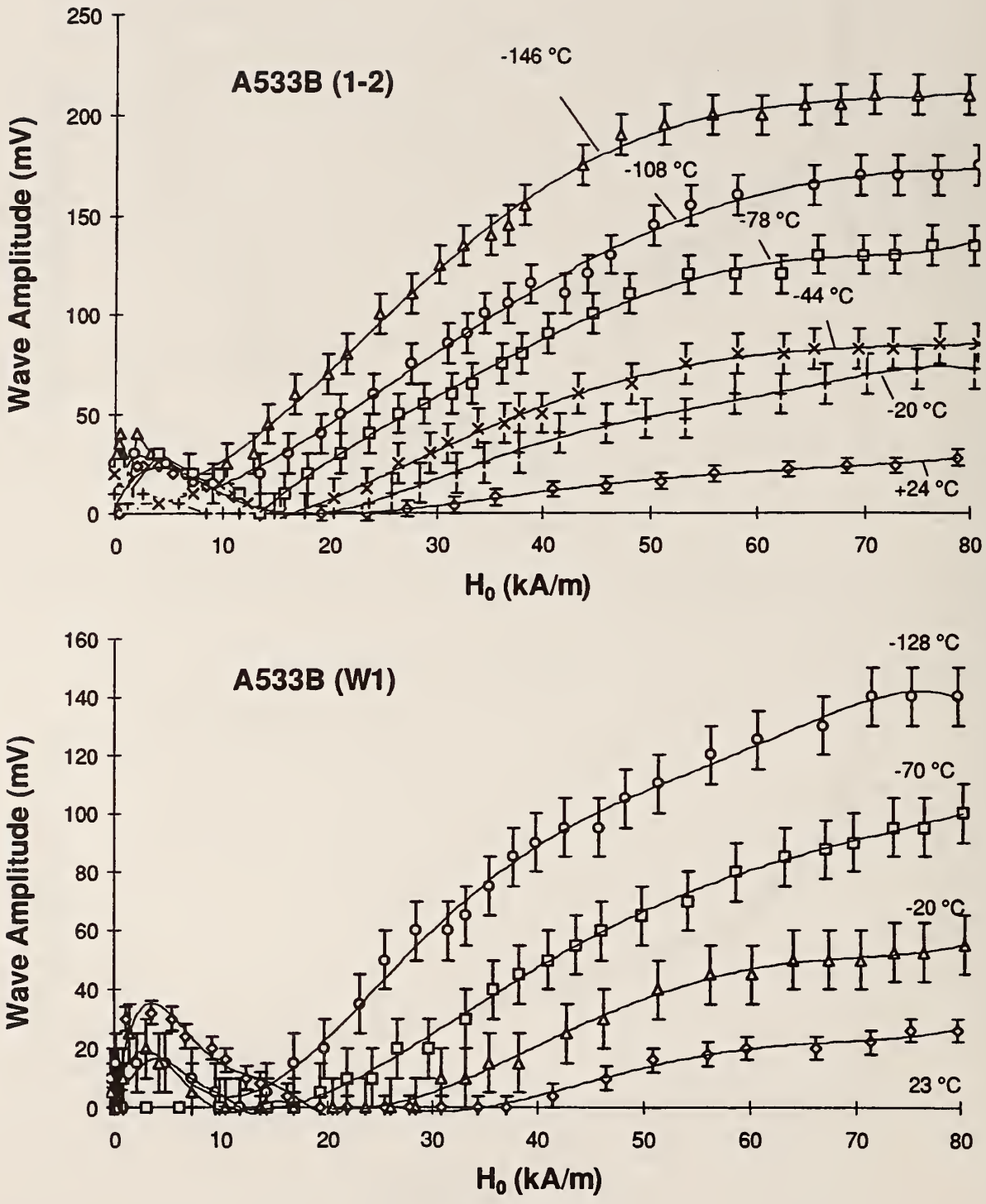

Fig. 2.7.11 SH_0 wave amplitude measured at various temperatures in sample 1-2 (top) and sample W1 (bottom) using Setup 2 in Fig. 2.7.2.

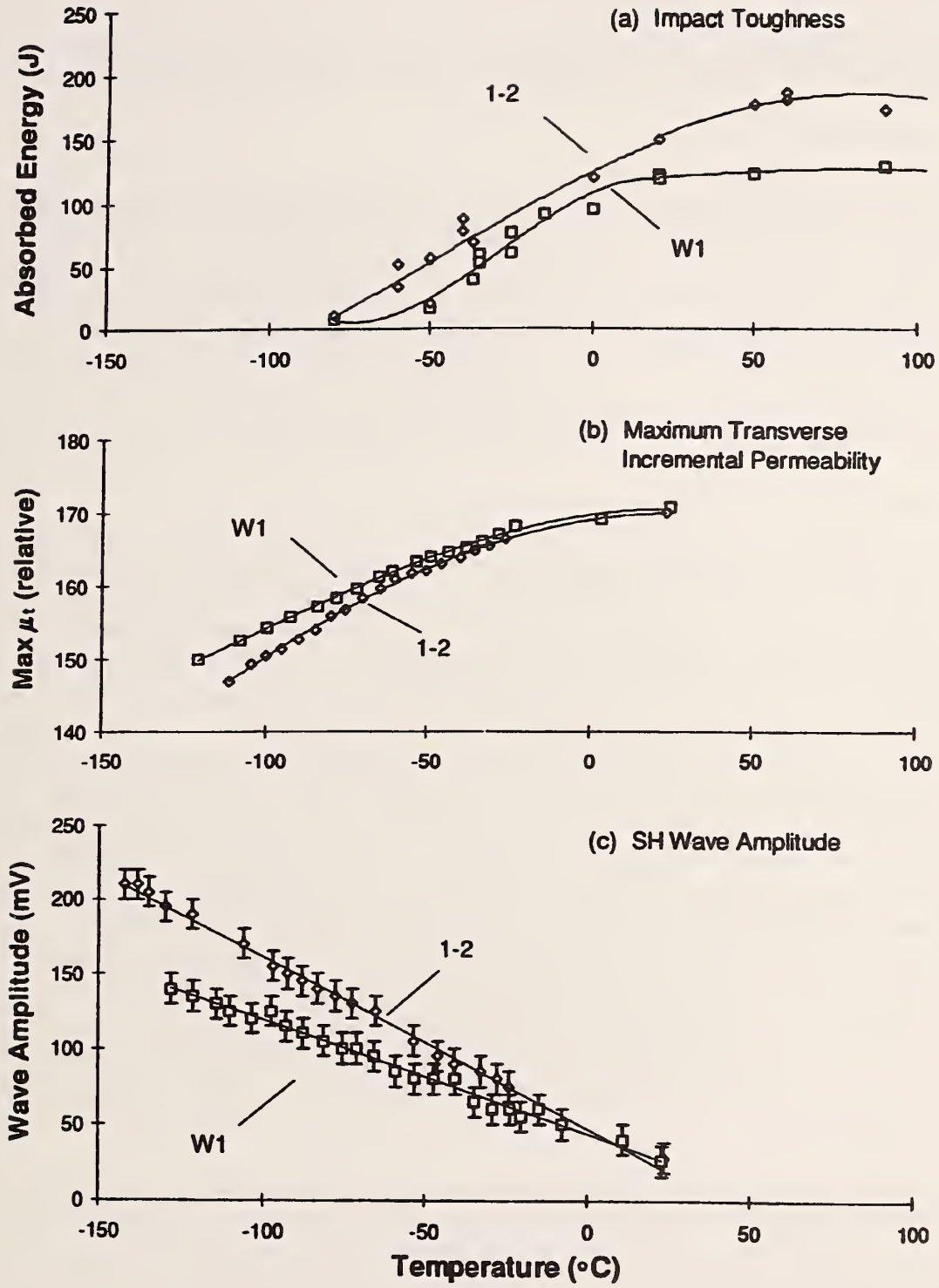

Fig. 2.7.12 Comparisons of temperature dependences of impact toughnesses (a), maximum transverse incremental permeabilities (b), and SH_0 wave amplitudes at 80 kA/m (c) measured in A533B samples 1-2 (◇) and W1 (□).

2.8 DISLOCATION MOBILITY UNDER A STATIC STRESS—Ward Johnson

2.8.1 Introduction

Ultrasonic measurements can be highly sensitive to the density, symmetry, and pinning of dislocations in crystals because the nonelastic response of dislocations to an acoustic wave causes damping and slowing of the wave. This phenomenon was explored in this project as a potential tool for nondestructively evaluating the mechanical properties of irradiated steel, especially the ductile-to-brittle transition temperature. The principal experimental approach employed was to use resonant ultrasonics to sense the degree to which dislocations break away from pinning points when surrogate materials were subjected to loads in a tensile testing machine. This type of measurement provides information about the mobility of dislocations.

2.8.2 Experimental Apparatus

A unique system was implemented for measuring resonant ultrasonic properties of specimens undergoing static or dynamic loading in a tensile testing machine. Figure 2.8.1 shows the configuration of the specimen and the grips that are mounted in the testing machine. Elecromagnets around the machine grips provide a static magnetic field along the specimen axis. Liquid nitrogen cooling and resistive heating of the grips provide temperature control from −100 °C to +70 °C. Highly accurate damping and velocity measurements are achieved with a cylindrical "trapped-mode" geometry that has resonant vibrational modes localized in a central portion of the specimen and, thus, has insignificant energy losses through the testing machine grips [2.8.1]. This geometry is shown in Fig. 2.8.2. The length of the central trapping region l is 51.7 mm for A710 (C5 and C7) specimens and 57.5 mm in the A533B (1-1, 1-2, and W-1) specimens. The total length L is 157 mm for A710 and 166 mm for A533B. The losses of energy through transducer coupling are essentially eliminated by employing noncontacting electromagnetic-acoustic transducers [2.8.2]. The sample is driven into resonant vibration by a long tone burst, and the frequency and amplitude of vibrations are measured during the subsequent ring-down. A detailed description of this technique of signal analysis is presented elsewhere [2.8.3]. Because of the high accuracy and the frequencies employed (typically, 0.8 to 3 MHz), this system is very sensitivity to the anelastic properties of dislocations and associated microstructural changes.

Radial and flexural resonant modes show similar changes in damping in response to static loading, but have different values for the equilibrium background damping. In this report, the mode types and frequencies of the measurements will be noted only in the figure captions.

The field provided by the electromagnets is employed in acoustic transduction. It also reduces damping associated with magnetoelastic responses within the material, making the measurements more reproducible and sensitive to dislocation effects. Since dislocations were the principle focus of this part of the feasibility project, results relating to magnetic damping are not

presented here. All of the measurements in this report were performed with the magnetic field in the range 28 to 32 kA/m (350 to 400 Oe).

2.8.3 Results

a. Before plastic deformation. Figure 2.8.3 shows the damping at several ultrasonic frequencies in three A533B specimens prior to loading. As described elsewhere, the 1-1 and 1-2 specimens were taken from different sections of base metal, and the W-1 specimen was taken from weld metal. The damping is expressed as the dimensionless logarithmic decrement δ, which is the reciprocal of the number of cycles for the free-decay amplitude of resonant vibrations to drop to 1/e of its initial value. The damping in all three specimens increases monotonically with frequency. This is consistent with the frequency dependence expected for dislocation damping in impure materials at these frequencies [2.8.4]. The data suggest that the density of dislocations that move in response to acoustic oscillations is lowest in 1-1 and highest in W-1.

A correlation between the ultrasonic results and Charpy results is pursued in Fig. 2.8.4 by taking the slopes of δ versus frequency for each specimen, obtained from the linear regressions shown in Fig. 2.8.3, and plotting these versus the temperature at which the Charpy impact energy drops to one half that of the upper plateau. The fact that 1-1 becomes brittle at higher temperatures than 1-2 and W-1 is consistent with the lower mobile dislocation density of 1-1 suggested by the ultrasonic damping measurements.

As discussed in section 2.8.4, accurate absolute measurements of damping in steel would be very difficult, if not impossible, on an actual pressure vessel. Therefore, in further pursuit of a practical nondestructive ultrasonic technique, a series of tests were developed to determine the relative changes in damping that occurs when specimens are subjected to tensile loading. Ultrasonic damping and velocity were measured as the load was (1) stepped rapidly from near zero to a significant fraction of yield, (2) held at the higher load for periods ranging from 10 to 600 s, and (3) reduced back to the original low load and held there. If dislocations are broken away from pinning points by the application of a load, one expects the damping to increase immediately but to recover with time as thermally activated repinning takes place. This effect is observed in materials that have been previously plastically deformed (see below). However, no effects of this type were observed in undeformed A533B (1-1, 1-2, and W-1) or A710 (C5) at temperatures ranging from −80 to 70 °C.

b. During plastic deformation. Ultrasonic measurements of two specimens of A710 steel, C5 and C7, were performed as the load was increased through yield. The loads were increased in discrete steps, and, at each load, δ was measured as a function of time. Figure 2.8.5 shows δ at two times following the step to each value of the load. In C5 (Fig. 2.8.5(a)), δ was relatively constant as the load was increased until reaching approximately 450 MPa, where time dependent changes occurred after the load step. Increases in δ after the steps were greater at higher loads, but always approached a constant with extended time at a given load. The changes in δ are interpreted as being the result of the depinning of dislocations and the increase in dislocation

densities that accompany plastic deformation. Similar effects have been reported by numerous researchers for a variety of metals and nonmetals. The continuous nature of the changes shown for C5, and the loads where they occur, are similar to the plastic strain shown in the conventional stress-strain curve obtained for this continuously yielding material. (See data presented in Fig. 2.2.1.) Measurements of the diameter of C5 before and after this test showed that a plastic strain of 0.15% had been introduced. Sample C7, which was found to yield discontinously in the conventional stress-strain test, had a relatively abrupt increase in δ near 495 MPa (Fig. 2.8.5(b)). This load is somewhat higher than the 471 MPa yield stress found in the conventional tensile test, probably because the ultrasonic test was performed much more slowly. Unlike C5, changes in δ proceeded more rapidly as the load was held at the highest load, consistent with discontinous yielding.

c. After plastic deformation. In plastically deformed A533B and A710, reproducible changes in δ are observed with loads well below those where macroscopic deformation had occurred in previous tests. Figure 2.8.6 shows measurements on a specimen of material 1-1 before and after 0.39% plastic prestrain. For the prestrained material, the load was initially held near 6 MPa for 1000 s, then increased in 0.5 s to 163 MPa (35% of the yield stress, as determined from the stress-strain test), held at that load for 100 s (during which time no ultrasonic measurements were performed), and, then, decreased back to 6 MPa. The 100 s loading induced an increase in δ followed by a slow recovery to the original value. A similar loading of material with no plastic prestrain induced no load-induced changes in δ even though the load was much higher (444 MPa). The load-induced changes in the deformed material are interpreted as being a result of breakaway and, perhaps, multiplication of dislocations followed, after release of the load, by recovery involving thermally activated movement of dislocations and/or point defects. This effect is found to be independent of the ultrasonic frequency. The solid line in Fig. 2.8.6 is a fit to the form $\delta = \delta_{eq} + [A\text{-}B\ln(1 + t/\tau)]^2$, which accurately matches changes in δ that accompany high-temperature isothermal recovery of cold-worked aluminum [2.8.5]. δ_{eq} is the equilibrium decrement at 6 MPa before the 163 MPa load. The success of this function in fitting the data of Fig. 2.8.6 suggests a mechanism similar to that of high-temperature recovery, involving dislocation annihilation followed by movement into a lower-energy configuration.

The magnitude of load-induced changes in δ increases with the magnitude of the load, as one would expect from dislocation breakaway. Figure 2.8.7 shows this dependence in a specimen of C5 that was previously deformed 0.15%. The response to a load also depends strongly on temperature. Measurements were performed on 0.15%-deformed C5 at several temperatures from −90 °C to +27 °C before and after loading at 420 MPa for 10 s. Figure 2.8.8 presents these measurements with the equilibrium δ_{eq} subtracted. At the higher temperatures, the initial change in δ is higher and the recovery is most rapid. This behavior is consistent with a mechanism involving thermally assisted unpinning of dislocations. That is, at the higher temperatures, dislocations are more rapidly unpinned during the period at 420 MPa, and, after the loading, thermally activated recovery proceeds more rapidly.

Since fracture behavior is also determined by the kinetics of dislocation unpinning, one may expect a close correlation between such ultrasonic results and the ductile-to-brittle transition.

2.8.4 Conclusions

The results presented here indicate that ultrasonic damping may provide information about mechanical properties by sensing the anelastic behavior of dislocations in equilibrium and under static loading. The equilibrium δ of undeformed A553B shows a correlation with the ductile-to-brittle transition in the three specimens studied (Fig. 2.8.4), and the sign of the correlation is consistent with that expected for dislocation effects. Increases in δ during plastic deformation provide information about yielding similar to that of a stress-strain curve. In plastically deformed material, the recoverable temperature-dependent ultrasonic response to loading is, apparently, sensitive to the kinetics of dislocation unpinning and, thus, may be closely related to the ductile-to-brittle transition.

From a practical perspective, however, the results are less than encouraging. Although interesting from the perspective of materials characterization, the techniques employed during and after deformation are useless for nondestructive evaluation because they involve modification of the material. The measurement of equilibrium δ before deformation is nondestructive. However, the values obtained for the equilibrium δ (Fig. 2.8.3) are so low that they are probably impossible to measure in the field. Because of the extensive complicated geometry of a pressure vessel and its structural supports, a high-resolution resonance method can not be employed. On the other hand, conventional pulse-echo methods suffer from diffraction losses that, even in plates with polished parallel surfaces, typically result in values of δ two orders of magnitude larger than the intrinsic δ measured here. Considering that the surfaces of pressure vessels (especially the stainless cladding) are highly irregular, scattering losses would be even more severe and small changes in intrinsic damping would be undetectable. Perhaps, other more exotic approaches to measuring damping would be useful to pursue. However, at present, there is no known technique that can measure damping comparable to that shown in Fig. 2.8.3 on an extensive irregular object such as a reactor pressure vessel.

2.8.5 References

2.8.1 Johnson, Ward; Auld, B.A. and Segal, E., Trapped torsional modes in solid cylinders, J. Acoust. Soc. Am., Vol. 100, p. 285 (1996).

2.8.2 Johnson, Ward; Alers, George, Force measurement using vibrational spectroscopy, Review of Scientific Instruments, Vol. 68, p. 102 (1997).

2.8.3 Johnson, Ward; Ultrasonic resonance of metallic spheres at elevated temperatures, J. Phys. IV (France), supplement to J. Phys. III (France), Vol. 6, p. C8-849 (1996).

2.8.4 Granato, A.V.; Lücke, K.; Physical Acoustics, Vol. IVA, edited by W. P. Mason (Academic, New York, 1966), p. 225.

2.8.5 Johnson, Ward; Ultrasonic damping in pure aluminum at elevated temperatures, J. Appl. Phys., to be published (March, 1998).

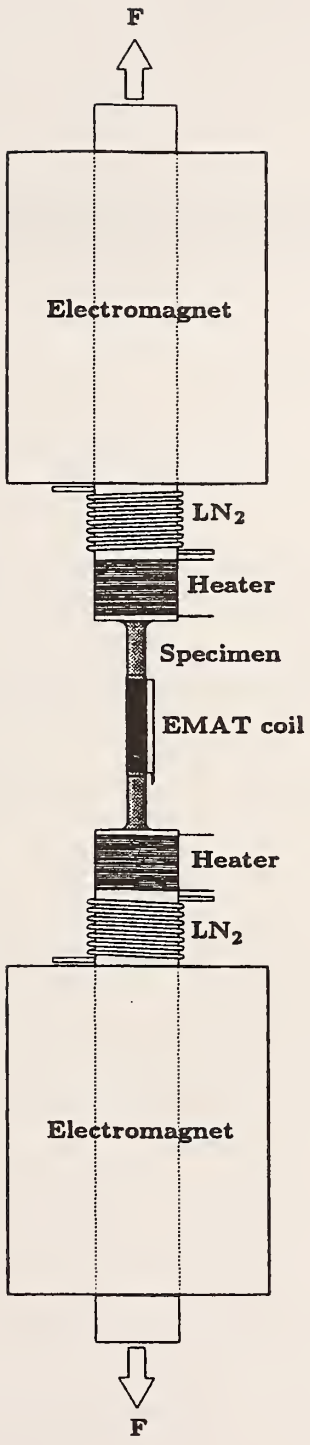

2.8.1 Configuration of the specimen and grips mounted in a tensile testing machine. Each of the grips is encircled by a heater, a liquid nitrogen cooling coil, and an electromagnet.

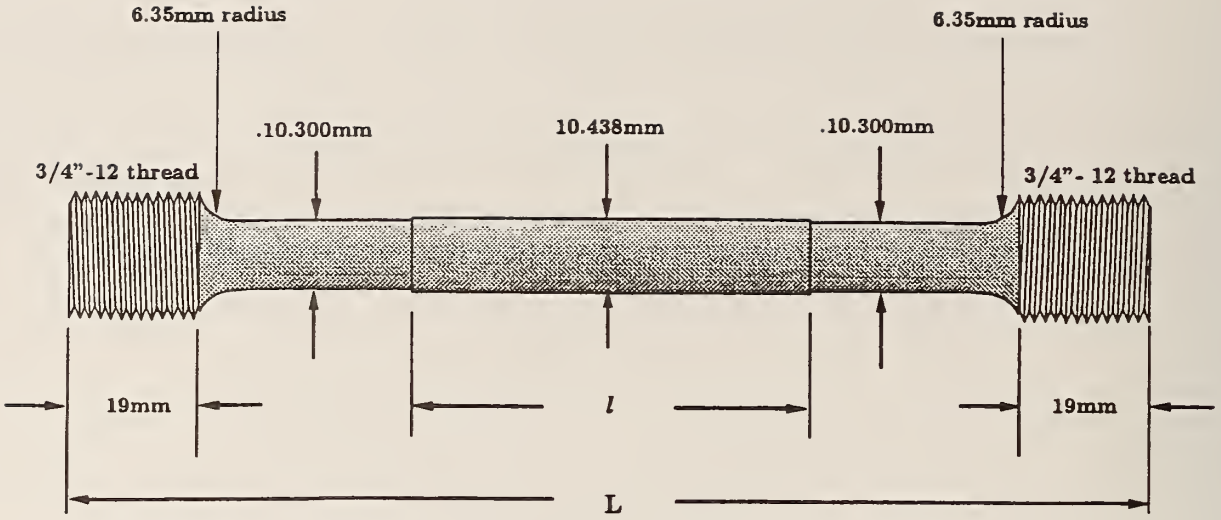

2.8.2 Geometry of a cylindrical ultrasonic resonant trapped-mode specimen.

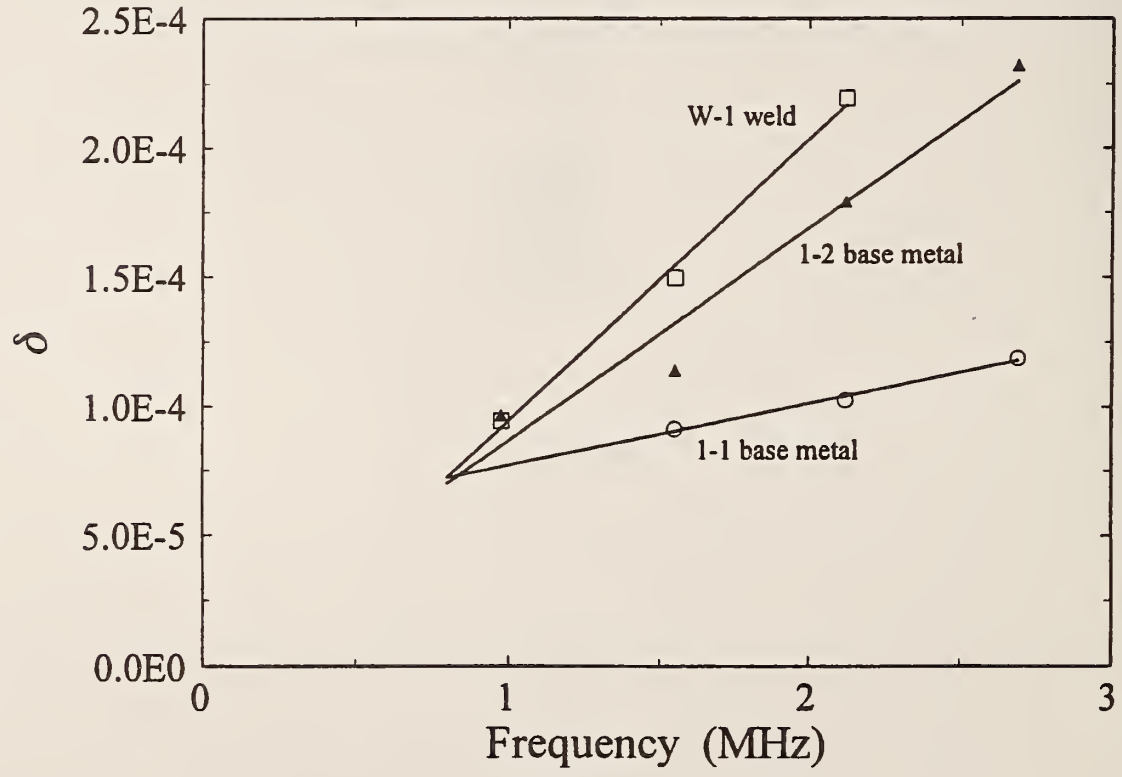

2.8.3 Equilibrium δ versus frequency of radial resonant modes in A533B specimens before deformation. 30 °C. 28 to 32 kA/m. The lines are linear regressions for each specimen.

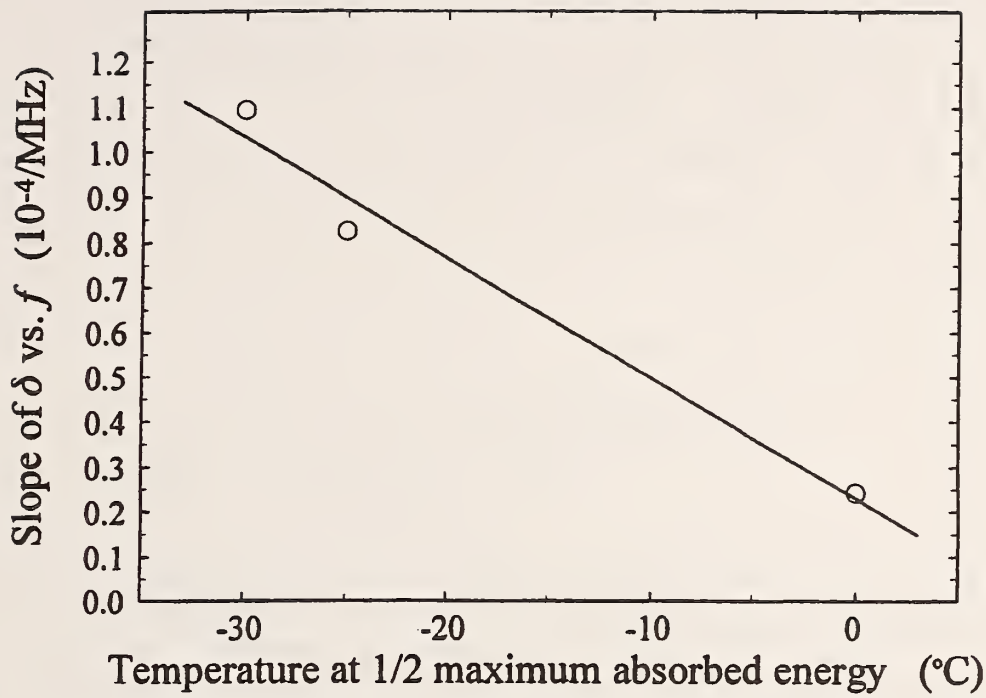

2.8.4 Slopes of the linear regressions shown in Fig. 2.8.3 versus the temperature at which the absorbed energy in the Charpy tests drops to one half that of the high-temperature plateau.

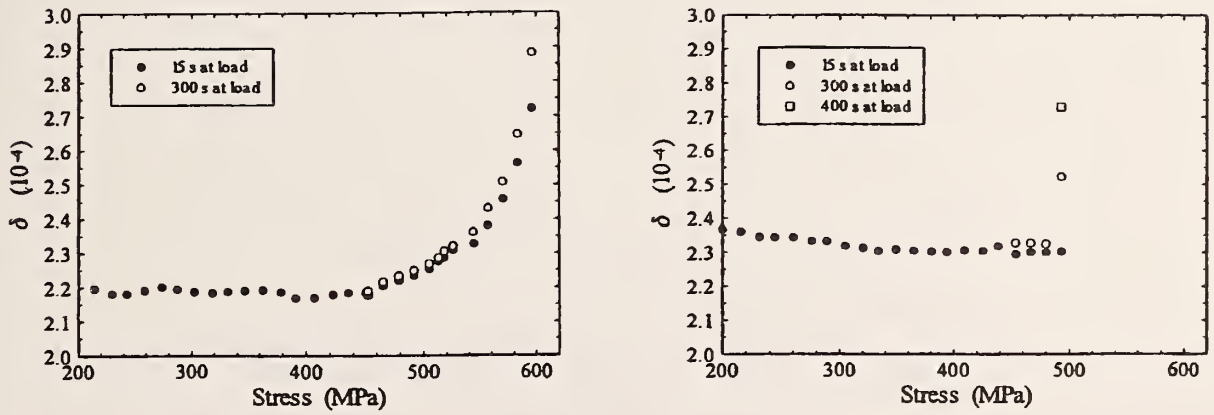

2.8.5 δ of the 0.82 MHz flexural mode of specimens C5 (a) and C7 (b) versus load during plastic deformation (33 °C, 37.8 kA/m).

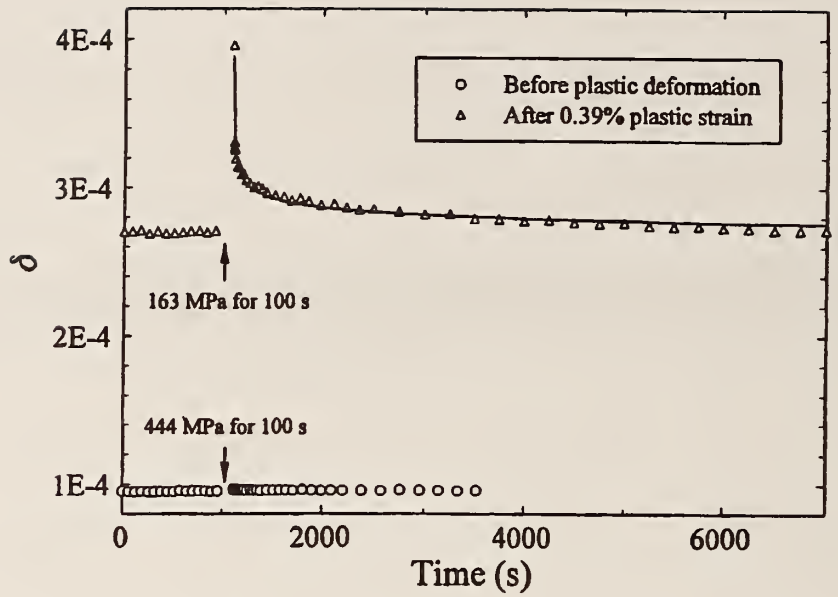

2.8.6 δ of the 1.55 MHz radial mode of specimen 1-1 (A533B) versus time before and after 0.39% plastic prestrain. The load was held at 6 MPa for 1000 s, increased to an elevated value (444 MPa before and 163 MPa after plastic deformation), held at the elevated load for 100 s, then decreased back to 6 MPa. No ultrasonic measurements were recorded while holding at the elevated loads. The solid line is a fit of the recovery data to $\delta = \delta_{eq} + [A - B\ln(1 + t/\tau)]^2$. (30 °C, 28 to 32 kA/m).

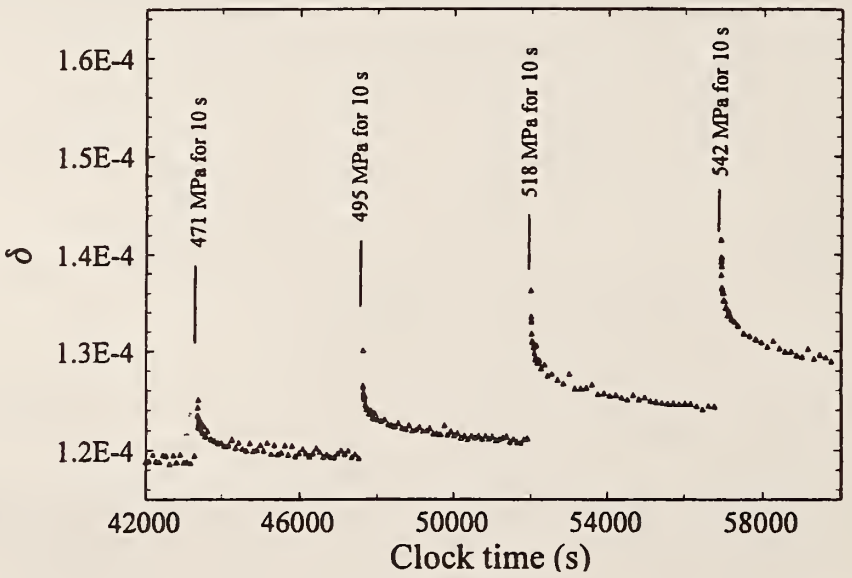

2.8.7 δ of the 1.55 MHz radial mode of specimen C5 versus time during a loading sequence. The load was held at the elevated values indicated for 10 s, and held at 6 MPa at all other times. The specimen was plastically prestrained 0.15% before the measurements were taken. No ultrasonic measurements were recorded while holding at the elevated load. (30°C, 27.2 kA/m)

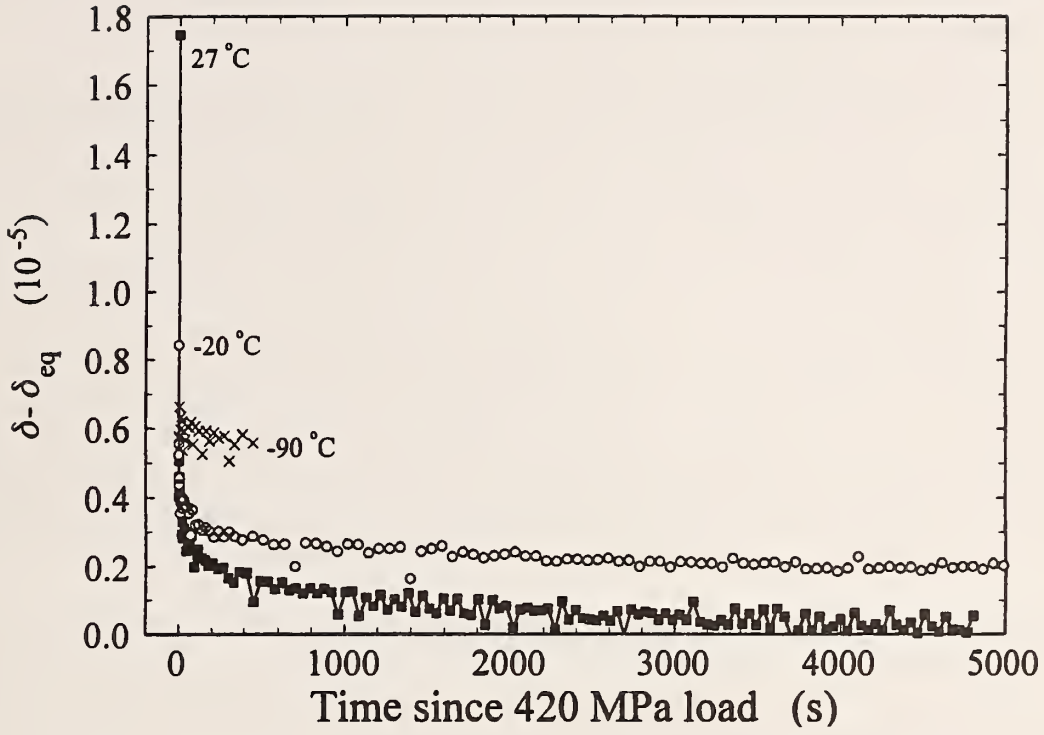

2.8.8 Recovery of δ of specimen C5 following 10 s/420 MPa loading at 27, −20, and −90 °C. The equilibrium δ_{eq} (measured before loading at each temperature) is subtracted. (2.12 MHz radial mode, 31.0 kA/m)

2.9 MEASUREMENTS UNDER CLADDING

2.9.1 Magnetic Field Penetration of SNUPPS Cladding — *G.A. Alers*

In order to measure the magnetostriction coefficient of the A533B steel under the cladding, it is necessary to subject the steel to an alternating magnetic field and an adjustable static bias field. Unfortunately, the cladding is a conductor and is slightly magnetic so it can effectively shield alternating magnetic fields. It will have no shielding effect on the static bias field except for the physical separation it will impose between the source of the bias and the A533B surface. In order to estimate the effectiveness of the cladding as a dynamic current shield and to establish quantitative design parameters for a transducer to measure the magnetostrictive characteristics of the A533B pressure vessel material under the cladding, we consider the electromagnet configuration shown in Fig. 2.9.1. A Hall probe capable of measuring dynamic magnetic fields was placed either above or below the cladding sample midway between the pole pieces of the electromagnet. It was oriented to measure the component of the field parallel to the surface of the slab. If the electromagnet is driven by an alternating current at frequency f, we can define the following measurables:

h(f) = the dynamic magnetic field under the cladding
T = the thickness of the cladding
f = the frequency of the electromagnet current and dynamic field
$h_o(f)$ = the magnitude of the field on top of the slab and
H = a static magnetic field supplied by a distant magnet (not shown) to subject the region under the slab to a bias field.

For a large spacing between the pole pieces of the electromagnet, classical electromagnetic theory would predict

$$h(f) = h_o \exp(-T/d) \qquad (1)$$

where d = the electromagnetic skin depth = $k\sqrt{(\rho/\mu f)}$. The constant k has the value 0.052 mm if the electrical resistivity ρ of the slab is measured in $\mu\Omega\cdot$cm and f in megahertz. The relative permeability of the slab is μ which may not equal 1 for the slightly magnetic stainless steel cladding.

For a first-order estimate, the Metals Handbook gives (for type 308 stainless steel) $\rho = 70$ $\mu\Omega\cdot$cm, $\mu = 1$. Equation (1) then gives

d = 1.4 mm @ f = 100 kHz
d = 4.3 mm @ f = 10 kHz
d = 14 mm @ f = 1 kHz.

or, for T = 10 mm, the dynamic field under the cladding will be attenuated to 37% of its value at the surface if the frequency is 2 kHz.

In order to get a more realistic measure of the field that will penetrate the cladding of a pressure vessel, an experimental version of Fig. 2.9.1 was set up. The electromagnet had a laminated core and was driven by a power amplifier capable of delivering up to 14A (rms) at any frequency from 0 to 50 kHz into a properly matched load. A commercial Hall probe was mounted in a wooden base so that it would measure the tangential component of the field at a point midway between the C-shaped pole pieces. A 4 mm thick slab of the stainless steel cladding cut from a sample of the SNUPPS pressure vessel was placed between the electromagnet and the Hall probe. With this configuration, the magnetic field that penetrated the cladding could be measured directly as a function of the current supplied to the electromagnet at any desired frequency. Figure 2.9.2 shows the magnitude of the field observed under the slab at a frequency of 0.1 kHz (100 Hz) for various currents in the electromagnet. The graph also shows the field values observed for 5 mm thick slabs of other materials including air. As expected, the field is a linear function of the current in the electromagnet and become smaller for a fixed current as the conductivity of the slab increases from stainless steel to aluminum.

In order to estimate the frequency at which it will be practical to operate an alternating current electromagnet above the cladding and still have a useful amount of magnetic field penetrate to the A533B substrate, field values were measured under various metal slabs as a function of the frequency of the current in the electromagnet. Such a measurement produces the quantity h(f) in eq (1). The quantity h_o in eq (1) was measured separately with the Hall probe above the metal slab as shown in Fig. 2.9.2. For a constant current in the electromagnet, h_o was observed to increase with frequency because eddy currents induced in the slab under the pole pieces produce a field that adds to the tangential field midway between the electromagnet pole pieces while they subtract from the tangential field below the slab. Equation (1) predicts that a graph of $\ln(h/h_o)$ versus the square root of the frequency should be a straight line with a slope of $119\sqrt{(\mu/\rho)}$ and an intercept of zero. Such a graph is shown in Fig. 2.9.3 for measurements on 5 mm slabs of aluminum and lead as well as the 4 mm thick slab of cladding cut from the SNUPPS RPV. The values of the slopes shown on the graph are for "best fits" to the measurements. The table below compares the slopes with the predictions of eq (1) using values of the resistivity of aluminum, lead, and type 308 stainless steel taken from handbooks.

Since the calculated and measured slopes are in reasonable agreement, eq (1) can be used to estimate the attenuation of the magnetic field to be expected as a function of frequency for cladding materials of various thicknesses. In particular, the solid line in Fig. 2.9.3 describes the attenuation for a realistic thickness of cladding of 8 mm. Based on this solid line, we estimate that 8 mm of cladding would attenuate the magnetic field to 37% (1/e) of its value at the surface if the operating frequency were 4 kHz or to 20% of the surface value if the frequency were 10 kHz.

Table 2.9.1 Comparison of measurements with the predictions of Eqn (1)

Material	Thickness (mm)	Slope (Fig. 2.9.3)	Calculated Slope	Resistivity (μΩ·cm)	Permeability (Relative)
Aluminum	5	−65	−59	2.8	1
Lead	5	−23	−21	20	1
Cladding	4	− 8	− 9	70	1

For a cladding thickness of 8 mm and accepting a factor-of-10 attenuation in the dynamic field by the cladding, Fig. 2.9.3 indicates that an acoustic wave at a frequency of 10 kHz could be excited by magnetostrictive coupling in the A533B alloy under the cladding from an AC electromagnet mounted on the cladding. The acoustic wave would be a shear wave with a propagation velocity of 3 mm/μs so its wavelength at 10 kHz would be 300 mm. This is approximately twice the thickness of the pressure vessel wall so establishing a standing wave resonance in the thickness dimension would be quite possible. A measurement of the amplitude of this resonant vibration at a fixed current in the electromagnet as a function of a biasing field would constitute a measurement of the magnetostrictive efficiency as a function of magnetic bias which is the information needed to obtain the parameters $|\lambda|$ at high H_0 and H_0 @ max $|\lambda|$ required for predicting the strength properties of interest (see Figs. 2.7.5 and 2.7.6).

2.9.2 Static Magnetic Properties (B-H Looper) — *F.R. Fickett*

The electromagnet and Hall probe configuration shown in Fig. 2.9.1 could be used with a direct current in the electromagnet to deliver a static magnetic field to the A533B steel under the cladding. Its magnitude and distribution could be calculated by finite element techniques if sufficient information about the geometry and the cladding properties were available. Such a calculation would use measurements of the magnetic field under the pole pieces and in the space between the pole pieces at the air-to-cladding interface to deduce a hysteresis curve for the A533B steel. In order to determine if such measurements would be possible on an actual pressure vessel, the Hall probe and electromagnet shown in Fig. 2.9.1 were placed on the clad surface of a 1 m square section of the Shoreham RPV and the fields around the electromagnet were measured as a function of the current in the electromagnet. The results showed that a measurable hysteresis from the A533B base metal could be detected through the cladding. Thus, it is possible to measure the coersive field Hc of the A533B steel under the cladding although the accuracy obtainable could not be judged.

2.9.3 Nonlinear Ultrasonic Experiments for Measuring RPV Wall Properties — *D. Hurley*

Nonlinear ultrasonic experiments indicate that the third-order elastic constants of steels with copper-rich precipitates are sensitive to microstructural changes that occur during hardening. One measure of the third-order elastic properties is the nonlinear ultrasonic parameter β. In the laboratory experiments described in Sect. 2.5, β correlated with hardness in a series of steel samples. Due to geometrical considerations, it may be more practical to measure the third-order properties in the reactor itself by a means other than β. One possibility is to perform ultrasonic mixing experiments such as described below. Preliminary estimates indicate that this approach may be feasible using ultrasonic waves in the 5 to10 MHz range. However, further calculations and additional laboratory experiments are necessary.

Figure 2.9.4 depicts the basic concept of a mixing experiment. Two transversely polarized ultrasonic waves at frequencies f_1 and f_2 are generated at different positions on the clad inner surface of the reactor. The waves penetrate the stainless steel layer (refraction has been ignored for simplicity), reflect off the reactor outer wall, and propagate back towards the reactor inner surface. The two waves will intersect inside the reactor steel at a position which depends on the incident angles and transducer separation. At the intersection, a longitudinal wave of frequency $f_1 + f_2$ will be generated by the same nonlinearities of the interatomic forces that give rise to the coefficient β. The longitudinal wave thus generated propagates at an angle determined by the sum of the transverse wavevectors. As shown in the figure, the transverse-wave transducers are arranged so that the longitudinal wave propagates back to the reactor's inner surface where it could be detected by a third transducer.

The amplitude of the generated longitudinal wave depends on the third-order elastic properties of the intersection volume. However, the amplitude also depends on other experimental parameters, such as the transducer dimensions, the angle between beams, the incident wave amplitude and frequency, and the second-order elastic constants. Therefore, thought must be given to an experimental approach which will isolate the effect of the third-order elastic properties from other effects. For instance, the behavior of amplitude as a function of incident angle or frequency may provide useful information. By varying the distance between the two generating transducers, the properties as a function of depth can be investigated. The use of mixing techniques (as opposed to harmonic generation) ensures that the detected signals are due solely to the third-order properties of the interaction volume and are not related to experimental artifacts.

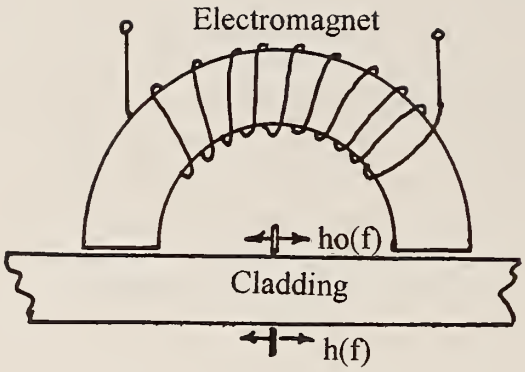

Fig. 2.9.1 Schematic diagram of an electromagnet designed to apply an alternating magnetic field to the cladding on the inner surface of a reactor pressure vessel. The field h(f) penetrates the cladding and is applied to the pressure vessel itself.

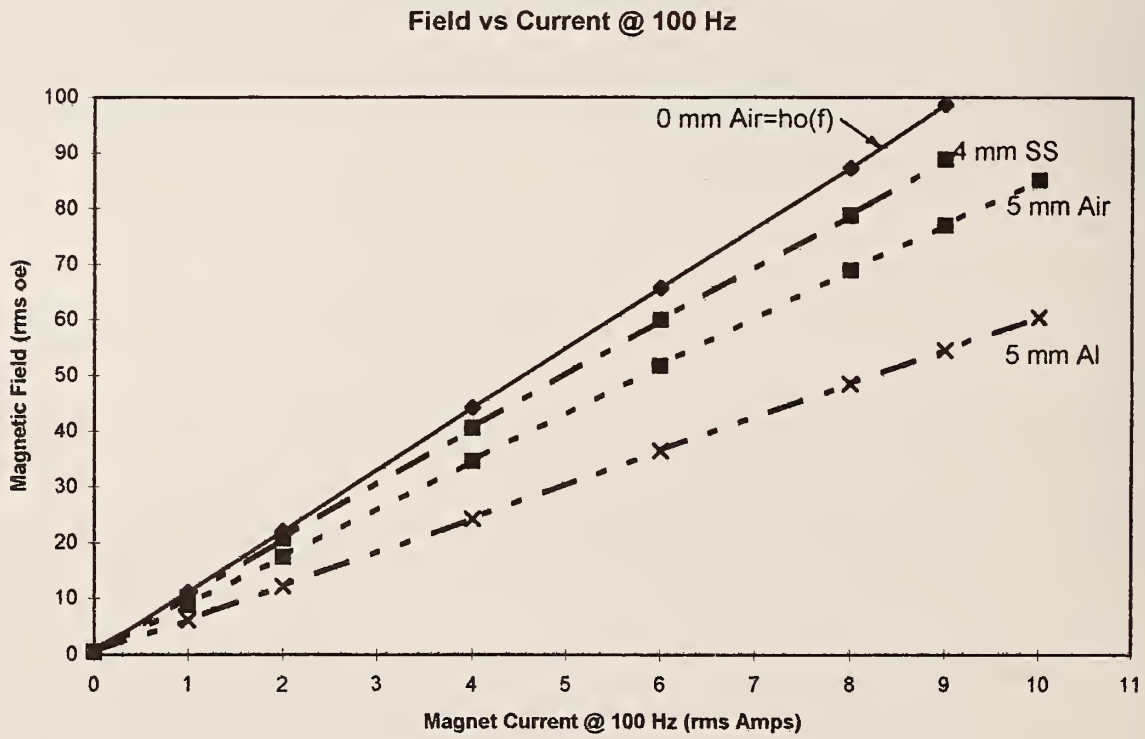

Fig. 2.9.2 Magnetic field that penetrates slabs of different materials as a function of the current in the electromagnet shown in Fig. 2.9.1.

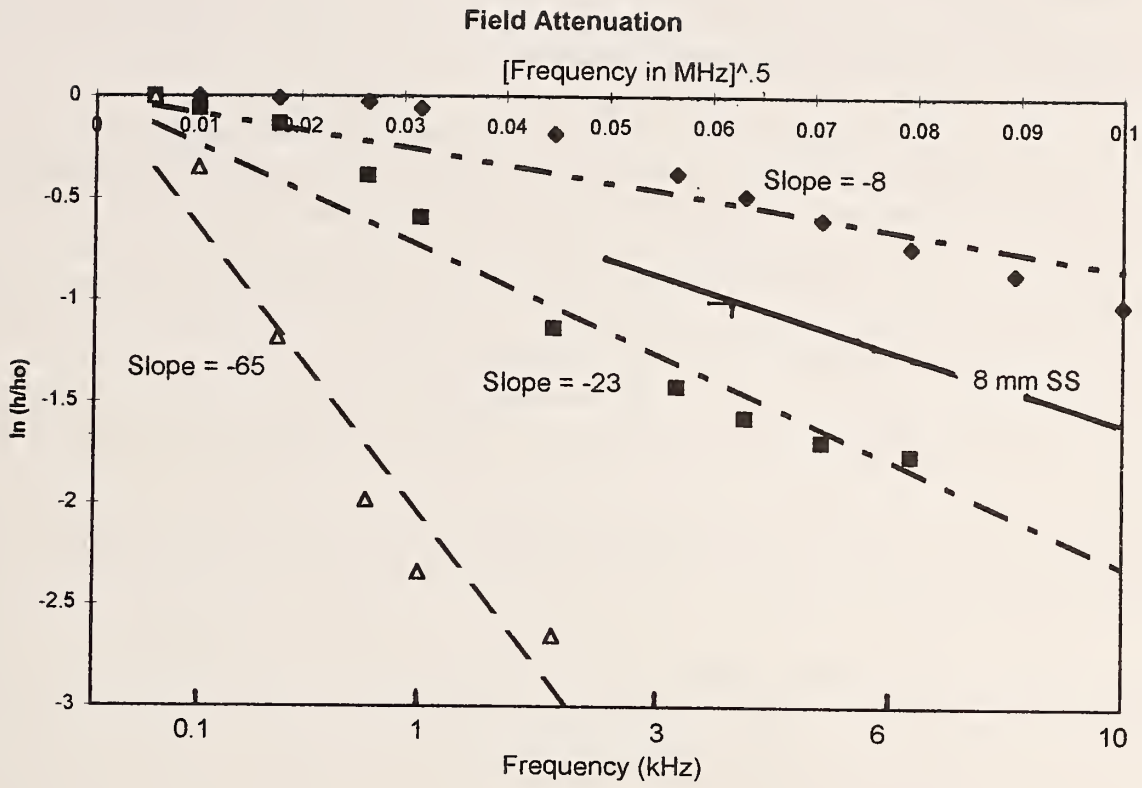

Fig. 2.9.3 Magnetic field penetrating slabs of different materials as a function of the frequency of the 1 A (rms) current in the electromagnet. The solid line depicts the field expected for a cladding thickness of 8 mm. (▵ Aluminum, ■ Lead, ♦ Stainless Steel)

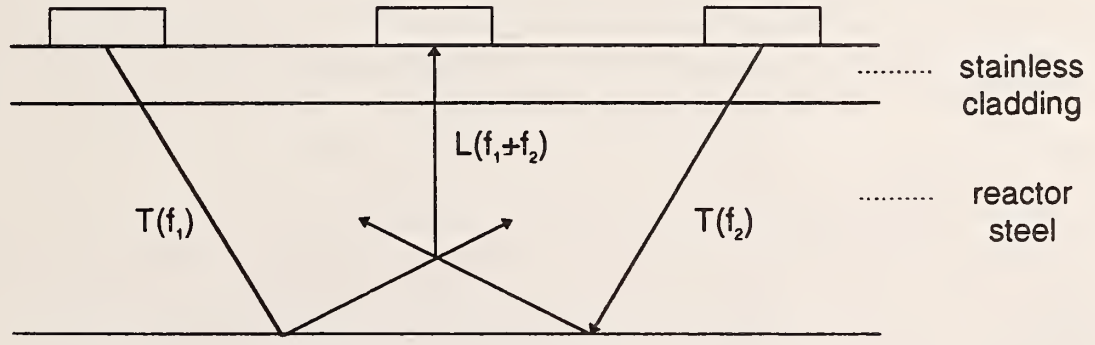

Fig. 2.9.4 Schematic diagram of a proposed configuration of ultrasonic transducers that could measure the nonlinear acoustic response of RPV material under the cladding by measuring the efficiency of mixing of two input waves to produce a third wave.

3. DISCUSSION

3.1 Physical Property-Strength Correlations

A major subtask of the research presented here was to produce a collection of physical property measurements on a material of controlled microstructure for which the relationship between microstructure and mechanical strength was known. The A710 (Fe-1.13 mass % Cu alloy) provided a steel whose strength properties could be varied over an extensive range by heat treatments and whose changes in microstructure were similar to those thought to be the cause of radiation induced embrittlement of A533B steels. Therefore, the A710 steel was used here as a surrogate of A533B on which to establish relationships between destructively measured strength properties and nondestructively measured physical properties. Tables 3.1.2, 3.1.3 and 3.1.4 at the end of this section compile the results of all of the mechanical strength measurements and the physical property measurements described in the preceding sections of this report. Examination of all the data shows that there were 6 strength-related properties and 10 physical properties available for establishing interrelationships. These are listed in Table 3.1.1 along with the symbols used to describe them in the text.

In performing the mechanical strength tests on the A710 surrogate alloy as well as on the A533B RPV material, we observed a major difference in deformation mode and its influence on the development of relationships between physical properties and strength must be kept in mind. Specifically, the solution treated and peak-aged samples of the A710 alloy showed a smooth transition from elastic to plastic strain as the stress was increased. On the other hand, the over-aged A710 steel and the A533B samples showed discontinuous yielding with little or no

Table 3.1.1 List of mechanical strength properties and physical properties measured in this program.

Strength property	Symbol	Physical property	Symbol
Proportional limit	PL	Elastic modulus	E, G, or B
0.2% yield strength	0.2%YS	Density	ρ
Ultimate Tensile Strength	UTS	Internal friction	Q^{-1} or δ
Ductile-to-brittle		Nonlinear ultrasonic parameter	β
transition temperature	DBTT	Internal strain	ϵ
Hardness	HRA	High field average magnetostriction	$\lambda\infty$
Elongation	% Elong.	Field at maximum magnetostriction	H_{max}
		Max. transverse incremental permeability	μ_t (max)
		Magnetic coercive force	Hc
		Saturation magnetization	$\mu_0 M_s$

plastic flow preceding the load drop when loaded at a constant strain rate. All the materials showed similar ultimate tensile strengths and large elongations so they all had comparable ductilities. Thus, a difference in correlations with physical properties can be expected for strength parameters that reflect yielding phenomena at low plastic strains, and ductile and work-hardening parameters that describe deformation at high plastic strains. Figure 3.1.1 graphs three important strength parameters plotted against hardness for the A710 steel. It shows a good linear correlation or proportionality between the hardness and the UTS but a nonlinear relationship with the proportional limit and the 0.2%YS. Plotting the DBTT versus hardness for the A710 alloy series shows a linear correlation similar to that observed for the UTS in Fig. 3.1.1. Thus, if a nondestructive measurement of the DBTT is desired, then those physical properties that show a strong correlation with hardness or UTS can be considered good candidates. If a physical property does not correlate well with hardness, it may be useful as a predictor of the proportional limit or the 0.2% YS and reflect the early stages of plastic flow when dislocations are just beginning to be mobile.

To test for strong correlations between physical properties and the strengthening effect of the copper rich precipitates (CRPs), each physical property was plotted against the hardness and against the proportional limit for the A710 alloy in its three conditions of tempering. Since the physical properties have a wide range of numerical values, these plots are best presented to the reader in a normalized format in which the values are divided by the value for the solution treated, initial condition of the alloy. This form of presentation allows the percentage change in property value to be read from the ordinate as the hardness or the proportional limit (the abscissa) extends from its minimum to its maximum value. Figure 3.1.2 shows the case of plotting against the hardness and Fig. 3.1.3, the case for plotting against the proportional limit. The choice of which property was plotted against which strength parameter was motivated by the requirement that the resulting curve need not be linear but should be monotonically increasing or decreasing in order to avoid double valued relationships. The fact that the correlations with hardness shown in Fig. 3.1.2 are all increasing while all those correlated with the proportional limit (Fig. 3.1.3) are decreasing is coincidental. Examination of these graphs shows that 8 of the 10 properties measured and listed in Table 3.1.1 showed a monotonic correlation with either the hardness or the proportional limit. The two properties not graphed, the density and the saturation magnetization, showed very small changes during the heat treatment and would be difficult to measure in a nondestructive test.

Figures 3.1.1 and 3.1.2 show hardness as the abscissa. Because it is equivalent to the ductile-to-brittle transition temperature, the figures demonstrate that there are four physical properties that could be candidates for a nondestructive predictor of the DBTT. These are the internal strain ϵ, the high field average magnetostriction λ_{∞}, the maximum transverse magnetic permeability μ_t (max) , and the nonlinearity parameter β. All of these, with the exception of ϵ and μ_t, can be measured by ultrasonic techniques. As discussed in Sect. 2.9, it is also possible to make these measurements through the stainless steel cladding so they could, in principle, be performed on the inner surface of a pressure vessel. To emphasize this encouraging result, Fig. 3.1.4 graphs these three parameters against the DBTT. Here the normalization factor used is the value of the

property for the alloy in the overaged condition (C7). These results describe only three heat treatment conditions of a steel containing 1.13 mass percent Cu in which the responses to the Charpy test were dramatically different (see Fig. 2.2.3). In RPV steels, the copper concentrations are much smaller and the shelf energies and transition temperatures are much closer together. However, the properties measured appear sensitive to the strength parameter in that they change by more than 10% over the range of hardness and DBTT investigated.

The graph of properties against the proportional limit (Fig. 3.1.3) show that the shear modulus and the coercive force, H_c, are insensitive to the heat treatment that forms the CRPs and maximizes the hardness. Most of the change in these properties occurs when the copper forms ϵ phase precipitates. The internal friction δ and the field at which the magnetostriction is maximum (H_{max}) show a good correlation with the proportional limit and sensitively indicate the change in this strength parameter during the formation of the CRPs.

3.2 Dislocation Mechanisms

Concerning the dislocation mechanisms that may underlie these correlations, the mechanical properties involving large deformations (hardness, UTS, and DBTT) are correlated with physical properties (ϵ, β, μ_t, and $\lambda\infty$) that reflect changes in microstructure on a nearly atomic scale. The internal strain, ϵ, is deduced from x-ray diffraction line broadening and is interpreted as reflecting the strain around the CRP clusters as they retain coherency with the lattice. This internal strain field obviously interacts with the dislocations to impair their motion over long distances as measured by the UTS. The acoustic nonlinearity parameter β measures the changes in the interatomic forces produced by strain. Hence, it is not surprising that it, too, is sensitive to internal strain fields and, thus, can be used as a nondestructive measure of internal strains. The two magnetic parameters, μ_t and $\lambda\infty$, measure the mobility of domain walls and the freedom of atomic spins to rotate relative to the direction of the applied field, respectively. They, too, are known to be sensitive to applied strains and, therefore, their measurement can be used to measure internal strains. The fact that all four properties are related to the dislocation motion at the ultimate tensile stress indicates that internal strains control the motion of dislocations at high levels of deformation.

For the low strain mechanical properties (proportional limit and upper yield stress), the dominant mechanism of dislocation motion is the release of dislocations from pinning points or impurity atmospheres by an applied stress. Since H_{max} and δ change with the proportional limit during the formation of CRPs as shown in Fig. 3.1.3, these two measurable parameters must be sensitive to the depinning of dislocations and the initiation of plastic flow at small strain levels. The sensitivity of δ to the release of dislocations was measured directly in our measurements of the effect of a static stress on dislocation mobility that are described in Section 2.8 above. Unfortunately, these experiments show that a measurement of the static stress needed to increase the internal friction or to produce a small amount of plastic flow cannot be considered a nondestructive test because they leave the material changed and require application of very high stresses to activate dislocation motion. On the other hand, the time dependent recovery of δ

following microscopic plastic flow shows some promise of indicating the degree of dislocation mobility that is available at low stresses soon after removal of a high stress. The dependence of this mobility on the temperature could be an indicator of the DBTT.

3.3 Temperature Effects

Some of the physical properties investigated in this program could be measured as a function of decreasing temperature through the region of the DBTT. These were Young's modulus, its associated damping capacity Q^{-1}_E, and the magnetic parameters λ_∞ and μ_t. Graphs of these quantities as a function of temperature can be found in Section 2.3 for the elastic properties and Section 2.7 for the micromagnetic properties. The magnetic hysteresis properties, H_c and B_s were measured at both liquid nitrogen temperature and at room temperature and showed no unexpected variations. In general, all the properties varied smoothly between room temperature and -100 °C with no unusual behavior at the DBTT for the alloys involved. There was a sharp peak in the internal friction near -10 °C in the solution treated A710 steel which might be due to a dislocation relaxation phenomenon but relating it to the DBTT will require considerable additional effort. The micromagnetic parameters were measured as a function of temperature on the A533B steel samples cut from the weld and from the bulk of the SNUPPS RPV. At room temperature, the measurements could not distinguish between the sources of the material. However, at -100°C the material from the weld (Sample W1) and from the bulk (Sample 1-2) could be distinguished by their values of λ_∞ and μ_t. (See Fig. 2.7.12). Again, considerable more study is needed to determine whether these observed differences in magnetic properties can be related to the difference in DBTT for these two samples of A533B steel.

Table 3.1.2 Values for the mechanical strength parameters for the steels studied here.

Sample	Condition	Prop. Lim MPa	Upper YS MPa	0.2% YS MPa	Ultimate MPa	Elong. %	Hardness Rock. A	41J DBTT °C
A710-CA	Soln treat	173	—	415	650	28.8	55.5	-33
A710-C5	Peak aged	391	—	551	718	25.1	58.5	-10
A710-C7	Overaged	446	471	471	558	29.2	53.2	-60
1508-AA	Quenched	285	—	575	821	6.6	59	—
1508-A5	As Rec'd.	576	576	560	610	24.8	54	—
1508-A6	1 h @ 675	524	524	514	594	25.3	53	—

Table 2.1.3 Values of the mechanical strength parameters for the SNUPPS A533B.

Sample	Condition	Prop. Lim MPa	Upper YS MPa	0.2% YS MPa	Ultimate MPa	Elong. %	Hardness Rock. A	41J DBTT °C
A533B	1-1	479	491	465	610	38	55	-20
A533B	1-2	461	468	452	574	43	53	-60
A533B	2-1	476	482	475	600	40	55	-25
A533B	2-2	513	525	507	640	35	56	-20
A533B	W-1	568	589	578	672	24	57	-30

Table 3.1.4 Compilation of physical properties measured to date.

Sample	Condition	Density g/cm^3	E GPa	G GPa	B GPa	$\delta(E) \times 10^4$	$\delta(G) \times 10^4$	$\delta(B) \times 10^4$	H_c A/m	$\mu_0 M_s$ Tesla	Hill λ Arbit.	H_{max} kA/m	Max μ_t Relative	β	Strain %
A710-CA	Soln treat	7.8414	207.9	80.71	163.42	3.12	4.18	6.57	668	2.03	940	16.5	200	5.16	0.069
A710-C5	Peak aged	7.8558	208.7	81.03	163.71	2.01	2.51	1.35	642	2.07	1050	10.6	222	5.36	0.074
A710-C7	Over aged	7.8534	209.5	81.36	164.41	2.28	2.67	2.79	485	2.06	780	7.1	170	4.81	0.053
1508-AA	Quenched	7.8507	208.9	81.17	163.43	1.9	2.17	0.25	479	2.09					0.156
1508-AA2	Air Cooled	7.8472	210.2	81.73	163.72	4.46	4.81	2.36							
1508-A5	As Rec'd.	7.8488	209.9	81.59	163.5	2.08	2.07	2.04	496	2.09		4.2	224	5.66	0.093
1508-A6	1 hr @ 675	7.8492	210.4	81.85	163.26	2.4	2.23	3.33	493	2.02		4.2	224	5.42	0.091
A533B 1-2	Bulk	7.8532	211.1	82	165.13	2.23	2.1	2.95	544	2.06			170	5.3	0.073
A533B W1	Weld	7.8339	211.2	82.11	164.39	2.46	2.7	1.07	712	2.05			171	6.56	0.077
Pure Iron	0.0007wt%C	7.872	212.36	82.44	166.93	7.9	7.7	9.1							

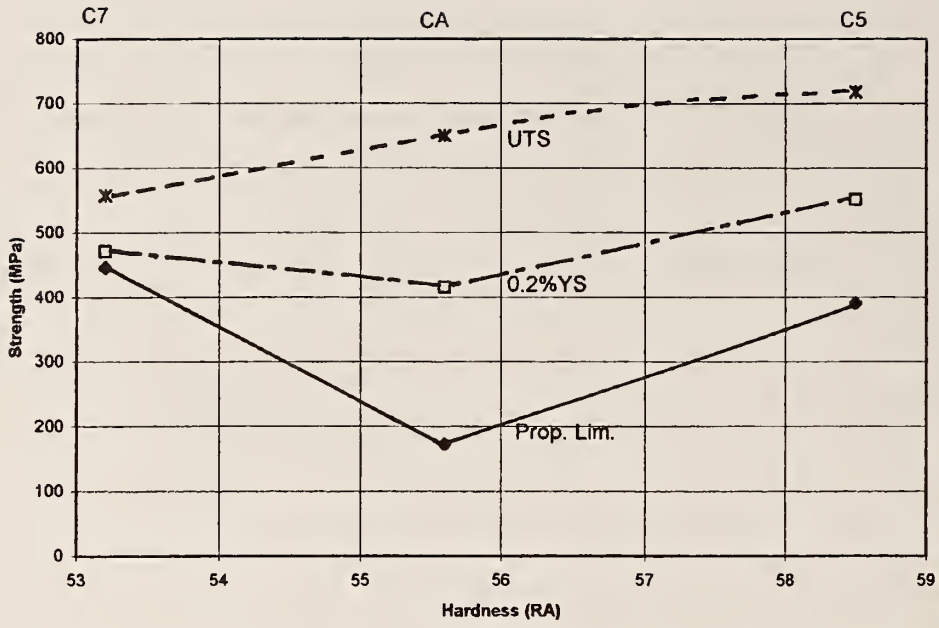

Fig. 3.1.1 Relationship between three different measures of strength (the proportional limit, the 0.2% yield strength,and the ultimate tensile strength) and the hardness as measured on the Rockwell A scale.

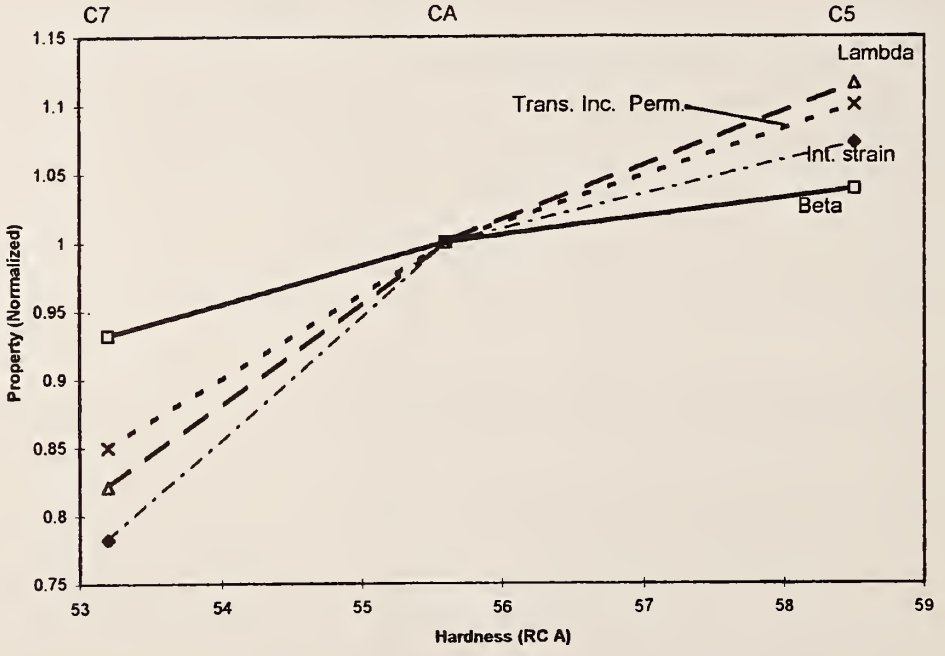

Fig. 3.1.2 Physical properties that exhibit a monotonic change with hardness in the A710 alloy series. For convenience in presentation, the properties have been normalized by their values in the solution treated state (CA).

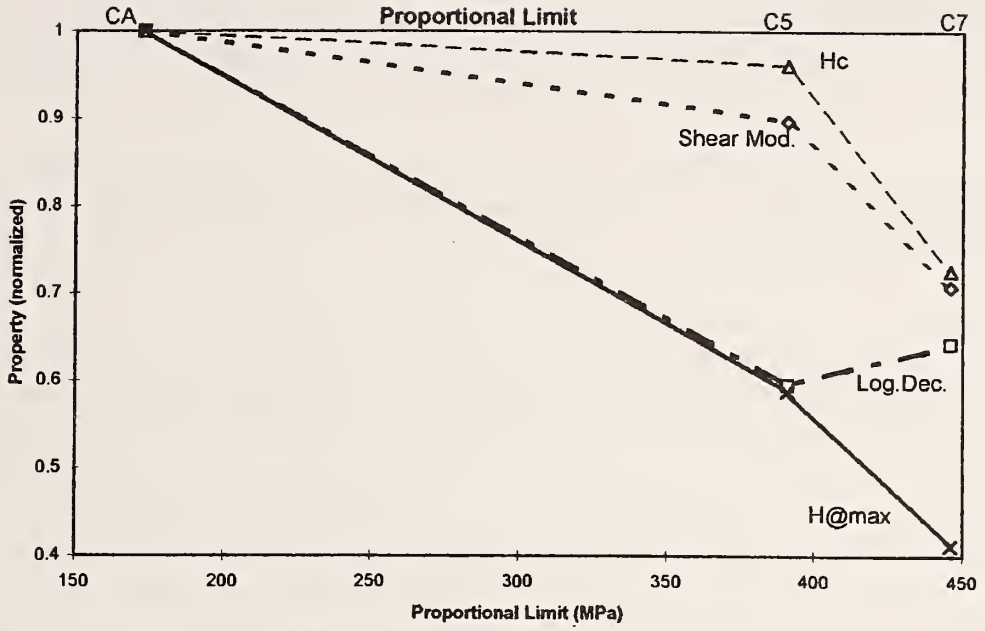

Fig. 3.1.3 Physical properties that exhibit a monotonic change with the proportional limit for the A710 series. For convenience of plotting, the properties have been normalized by their values in the solution treated state (CA).

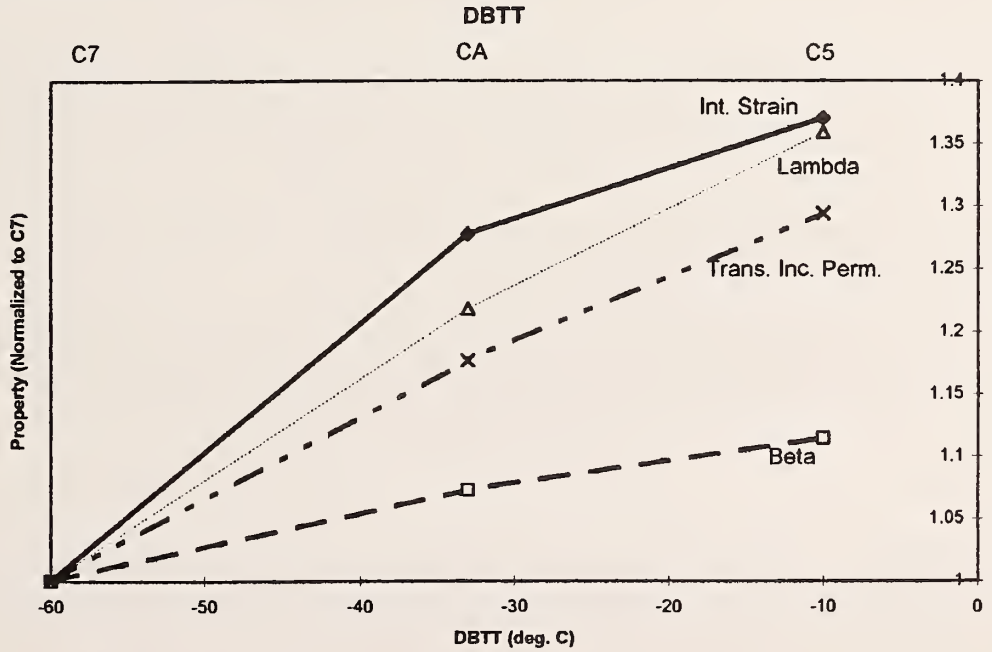

Fig. 3.1.4 Relationship between four of the physical properties and the ductile-to-brittle transition temperature (DBTT) for the three heat treatments of the Fe-1.13% Cu alloy. The properties have been normalized by their values in the overaged condition (C7).

4. CONCLUSIONS

4.1 Task I

Task I was to define and investigate nondestructive physical property measurements that could be promising candidates for predicting the DBTT in radiation embrittled A533B steel. The most significant findings were:

1. Based on the measurements carried out in Task II, several physical properties appear capable of predicting the ultimate tensile strength, the hardness, and the DBTT of a steel in which the embrittlement mechanism is similar to that responsible for embrittlement of RPVs. These properties are the nonlinear ultrasonic parameter β, the mximum transverse incremental permeability μ_t, and the high field average magnetostriction $\lambda\infty$. All three properties can be deduced from ultrasonic measurements that can be performed nondestructively. Two other properties, the internal friction Q^{-1} and the field at which the magnetostriction is a maximum H_{max} appear to be related more closely to the proportional limit than to the hardness or the DBTT.

2. Measurement of several physical properties including Young's modulus, the internal friction parameter Q^{-1}, μ_t and $\lambda\infty$ were made as a function of temperature over a range that included the DBTT in both the A710 and A533B alloys. All the properties measured under these conditions showed a nearly linear temperature dependence with no special variations in the vicinity of the DBTT.

3. The static stress needed to initiate plastic flow (that is, to produce dislocation breakaway and motion) was near the proportional limit observed in conventional constant strain rate tensile tests. Once deformed, however, the static stress needed to cause a release of dislocations and an increase in internal friction was much lower than the proportional limit. Time–dependent recovery of this internal friction at a low load was similar to that observed during recovery of cold–worked material at elevated temperature.

4. The magnitude of the internal friction was so small (even after small amounts of plastic deformation) that it would be difficult to measure by conventional ultrasonic pulse-echo techniques.

4.2 Task II

Task II was to accurately measure physical properties on an A710 steel (Fe-1.13%Cu) surrogate for the RPV steel in which tempering could be used to produce samples strengthened to different levels by the formation of copper rich precipitates (CRPs) similar to those suspected of causing radiation induced embrittlement in A533B alloys. Three sets of samples were produced in the solution treated, peak aged and overaged conditions. Tensile tests of constant strain rate and Charpy V-notch tests were used to determine five measures of mechanical strength. Ultrasonic, magnetic, and x-ray techniques accurately measured 10 physical properties. Correlations between

mechanical and physical properties fell into two classes: those that were related to large deformation mechanical properties such as the ultimate tensile strength, and those that related to the initiation of plastic flow such as the proportional limit. The results can be summarized as follows:

1. Three properties that exhibit a monotonically increasing correlation with the UTS, the hardness and the DBTT are the high field average magnetostriction $\lambda\infty$, the maximum in the transverse incremental permeability, μ_t, and the nonlinear ultrasonic coefficient β that quantifies harmonic generation. All three can be deduced from nondestructive ultrasonic measurements.

2. These three physical properties were found to be proportional to internal strains measured by the broadening of x-ray diffraction peaks and presumed to arise from coherency strains surrounding the CRPs.

3. Four other properties exhibit monotonically decreasing correlations with the proportional limit and the 0.2% yield stress. These were the internal friction Q^{-1}, the field H_{max}, at which the magnetostriction is a maximum, the elastic moduli, and the coercive field, H_c. The latter two are much less sensitive to the proportional limit and 0.2% yield strength than are the former two.

4. Because the internal friction depends on irreversible depinning and motion of dislocations after the proportional limit has been exceeded, this physical property may be unsuitable as a nondestructive test. However, the temperature dependence of the internal friction and its response to incremental changes in stress may be good indicators of the mechanical properties of the material. Unfortunately, the magnitude of the internal friction for the A710 and A533B steels was so small that it will be difficult to measure with conventional pulse echo techniques.

4.3 Task III

Tasks I and II produced a list of ultrasonic and magnetic properties that were sensitive to the microstructural features that control the mechanical strength of an A710 steel and an the A533B steel. Task III was to discuss the possible ways in which these properties could be measured through the stainless steel cladding that covers the inner surface of an actual pressure vessel. Of the 10 measurables investigated, 3 appear able to meet the requirements of being nondestructive, having good sensitivity to the desired mechanical property and being able to operate through the cladding. These are:

1. Deducing quantities related to H_{max} and $\lambda\infty$ from measurements of the amplitude of a low frequency shear wave generated by magnetostrictive coupling at the cladding-to-A533B steel interface.

2. Deducing a quantity related to β from measurements of the amplitude of a longitudinal wave produced by mixing two shear waves.

3. The magnetic coercive force H_c of the A533B material under the cladding could be deduced from measurements of the static magnetic field distribution around an electromagnet placed on the cladding but this particular physical property (like the elastic moduli) does not appear to be particularly sensitive to the CRPs responsible for embrittlement.

A more detailed discussion of making measurements through the cladding can be found in Section 2.9 above.

5. RECOMMENDATIONS

1. Perform the physical property measurements that are related to the ductile-to-brittle transition temperature of the A710 alloy surrogate or a second surrogate material whose mechanical properties more nearly match the response of the A533B alloy to radiation damage.

2. Develop procedures for measuring those physical properties that are sensitive to the DBTT on half compact tension specimens in a hot cell. Perform these measurements on surveillance specimens that have been subjected to different neutron fluences in a reactor. Determine the quality of correlations between the measured physical properties and the DBTT and the fracture toughness of the surveillance specimens.

3. Determine the accuracy and the reliability for measuring magnetostriction and nonlinear acoustic parameters of the A533B alloy under the cladding.

*U.S. GOVERNMENT PRINTING OFFICE 1998-0-673-018/40104

NIST Technical Publications

Periodical

Journal of Research of the National Institute of Standards and Technology—Reports NIST research and development in those disciplines of the physical and engineering sciences in which the Institute is active. These include physics, chemistry, engineering, mathematics, and computer sciences. Papers cover a broad range of subjects, with major emphasis on measurement methodology and the basic technology underlying standardization. Also included from time to time are survey articles on topics closely related to the Institute's technical and scientific programs. Issued six times a year.

Nonperiodicals

Monographs—Major contributions to the technical literature on various subjects related to the Institute's scientific and technical activities.

Handbooks—Recommended codes of engineering and industrial practice (including safety codes) developed in cooperation with interested industries, professional organizations, and regulatory bodies.

Special Publications—Include proceedings of conferences sponsored by NIST, NIST annual reports, and other special publications appropriate to this grouping such as wall charts, pocket cards, and bibliographies.

Applied Mathematics Series—Mathematical tables, manuals, and studies of special interest to physicists, engineers, chemists, biologists, mathematicians, computer programmers, and others engaged in scientific and technical work.

National Standard Reference Data Series—Provides quantitative data on the physical and chemical properties of materials, compiled from the world's literature and critically evaluated. Developed under a worldwide program coordinated by NIST under the authority of the National Standard Data Act (Public Law 90-396). NOTE: The Journal of Physical and Chemical Reference Data (JPCRD) is published bimonthly for NIST by the American Chemical Society (ACS) and the American Institute of Physics (AIP). Subscriptions, reprints, and supplements are available from ACS, 1155 Sixteenth St., NW, Washington, DC 20056.

Building Science Series—Disseminates technical information developed at the Institute on building materials, components, systems, and whole structures. The series presents research results, test methods, and performance criteria related to the structural and environmental functions and the durability and safety characteristics of building elements and systems.

Technical Notes—Studies or reports which are complete in themselves but restrictive in their treatment of a subject. Analogous to monographs but not so comprehensive in scope or definitive in treatment of the subject area. Often serve as a vehicle for final reports of work performed at NIST under the sponsorship of other government agencies.

Voluntary Product Standards—Developed under procedures published by the Department of Commerce in Part 10, Title 15, of the Code of Federal Regulations. The standards establish nationally recognized requirements for products, and provide all concerned interests with a basis for common understanding of the characteristics of the products. NIST administers this program in support of the efforts of private-sector standardizing organizations.

Consumer Information Series—Practical information, based on NIST research and experience, covering areas of interest to the consumer. Easily understandable language and illustrations provide useful background knowledge for shopping in today's technological marketplace.

Order the **above** *NIST publications from: Superintendent of Documents, Government Printing Office, Washington, DC 20402.*

Order the **following** *NIST publications—FIPS and NISTIRs—from the National Technical Information Service, Springfield, VA 22161.*

Federal Information Processing Standards Publications (FIPS PUB)—Publications in this series collectively constitute the Federal Information Processing Standards Register. The Register serves as the official source of information in the Federal Government regarding standards issued by NIST pursuant to the Federal Property and Administrative Services Act of 1949 as amended, Public Law 89-306 (79 Stat. 1127), and as implemented by Executive Order 11717 (38 FR 12315, dated May 11, 1973) and Part 6 of Title 15 CFR (Code of Federal Regulations).

NIST Interagency Reports (NISTIR)—A special series of interim or final reports on work performed by NIST for outside sponsors (both government and non-government). In general, initial distribution is handled by the sponsor; public distribution is by the National Technical Information Service, Springfield, VA 22161, in paper copy or microfiche form.

U.S. Department of Commerce
National Institute of Standards and Technology
325 Broadway
Boulder, Colorado 80303-3328